ABSTRACT

INVESTIGATIONS AND APPLICATIONS OF FIELD- AND PHOTO-EMITTED ELECTRON BEAMS FROM A RADIO FREQUENCY GUN

SriHarsha Panuganti, Ph.D.
Department of Physics
Northern Illinois University, 2015
Philippe Piot, Director

Production of quality electron bunches using efficient ways of generation is a crucial aspect of accelerator technology. Radio frequency electron guns are widely used to generate and rapidly accelerate electron beams to relativistic energies. In the current work, we primarily study the charge generation processes of photoemission and field emission inside an RF gun installed at Fermilab's High Brightness Electron Source Laboratory (HBESL). Specifically, we study and characterize second-order nonlinear photoemission from a Cesium Telluride (Cs_2Te) semiconductor photocathode, and field emission from carbon based cathodes including diamond field emission array (DFEA) and carbon nanotube (CNT) cathodes located in the RF gun's cavity. Finally, we discuss the application experiments conducted at the facility to produce soft x-rays via inverse Compton scattering (ICS), and to generate uniformly filled ellipsoidal bunches and temporally shaped electron beams from the Cs_2Te photocathode.

NORTHERN ILLINOIS UNIVERSITY
DE KALB, ILLINOIS

AUGUST 2015

INVESTIGATIONS AND APPLICATIONS OF FIELD- AND PHOTO-EMITTED ELECTRON BEAMS FROM A RADIO FREQUENCY GUN

BY

SRIHARSHA PANUGANTI
© 2015 SriHarsha Panuganti

A DISSERTATION SUBMITTED TO THE GRADUATE SCHOOL

IN PARTIAL FULFILLMENT OF THE REQUIREMENTS

FOR THE DEGREE

DOCTOR OF PHILOSOPHY

DEPARTMENT OF PHYSICS

Dissertation Director:
Philippe Piot

ACKNOWLEDGEMENTS

It has been mostly a fun (but a bit bumpy) ride during the course of this dissertation work. At the end of the day, I would not wish I had better opportunities. There have been many individuals at NIU and at Fermilab who played their roles in making the current work possible. Firstly I would like to acknowledge the efforts put by my esteemed team Philippe Piot, Daniel Mihalcea (NIU) and Charles Thangaraj (FNAL). Philippe's extraordinary effort was necessary for the conception, construction and operation of the HBESL facility; he had been at the center of this research all along. The numerous discussions I had with Charles and especially with Daniel, were significant in my learning process, besides our discussions on world politics and history. I would like to thank my fellow graduate students Ben Blomberg, Francois Lemery and former graduate student Tim Maxwell for their help. Jinhao Ruan, Jamie Santucci, Yin-E Sun and Elias Lopez had lend their hands whenever we needed them. I'm grateful to all the folks who were responsible for building and supporting the A0 photoinjector whose infrastructure we utilized extensively. I would like to thank our collaborators from RadiaBeam Technologies, MIT and Vanderbilt University for their participation. I'm thankful to Zhili Xiao and the late Clyde Kimball for their brief financial support during my second semester in the Physics program. I want to thank Bela Erdelyi and Yasuo Ito for serving on my dissertation committee.

The city of DeKalb has treated me well during my stay so far, it's been fun. I will cherish NIU's beautiful campus and my graduate study in the Dept. of Mechanical Engineering; if it were not for my former advisor Federico Sciammarella's (random)

idea, I would not have pursued my Ph.D. studies in Physics. There are many friends who kept good company during my course of study and made my life not boring. Finally, my family has been very encouraging and supportive during my twelve years in college, especially my latest six years in the Ph.D. program.

This work was supported by the United States Department of Energy under contract DE-FG02-08ER41532 with Northern Illinois University and DE-SC0004459 with Radiabeam Technologies, LLC. The work was also performed at Fermi National Accelerator Laboratory which is operated by the Fermi Research Alliance, LLC under Contract No. DE-AC02-07CH11359 with the United States Department of Energy.

DEDICATION

To all the animal rights advocates and activists across the globe who strive for the truly voiceless and defenseless, animals. Compassion transcends love, faith and belief.

TABLE OF CONTENTS

Page

LIST OF TABLES ix

LIST OF FIGURES. x

Chapter

1 INTRODUCTION 1

2 HBESL PHOTOINJECTOR AND RELATED ACCELERATOR PHYSICS 4

2.1 Pertinent Beam Dynamics Concepts 4

2.2 Overview of HBESL Photoinjector 6

2.2.1 Introduction and General Layout 6

2.2.2 Radio Frequency Components 7

2.2.2.1 RF Gun 7

2.2.2.2 Transverse Deflecting Cavity 9

2.2.2.3 RF System 11

2.2.3 Magnets. 13

2.2.3.1 Solenoids 13

2.2.3.2 Dipole and Quadrupole Magnets. 14

2.2.4 Beam Diagnostics 15

2.2.4.1 Transverse Beam Diagnostics 15

2.2.4.2 Charge Measurement 17

2.2.4.3 Energy Measurement 18

Chapter Page

3 PULSED LASER GENERATION FOR PHOTOINJECTION 20

3.1 Mathematical Representation of a Light Pulse 20

3.2 Time–Bandwidth Product of a Light Pulse 23

3.2.1 Transform-limited Pulse 25

3.3 Overview of HBESL's Laser System 26

3.4 The Octavius-85M Oscillator Laser 27

3.4.1 Self-phase Modulation (SPM) 30

3.4.2 Kerr Lens Mode Locking 32

3.4.3 Operation of the Octavius-85M 34

3.5 Regenerative Amplification 36

3.6 Laser Pulse Shaping 41

3.7 Frequency Upconversion 45

3.8 Temporal Laser Diagnostics 50

4 LASER SYNCHRONIZATION WITH THE RF GUN 53

4.1 81.25-MHz Phase Locking 55

4.2 1.3-GHz Phase Locking 59

5 LINEAR AND MULTIPHOTON PHOTOMISSION FROM CESIUM TELLURIDE PHOTOCATHODE 62

5.1 Spicer's Three-step Model 65

5.2 Multiphoton Processes 69

5.3 QE Measurement for a Cs_2Te Photocathode 72

5.4 Multiphoton Photomission from Cs_2Te using 800-nm IR Laser 78

6 FIELD EMISSION CATHODES IN RF SOURCE 87

6.1 Theory of Field Emission 87

Chapter Page

6.2 Motivation 90

6.3 Diamond Field Emission Array Cathode in RF Gun 92

6.3.1 Numerical Simulations 94

6.3.1.1 Electromagnetic Modelling 94

6.3.1.2 Beam Dynamics Simulations 99

6.3.2 Experiment 106

6.3.2.1 FN Characteristics 109

6.3.2.2 Transverse Beam Density and Current Stability . . . 109

6.4 Carbon Nanotube Cathode in RF gun 111

6.4.1 Numerical Simulations 114

6.4.1.1 Electromagnetic Modeling 114

6.4.1.2 Beam Dynamics Simulations 118

6.4.2 Experiment 120

6.4.2.1 FN Characteristics 120

6.4.2.2 Beam Bunching 123

6.4.2.3 Transverse Beam Characteristics and Current Stability 126

7 BEAM APPLICATION STUDIES 129

7.1 Design of Inverse Compton Scattering Experiment 129

7.1.1 Introduction and Motivation 129

7.1.2 Experimental Setup 132

7.1.3 Measurement 138

7.1.4 Conclusion 139

Chapter Page

7.2 Generation of Ellipsoidal Electron Bunches using Cesium Telluride Photocathode 140

7.2.1 Introduction and Motivation 140

7.2.2 Numerical Simulations 141

7.2.3 Experiment 142

7.2.4 Conclusion 146

7.3 Temporal Beam Shaping using Birefringent Crystals 147

7.3.1 Introduction and Motivation 147

7.3.2 Experiment 149

7.3.3 Conclusion 152

8 CONCLUSION. 154

REFERENCES 156

LIST OF TABLES

Table Page

3.1 HBESL laser lab primary apparatus model specifications 27

3.2 Typical operating parameters of HBESL's OCTAVIUS system 36

3.3 Typical operating parameters of HBESL's SPITFIRE PRO amplifier. 42

6.1 Important specifications of the finite element modeling of the RF gun 96

6.2 Numerical results of computations of Q-factors of HBESL's RF gun for the cases of large and small cathodes. 117

6.3 Inferred enhancement factors and effective emmssion areas for the cases considered in Figs. 6.32 and 6.33. 125

7.1 Important experimental specifications of the ICS experiment. 136

7.2 Estimated fit parameters for the plots in Fig. 7.13 for four θ values. 151

LIST OF FIGURES

Figure Page

2.1 A schematic and a photograph of the HBESL photoinjector beamline configuration. 7

2.2 A 3D computer aided drawing (CAD) sectional view of HBESL's RF gun. 8

2.3 Accelerating gradient of the π-mode along the gun when the field is positive at the cathode center. 9

2.4 A numerical simulation of horizontal deflection of an electron as a function of TDC phase for an arbitrary initial phase and peak electric field. 11

2.5 An experimental phase–deflection data of the TDC obtained at HBESL. 12

2.6 A general schematic of the HBESL RF trigger system. 12

2.7 HBESL's typical cumulative solenoidal axial magnetic field (B_z), and the axial derivative ($\frac{dB_z}{dz}$) on beam axis. 14

2.8 A schematic (top view) of the beam transverse size and distribution measurement. 16

2.9 A schematic of the measurement of the beam's x-emittance using the multi-slit method. 17

3.1 A graphical representation of carrier and envelope functions of an ultrashort light pulse. 21

3.2 Superposition of cosine waves 24

3.3 A schematic of the primary laser system at HBESL.. 27

3.4 Longitudinal modes sustained in a laser cavity. 29

Figure Page

3.5 The typical spectrum of the Octavius-85M at HBESL 32

3.6 Kerr lens mode locking of a stable cavity with soft apperture 33

3.7 Layout of the Octavius-85M oscillator laser. 35

3.8 A diagram of the Spitfire Pro regenerative amplifier. 38

3.9 Schematic of chirped pulse amplification.. 39

3.10 Spectral intensity of the seed pulse at various stages of CPA. 41

3.11 The principle of AOPDF.. 42

3.12 Pulse duration adjustment using the Dazzler 45

3.13 Pulse spectral shaping using the Dazzler 46

3.14 Production of UV pulses at HBESL through frequency tripling 48

3.15 A typical spectral intensity of the output pulse from HBESL's tripler optics. 49

3.16 A schematic of an SHG FROG setup. 51

3.17 The FROG sonogram and the corresponding pulse field intensity retrieved using a GP algorithm. 52

4.1 Dependence of mean beam energy and the bunch charge output, on the injection phase of the laser. 54

4.2 A diagram of the RF–laser timing. 55

4.3 Schematic of the 81.25-MHz repetition rate locking loop. 56

4.4 A numerically created example 81.25-MHz pulse train signal of the diode and the corresponding FFT. 58

4.5 Schematic of the 1.3-GHz repetition rate locking loop. 59

4.6 Comparison of the jitter from the 81.25-MHz and 1.3-GHz repetition rate locking loops. 60

4.7 A histogram of 70 bins of the data presented in Fig. 4.6 61

Figure Page

5.1 Energy band diagram of a p-type semiconductor. 64

5.2 Schematic of the setup used at the HBESL photoinjector to calibrate the laser energy. 73

5.3 Schematic showing the calibration of detector C with an energy meter. 74

5.4 Energy ($\mathcal{E}$) as a function of detector C voltage. 75

5.5 Detector C voltage as a function of detector P voltage. 76

5.6 Charge emitted as a function of detector P voltage. 77

5.7 Charge emitted as a function of UV laser energy. 78

5.8 IR Laser energy ($\mathcal{E}_{IR}$) as a function of detector P voltage. 79

5.9 Images of the laser beam corresponding to the three spot sizes considered. 80

5.10 Charge dependence on the laser–gun relative phase. 81

5.11 Charge variation with IR laser energy. 82

5.12 Logarithmic plots of charge vs. energy. 83

5.13 log-log plots of charge density vs. laser intensity. 84

5.14 The effect of the accelerating gradient on the charge yield. 85

5.15 Comparison of the QE among the three spot sizes considered in this study. 86

6.1 Potential energy of an electron near the surface of a metal. 88

6.2 Enhancement of electric field around a metallic tip inside a capacitor. 89

6.3 An SEM image of the DFEA pattern and an SEM image of a single tip. 92

6.4 A photograph of the DFEA cathode brazed on an HBESL cathode plug. 93

Figure Page

6.5 Finite element model of the HBESL RF (quarter) gun. 95

6.6 Effect of the cathode displacement on the π-mode eigenfrequency and the peak electric field on the cathode surface. 97

6.7 The accelerating gradient profiles near the cathode for different cathode displacements.. 98

6.8 The 10-nm radius tip on a pyramid introduced on the cathode surface and the field enhancement profile in the neighborhood of the tip. 98

6.9 The electric field distribution on a 20-nm diameter nanotip for an arbitrary peak electric field. 99

6.10 A scatter plot of an FN charge density distribution on the nanotip corresponding to the electric field represented Fig. 6.9 for an arbitrary total charge. 100

6.11 FN current density corresponding to a sinusoidal (temporal) macroscopic electric field. 102

6.12 Evolution of transverse (x, y) and longitudinal (z) normalized emittance (ϵ) and rms beam size (σ) of the beam emitted from a single nanotip, along the beamline. 103

6.13 Transverse (x) phase space and the corresponding projection at $z =$ 1 m of the beam emitted from a single nanotip. 103

6.14 Longitudinal phase space distribution of the bunch emitted by a single nanotip at $z = 1$ m and the corresponding projections. 104

6.15 A scatter plot of the particle distribution on a nanotip with the number of particles reduced to 51, from previously 198. 105

6.16 An array of 25 tips arranged in 5 rows and 5 columns. 106

6.17 Evolution of the transverse and longitudinal normalized emittance (ϵ) and the rms beam size (σ) of the beam emitted from a 40,000-tip array, along the beamline. 107

6.18 Transverse (x) phase space and the corresponding projection at $z =$ 1 m, of a beam emitted from a 3600-tip array. 107

6.19 Evolution of ϵ_x, σ_x and $\sigma_x^{'}$ with the number of tips in the array. . . . 108

Figure Page

6.20 Current traces recorded with the DFEA cathode for 1.2, 1.3, and 1.5 MW forward power. 108

6.21 F-N plots and the corresponding characteristic curves for the nominal and retracted cathode positions.. 110

6.22 The measured transverse density of the beam at X3 with solenoids off, and focused with solenoids turned on corresponding to the accelerating gradients of 23.5 MV/m and 31 MV/m respectively. 111

6.23 Longterm current stability studies for two cases of electric field values. 112

6.24 An SEM image of the large CNT cathode with a magnification of 20k showing CNTs and other structures, a picture of the large CNT cathode, and a picture of the small CNT cathode. 113

6.25 The cross-section of the (quarter) gun near the cathode region for the case of small cathode. 116

6.26 Comparison of surface resistive loses for the two cases of the large and small cathodes in RF gun's π-mode. 118

6.27 Longitudinal electric field along the axis (z) and along the radial coordinate (r) of the gun for the case of small cathode.. 119

6.28 Comparison of spectrum and network analyzer measurements of HBESL's RF gun for the cases of small and nominal (flat) cathodes. 120

6.29 Evolution of transverse (x, y) and longitudinal (z) normalized emittance (ϵ) and rms beam size (σ) of the beam emitted from a CNT cathode, along the beamline. 121

6.30 Transverse (x) phase space and the corresponding projection at $z =$ 1 m for the CNT cathode. 121

6.31 Longitudinal phase space distribution of the bunch emitted from a CNT cathode at $z = 1$ m and the corresponding projections.. 122

6.32 Measured average current as a function of applied macroscopic field and the corresponding FN plots for the large cathode. 123

6.33 Measured average current as a function of applied macroscopic field and the corresponding FN plots for the small cathode. 124

Figure Page

6.34 Voltage signal (large cathode) from the electromagnetic pick-up and the corresponding FFT. 125

6.35 Emittance measurement snapshots showing the beam's transverse distribution at X3 for the small cathode 126

6.36 Current stability over a > 6-hour period for 100, 300 and 650 mA current. 127

7.1 A diagram of an ICS scenario in the laboratory frame. 130

7.2 A Schematic of the ICS experiment. 133

7.3 Design of the ICS interaction chamber. 134

7.4 CCD images of the laser and the electron beams at the IP. 135

7.5 ICS signal as a function of laser path delay and the corresponding Gaussian fit. 139

7.6 ASTRA simulations of the evolution of the electron beam profile as a function of charge density. 143

7.7 The transverse distribution ($x \propto t$) profile of the beam for different charge densities. 144

7.8 A gray-scale image of the laser transverse distribution as detected on the virtual cathode. 145

7.9 The transverse trace space of the beam measured at X3 for the different charge values shown.. 146

7.10 x-emittance as a function of the charge density corresponding to the beam's trace space distributions shown in Fig. 7.9. 146

7.11 A diagram explaining principle of birefringence. 149

7.12 A diagram explaining the expected pattern of the charge vs. laser–RF relative phase for the twin bunches.. 150

7.13 $Q - \phi$ plots for different θ values. 151

7.14 The electron beam on X7 screen with the TDC turned off, and turned on revealing the twin bunches. 152

7.15 The spatial separation of the twin bunches on X7 screen downstream of the TDC as a function of E_T. Also shown is the $\delta t - \delta s$ calibration. 153

CHAPTER 1

INTRODUCTION

Particle accelerators are extensively used in industry, medicine and scientific research. Accelerators have extraordinary potential to address future energy needs and reduce emissions for safer environmental impact. For instance, accelerator based technology can be used in nuclear waste transmutation for nuclear power generation, and in chemical-free water treatments [1]. Electron accelerators, in particular, have industrial applications like materials processing, cargo inspection and sterilization [2]; and medical applications like radiation therapy [3] and radiology. The radiation power P in vacuum, generated by an accelerating relativistic charged particle with a charge q is given by the Lienard's generalization of Larmor's formula as [4]

$$P = \frac{\mu_0 q^2 \gamma^6}{6\pi c}\left[a^2 - \left|\frac{\boldsymbol{v}\times\boldsymbol{a}}{c}\right|^2\right] \tag{1.1}$$

where μ_0 is the magnetic permeability of vacuum, c is the speed of light, $\boldsymbol{v}$ and $\boldsymbol{a}$ are respectively the velocity and acceleration of the particle, and $\gamma = \sqrt{\frac{1}{1-(\frac{v}{c})^2}}$ is the Lorentz factor. Equation 1.1 implies that P steeply increases with γ. An electron with an energy $\mathcal{E} = 5.2$ MeV ($\equiv \gamma m_e c^2$, where m_e is the electronic mass) has a $\gamma > 10$ due to its low mass, contrary to a proton which has a $\gamma \approx \frac{10}{1836}$ for the same energy because of its significantly higher mass. Hence, electron beams are especially important as radiation sources because of their ability to readily radiate at modest energies. They can also be used in beam-driven schemes to advance

the energy frontier in elementary particle physics [1]. Development of compact and portable electron beam sources can therefore pave ways to compact accelerator-based radiation sources. For example, compact electron accelerator-based radiation sources can support in x-ray therapy [1], and in THz-based time-resolved studies of proteins in biology [5].

Generation of high charge and high current beams is key to modern applications of charged particle beams like electron-beam welding and klystrons [6]. High quality electron beams are widely required in vacuum micro-electronics [7] e.g. in field emission displays.

The primary goal of this dissertation was to investigate electron emission processes including nonlinear photoemission from semiconductor cathodes and field emission from carbon based cathodes [8]. The emphasis was to explore charge emission processes that could be more efficient or simpler than traditional processes (e.g. linear photoemission). In the process, we established a compact accelerator test facility, the High Brightness Electron Source Laboratory (HBESL) which was used to carry out our studies. Additionally, the facility was used to demonstrate possible applications of high brightness beams including the production of radiation via inverse Compton scattering, the formation of uniformly filled ellipsoidal bunches (which are immune to space charge induced degradation) and the generation of temporally shaped twin bunches.

This dissertation is organized into eight chapters. Chapter 2 describes the HBESL photoinjector and introduces accelerator physics concepts relevant to the experiments. Chapter 3 discusses the theory of pulsed laser generation for photoinjection and presents the HBESL laser system and its experimental characterization. Chapter 4 describes the HBESL laser system's synchronization upgrade. With the appropriate background set, Chapter 5 is dedicated to linear and multiphoton (non-

linear) photoemission studies from Cesium Telluride (semiconductor) photocathode. Chapter 6 focuses on the field emission from diamond field emission array and carbon nanotube cathodes located in a radio frequency gun. Chapter 7 discusses three electron beam application experiments: i) inverse Compton scattering using a $\sim$ 4-MeV electron beam and a 800-nm wavelength laser ii) temporal bunch shaping using nonlinear birefringent crystals, and iii) ellipsoidal bunch generation from Cesium Telluride photocathode. Finally, Chapter 8 concludes with the summary and future implications of the work presented in this dissertation.

CHAPTER 2

HBESL PHOTOINJECTOR AND RELATED ACCELERATOR PHYSICS

2.1 Pertinent Beam Dynamics Concepts

A photoinjector generates relativistic electron beams via photoemission from a photocathode typically located inside a radio frequency (RF) gun. In photoemission, electrons are emitted when photons of certain energy impinge on a photocathode. The emitted electrons (bunch) are then rapidly accelerated using high gradient RF electric fields (tens of MV/m) inside the RF gun. Photoinjectors have become reliable sources of producing electron beams for collider experiments, x-ray sources and advanced accelerator R&D [9]. The quality of a charged particle beam is often characterized by its emittance and brightness. If we denote $u \in \{x, y, z\}$ as a spatial coordinate and p_u as the corresponding canonical momentum of a particle in the beam, then the parameter space of $u - p_u$ is called the phase space. The canonical emittance of a beam refers to the area in the phase space occupied by all the particles in the beam and is statistically defined as

$$\tilde{\epsilon_u} = \frac{1}{m_e c}\sqrt{\langle u^2\rangle\langle p_u^2\rangle - \langle up_u\rangle^2} \tag{2.1}$$

where m_e is the electronic mass and c is the speed of light. The notation $\langle\ \rangle$ indicates the statistical average over all particles in the beam. Often, the normalized

emittance ϵ is convenient to use and is given for each phase space plane (z is the coordinate along the direction of beam propagation) as

$$\epsilon_x = \beta\gamma\sqrt{\langle x^2\rangle\langle x'^2\rangle - \langle xx'\rangle^2}, \tag{2.2}$$

$$\epsilon_y = \beta\gamma\sqrt{\langle y^2\rangle\langle y'^2\rangle - \langle yy'\rangle^2}, \tag{2.3}$$

$$\epsilon_z = \beta\gamma\sqrt{\langle z^2\rangle\langle \delta^2\rangle - \langle z\delta\rangle^2}, \tag{2.4}$$

where $x' \equiv \frac{p_x}{\langle p_z\rangle}$ and $y' \equiv \frac{p_y}{\langle p_z\rangle}$ are the x and y divergences respectively, $\gamma \equiv \frac{\langle p_z\rangle}{m_e c}$ is the Lorentz factor, $\beta = \sqrt{1-\frac{1}{\gamma^2}}$, and $\delta \equiv \frac{p_z - \langle p_z\rangle}{\langle p_z\rangle}$ is the fractional momentum spread. On the other hand, brightness of an electron beam incorporates the charge Q of the bunch and can be defined in 6D phase space as

$$B = \frac{Q}{\epsilon_x\epsilon_y\epsilon_z}. \tag{2.5}$$

Emittance of a charged particle beam grows after its generation due to the Coulomb forces the individual particles exert on one another, referred to as space charge forces. The space charge forces are eventually suppressed when the beam becomes relativistic after sufficient acceleration. From the point of generation to the point of application, a beam may travel a long path, so it is important to contain the beam to a small transverse size. This is accomplished with focusing magnets such as quadrupole magnets or solenoidal lenses.

2.2 Overview of HBESL Photoinjector

2.2.1 Introduction and General Layout

The HBESL photoinjector was reconfigured early 2012 upon decommissioning of the A0 photoinjector (A0PI). The approximately 13-m long A0PI was reconfigured to the current $\sim$ 7-m long HBESL photoinjector. A key difference between HBESL and its predecessor A0PI is that HBESL lacks the superconducting RF (SRF) accelerating cavity A0PI had, limiting the maximum energy of the electron beam to $\sim$ 4 MeV, compared to A0PI's 16-MeV beam. The general layout of HBESL photoinjector is depicted in Fig. 2.1 (a). The beamline is evacuated to ultra-high vacuum (UHV) levels (2-4 nTorr) with ion pumps installed at various locations. Ion gauges are employed to monitor the vacuum pressure. The photocathode laser system is described in Chapter 3. The laser beam is directed towards the photocathode through an injection port. Under nominal operation, the electron beam is dumped in the beam dump located downstream of XS; see Fig. 2.1 (a). When the spectrometer located towards the end of the beamline is turned off, the beam is directed to another beam dump using a pair of bending magnets. An inverse Compton scattering (ICS) setup and a photodiode are installed downstream of the spectrometer for the ICS experiment which is discussed in Chapter 7.

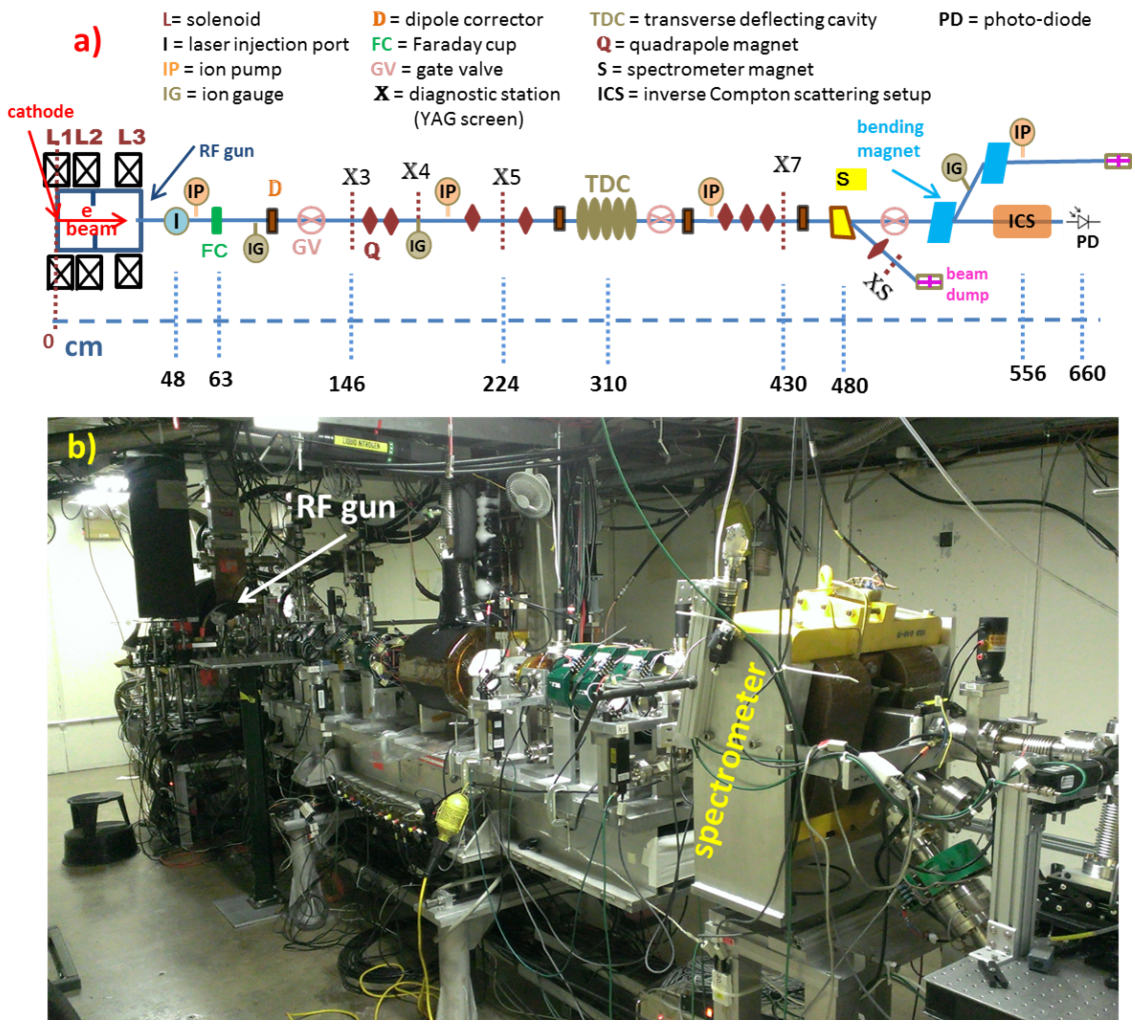

Figure 2.1: A schematic (a) and a photograph (b) of the HBESL photoinjector beamline configuration.

2.2.2 Radio Frequency Components

2.2.2.1 RF Gun

The facility incorporates an RF gun powered by a klystron capable of producing up to 3-MW pulsed power. In an RF gun, the emitted charge—regardless of the

method of charge generation—is accelerated by a standing RF wave with a time dependent E-field with a large component along the axial direction. An RF gun is carefully designed to support such a mode of RF wave for the given frequency. HBESL's RF gun is a 1.625-cell cavity that operates in $TM_{010,\pi}$ mode, aka the π-mode at a fundamental frequency 1.3 GHz. The two cells of the gun are casually referred to as the full cell (bigger cell) and the half cell; see Fig. 2.2. In the π-mode, the electric field is maximum at the cathode surface (center of gun). The axial electric field profile of the π-mode along the beam axis is shown in Fig. 2.3. When an electron bunch is emitted from the photocathode located at the center of the back plane of the gun (see Fig. 2.2) at the right phase of the RF, the bunch quickly gets accelerated and reaches relativistic speeds. This allows the particles to stay in phase with the RF and remain bunched as the electron bunch duration (<1 ps) is much smaller than the RF period ($\approx$ 769 ps).

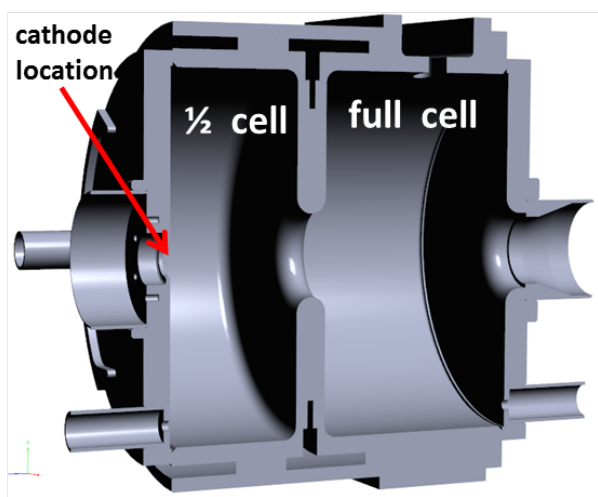

Figure 2.2: A 3D computer aided drawing (CAD) sectional view of HBESL's RF gun.

The photoinjector beamline includes a load-lock system behind (upstream) the RF gun that permits cathode transfer to the gun from a cathode storage chamber

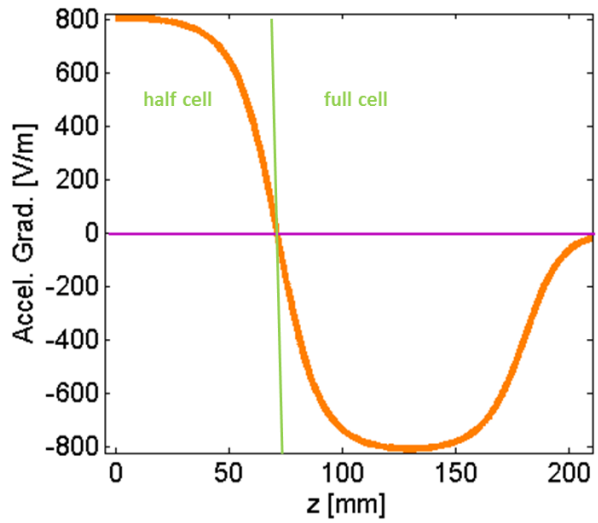

Figure 2.3: Accelerating gradient (E-field) of the π-mode along the gun when the field is positive at the cathode center, for an arbitrary peak field.

without having to break the vacuum. Once a cathode is inserted into the gun using the load-lock system, the gun's frequency is tuned to 1.3 GHz $\pm$100 KHz by adjusting the axial position of the cathode plug assembly. A network analyzer is used to measure the resonant frequencies of the gun (see Fig. 6.28). The cathode plug is electrically connected to the RF gun and to the ground via a circular copper-Beryllium spring (Cu-Be) that surrounds the plug at the insertion surface.

2.2.2.2 Transverse Deflecting Cavity

The transverse deflecting cavity (TDC), which has 5 cells, allows to diagnose the temporal distribution of the beam. The TDC runs in a TM_{110} mode (at a frequency ν = 3.9 GHz) and imparts a linear correlation between the temporal position (t) in the beam and the horizontal position (x) as detected on the YAG screen at X7 (see Section 2.2.4.1) downstream of the TDC. The non-zero electromagnetic fields

inside a cylindrically symmetric pillbox resonating cavity operating in TM_{110} mode are given in cylindrical coordinates $\{r, \phi, z\}$ as [10]

$$E_z = E_0 J_1\Big(\frac{k_1 r}{R}\Big)\cos(\phi)\cos(2\pi\nu t), \tag{2.6}$$

$$B_r = E_0 \frac{2\pi\nu R^2}{Z_0 c k_1^2 r} J_1\Big(\frac{k_1 r}{R}\Big)\sin(\phi)\sin(2\pi\nu t), \tag{2.7}$$

$$B_\phi = E_0 \frac{2\pi\nu R}{Z_0 c k_1} J_1'\Big(\frac{k_1 r}{R}\Big)\cos(\phi)\sin(2\pi\nu t), \tag{2.8}$$

where E_0 is the electric field amplitude, $k_1 = 3.832$ is the first root of the first order Bessel function $J_1(x)$, R is the radius of the cavity, Z_0 is the impedance of the free space, and ν is the resonating frequency. The non-zero longitudinal electric field gradient $E_z' \equiv \frac{dE_z}{dx}$ along with the vertical (y) magnetic field imparts a transverse (x) force for axially traversing electrons [10]. A small-argument expansion of Eq. 2.6 gives

$$E_z \approx x\Big[\frac{E_0}{R}\cos(2\pi\nu t)\Big]. \tag{2.9}$$

From applying the Maxwell's equation $\boldsymbol{\nabla} \times \boldsymbol{E} = \frac{\partial \boldsymbol{B}}{\partial t}$ to Eq. 2.9 we get $B_y = \frac{E_0}{2\pi\nu R}\sin(\pi\nu t)$ and $B_x = B_z = 0$ (since $E_r = E_\phi = 0$). Figure 2.4 shows how an electron, or the center of an electron beam, is deflected by the TDC operating in the horizontal (x) deflecting mode with an arbitrary peak electric field, based on the TDC phase.

The TDC phase at which there is zero deflection (see Fig. 2.4) is referred to as a point of zero-crossing. When an electron beam of finite length encounters a point of zero crossing at its center inside the TDC, the head and the tail of the beam *see* deflecting fields in opposite directions while the beam center remains undeflected.

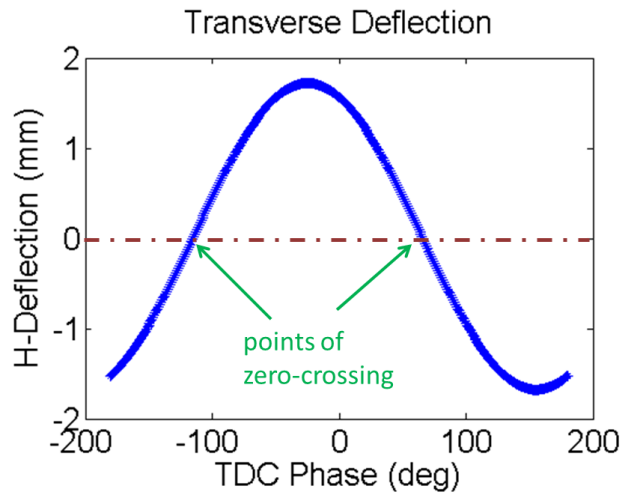

Figure 2.4: A numerical simulation of horizontal deflection of an electron as a function of TDC phase for an arbitrary initial phase and peak electric field.

This allows for the $t - x$ coordinate linear mapping (at X7) given as $x \propto Kt$ where $K \simeq \frac{eE_0}{\gamma m_e c} \times \frac{2\pi\nu}{c} L$ where E_0 is the peak electric field, ν is the TDC frequency and L is the distance between the center of the TDC and the YAG screen (X7) [11]. Hence, an electron beam deflected by the TDC (centre deflection = 0) has $\sim t \propto z \propto x$ for a small transverse size. Figure 2.5 shows an experimental phase–deflection data of the TDC at HBESL.

For the peak-to-peak x-deflection $\Delta x = 13$ mm from Fig. 2.5, L = 1.2 m and beam energy $\mathcal{E} = 4$ MeV, we can estimate $E_0 = \frac{\Delta x \mathcal{E}}{2L} = 21.6$ keV.

2.2.2.3 RF System

Figure 2.6 shows the general overview of the RF trigger system. A master oscillator clock produces a 1.3-GHz RF wave signal that is amplified in a klystron (Klystron 1 in the figure). RF power is sent from Klytron 1 to the RF gun through a wave guide at a rate of 0.5 Hz, whose trigger signal is supplied by down-converting the

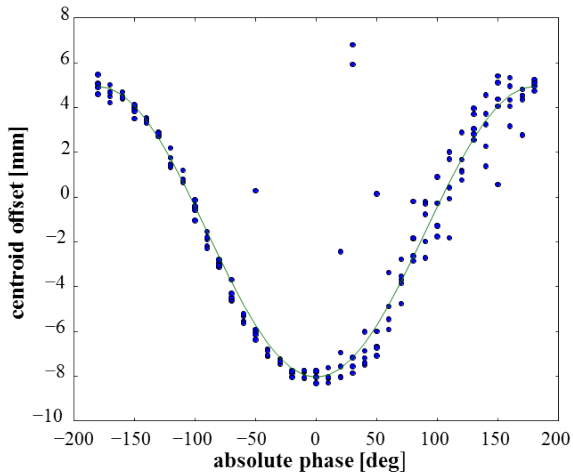

Figure 2.5: An experimental phase–deflection data of the TDC [12] obtained at HBESL. The line is a fit to the data points.

master oscillator's 1.3-GHz signal. The 3.9-GHz TDC described in Section 2.2.2.2, also is triggered the same way as the RF gun (see Fig. 2.6); but the 3.9-GHz RF signal is obtained by up-converting the master oscillator's signal. The amplified 3.9-GHz RF power is directed into the TDC through a waveguide by Klystron 2 at the rate of 0.5 Hz. A phase shifter is employed for the TDC to adjust its RF relative phase with respect to the RF gun.

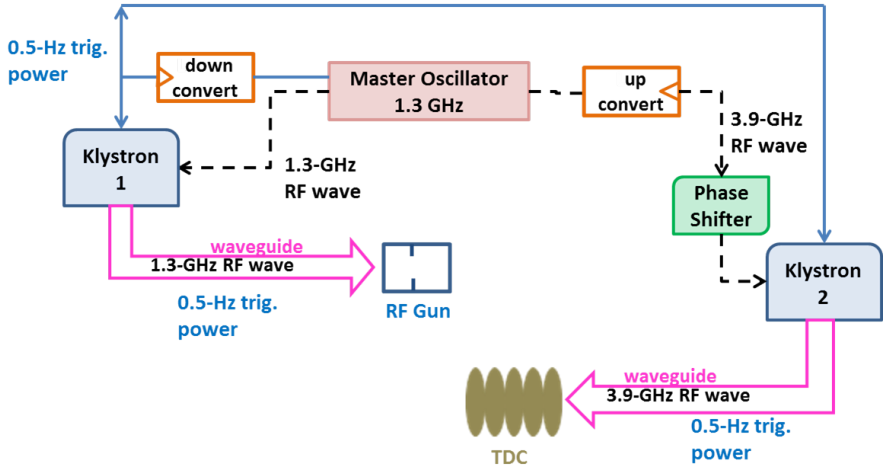

Figure 2.6: A general schematic of the HBESL RF trigger system.

The forward RF power, P, injected into the RF gun cavity is measured using a calibrated RF diode detecting the low power from a -60 dB directional coupler installed on the RF waveguide. The peak electric field at the cathode surface is calculated from the measured forward power (P) using numerically obtained relation $E[MV/m] \simeq 2.234 \times 10^2 \sqrt{P[MW]}$, where the gun's quality factor (see Section 6.4.1.1) is taken to be $Q_\eta \simeq 2.3 \times 10^4$ while the cathode surface is assumed to be co-planar with the gun's back plane [13, 14].

2.2.3 Magnets

2.2.3.1 Solenoids

The RF gun is nested in three magnetic lenses viz. L1 , L2 and L3 [see Fig. 2.1 (a)] referred to as solenoids that are nominally used to control the beam divergence and transverse emittance. L1 and L2 are generally operated at equal magnetic strengths to maintain a zero magnetic field on the cathode surface in order to minimize the initial transverse beam emittance growth that can be induced by the magnetic field [13]. A radial magnetic field $B(r, z) \simeq -\frac{r}{2}\frac{dB_z}{d_z}$ induced by the longitudinal magnetic field gradient $\frac{dB_z}{dz}$ provides a focusing effect to the beam. Figure 2.7 shows the axial magnetic field and the corresponding derivative for a typical operation at HBESL.

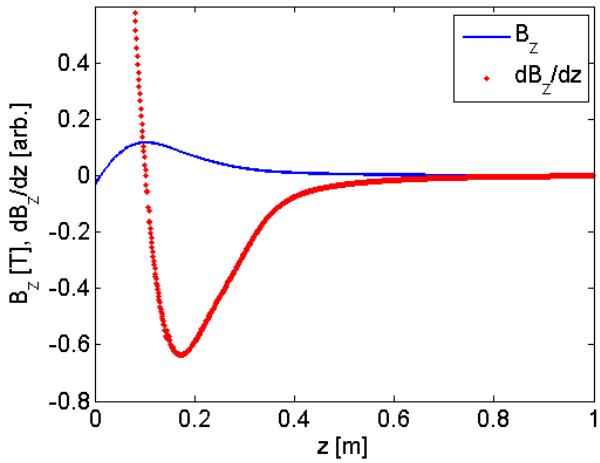

Figure 2.7: HBESL's typical cumulative solenoidal axial magnetic field (B_z), and the axial derivative ($\frac{dB_z}{dz}$) on beam axis.

2.2.3.2 Dipole and Quadrupole Magnets

The beamline incorporates several dipole 'steering' magnets to direct the beam along the axis of the beamline. By varying the strength of the dipole magnets, the electron beam's bending angle can be adjusted to alter the direction of beam travel, thus allowing for beam steering for alignment.

There are several quadrupole magnets available for transverse ($x - y$) focusing of the beam. When a beam passes through the center of a quadrupole magnet, it is focused in one axis and defocused in the perpendicular axis. Sequently, when the beam passes through a quadrupole with opposite polarity that follows the first quadrupole, the focusing and defocusing axes are interchanged from before; this provides a net focusing in both axes as the beam passes through the magnet pair. For this reason, generally quadrupole magnets are arranged in pairs, with each pair consisting of a symmetric and its anti-symmetric (opposite polarity) magnet. (A vertical spectrometer magnet is employed on the beamline at $\simeq$ 4.8 m from the

cathode for the measurement of the mean energy and energy spread of the beam, which is discussed in Section 2.2.4.3.)

2.2.4 Beam Diagnostics

2.2.4.1 Transverse Beam Diagnostics

Beam diagnostic stations X2, X3 etc. have insertable scintillating Ce:YAG (Cerium doped Yttrium Aluminum garnet) screens which allow for the measurement of the beam's position and transverse distribution at the respective locations. The beam is intercepted by a YAG screen with its normal at 45^0 with respect to the beam direction; see Fig. 2.8. When an electron beam hits a YAG screen, the beam produces fluorescence light in the visible spectrum, thus allowing for the beam detection. All screens are imaged using charge-coupled device (CCD) digital cameras as shown in Fig. 2.8. When needed, a variable iris and neutral density filters are used to attenuate emitted optical radiation and mitigate saturation of the CCD cameras. The calibration of the beam size is done by taking the YAG screen size (≈ 1 inch) as a reference. An image of the electron beam's distribution as noted on a YAG screen is shown in Fig. 6.22.

The transverse laser beam profile on the photocathode is imaged onto a virtual cathode located outside the beamline by utilizing a reflection of the laser beam from the injection port. The virtual cathode also is imaged using a CCD camera; see Fig. 7.8.

Transverse emittance measurement: the beamline is equipped with insertable vertical slits at X3 to measure the beam's x-emittance (horizontal) utilizing

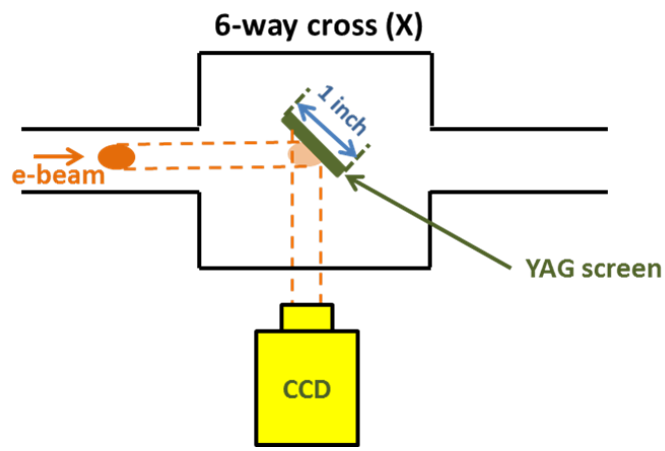

Figure 2.8: A schematic (top view) of the beam transverse size and distribution measurement.

the multi-slit method [15] instead of standard envelope techniques, as typically the beam has significant space charge effects [16]. The slits are 50-μm wide with an inter-slit separation of 1 mm, located on a 6-mm thick tungsten screen [17]. When inserted, the beam is masked by the tungsten screen producing beamlets originating from the transmitted beam through the slits as shown in Fig. 2.9. A measurement of the beamlet (average) rms size (σ_B) at X5 provides information on the beam's intrinsic x-divergence $\sigma_x^{'} \simeq \frac{\sigma_B}{L}$ at X3. Together with a measurement of the rms transverse beam size σ_x at X3, the divergence yields the value of the normalized x-emittance as $\epsilon_x = \beta\gamma\sigma_x^{'}\sigma_x$ [15]. $\gamma = \frac{\mathcal{E}}{m_e c^2}$ is calculated from measuring the mean energy $\mathcal{E}$ of the beam using the spectrometer as described in Section 2.2.4.3. An example of an emittance measurement with the reconstructed trace space appears in Fig. 6.35.

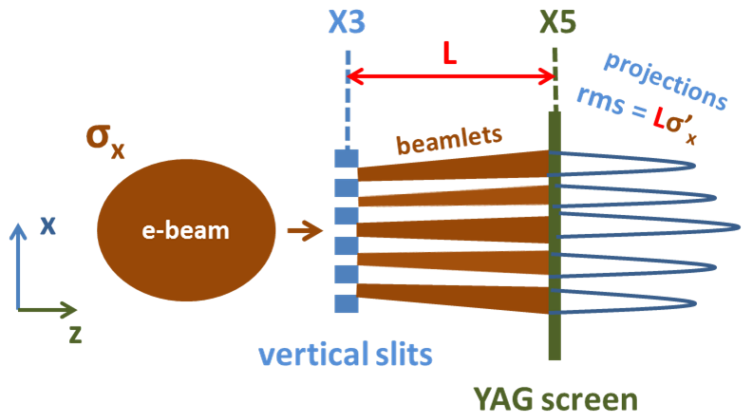

Figure 2.9: A schematic of the measurement of the beam's x-emittance using the multi-slit method.

2.2.4.2 Charge Measurement

An insertable Faraday cup (FC) located at X2 measures the bunch charge in the range of tens of pC to a nC. An FC is a metal cup that when hit by an electron beam absorbs the total charge of the beam, thus becoming negatively charged. The acquired charge is discharged to the ground and the corresponding current $I(t)$ (where t is time) is measured using an oscilloscope. The total charge is thus given by $Q = \int I dt$. For beams with $Q > 100$ pC, an integrating current transformer (ICT) that is cross-calibrated with the FC can be used for a non-destructive charge measurement. The ICT is a special transformer where the current generated by an electron beam passing through the center of the device induces a current with identical current profile of the passing bunch. This current charges a capacitor which stores a charge equal to the bunch charge. The capacitor slowly (compared to bunch duration) discharges into the output winding connected to an oscillator circuit producing a current $I_{out}(t)$. The charge of the bunch can be obtained by integrating the

output current as $Q = \int I_{out} dt$ on the oscilloscope. While the temporal information of the bunch is lost, the charge information is preserved.

2.2.4.3 Energy Measurement

Towards the end of the beamline, a vertical spectrometer magnet is employed to measure the mean energy and the energy spread of the beam. Downstream of the spectrometer, there is a 45° section of beam pipe that leads to a beam dump. This section has the diagnostic station XS $\approx$ 118 cm from the center of the spectrometer (see Fig. 2.1). If an electron with charge e and speed v enters the spectrometer's magnetic field with magnitude B and a direction perpendicular to the electron's velocity, then we have

$$eB = \frac{m_e v}{\rho} \tag{2.10}$$

by equating the Lorentz force acting on the electron with the centripetal force; where ρ is the bending radius of the electron's trajectory. From using the equation $\mathcal{E} = \gamma m_e c^2$ ($\mathcal{E}$ is the total energy of the electron), it can be shown from Eq. 2.10 that

$$B\rho = \frac{1}{ec}\sqrt{\mathcal{E}^2 - (m_e c^2)^2}. \tag{2.11}$$

For an electron with kinetic energy T [MeV] ($\equiv (\mathcal{E} - m_e c^2)$), with ρ expressed in cm and B in kG ($\equiv$ 0.1 T), we get [18]

$$T = \sqrt{0.09 B^2 \rho^2 + (m_e c^2)^2} - m_e c^2. \tag{2.12}$$

For a constant magnetic field, and a bending angle $\theta = 45^o$ ($\equiv \frac{\pi}{4}$ rad), we have $\rho = \frac{l}{\theta} = \frac{4l}{\pi}$ where l is the length of electron travel in the spectrometer. Thus the mean energy of the electron beam can be calculated by adjusting the experimental B value such that the center of the beam corresponds to the center of the YAG screen at XS; from that B value and ρ, T can be calculated using Eq. 2.12. It can be noted that, the spread in energy of the beam correlates to the spread in the vertical size of the beam at XS, since for a given B an individual electron in the beam has $\theta \propto \frac{1}{\mathcal{E}_e}$ where $\mathcal{E}_e$ is its energy. The energy spread of the beam can be estimated as the measured difference in the energies of the vertical extremities of the beam at XS. Based on the current I needed to bend the beam by 45^0, the mean longitudinal momentum of the beam was calibrated as $p_z[\text{MeV}/c] = 1.619I[\text{A}]$ [13].

CHAPTER 3

PULSED LASER GENERATION FOR PHOTOINJECTION

Photoemission of short electron beams relies on short laser pulses. The initial bunch duration of a photo-emitted electron beam (e-beam) also depends on the response time of a given photocathode. Metallic photocathodes are considered as 'prompt' which means the initial electron bunch duration is approximately equal to the drive laser pulse duration used for the photoemission. Semiconductor photocathodes have longer response times, but, still can produce e-beams on the order of several hundreds of femtoseconds provided the drive laser pulses are short enough. Laser pulses of a few hundreds of femtoseconds or less are referred to as ultrashort pulses. Ultrashort laser pulses also give an advantage of generating high peak powers and in turn can generate higher current e-beams through photoemission. Besides photoemission, there are numerous other uses of high peak power laser pulses in accelerator technology, which include but not limited to inverse Compton scattering experiments and laser-driven acceleration and manipulation techniques [19].

3.1 Mathematical Representation of a Light Pulse

The equation of a monochromatic light wave propagating in one direction, say along the z-coordinate, can be given by its oscillating electric field magnitude in complex form (here represented with a tilde) $\tilde{E}$ in time t as a plane wave $\tilde{E}(t) =$

$e^{i(kz-\omega t+\phi)}$, where ω is the angular frequency, k $(= \frac{2\pi}{\lambda})$ is the wave number, ϕ is the initial phase, λ is the wavelength and $i = \sqrt{-1}$. An ideal plane wave extends infinitely in space and time, so in practice, ideal plane waves are rarely relevant to a real system. An ultrashort light pulse, on the other hand, has a broad frequency spread $(\Delta\omega)$ and very short duration which is explained in the following section, and can be represented as [20]

$$\tilde{E}(t) = \frac{1}{2}\tilde{\Lambda}(t)e^{i\omega_0 t}, \tag{3.1}$$

where $\tilde{\Lambda}(t)$ is the complex envelope and ω_0 is called the carrier frequency. The complex envelope can be written in terms of the real envelope $\Lambda(t)$ as $\tilde{\Lambda}(t) = \Lambda(t)e^{[i\phi(t)+\phi_0]}$, where ϕ_0 is the phase difference between the carrier and envelope functions referred to as 'carrier to envelope phase'. Equation 3.1 is valid in the regime $\frac{\Delta\omega}{\omega_0} \ll 1$ which is applicable for ultrashort pulses. An example of the graphical representation of an ultrashort light pulse is shown in Fig. 3.1.

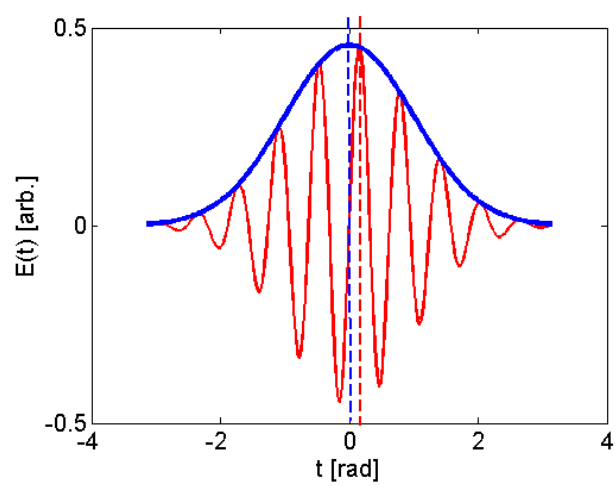

Figure 3.1: A graphical representation of carrier and envelope functions of an ultrashort light pulse. The blue and red curves correspond to the envelope and the electric field respectively. The phase difference between the red and blue dashed lines is ϕ_0.

A complete description of an ultrashort pulse includes a spatial function, say $S(x_\perp, z)$, to describe the spatial variation of the electric field along the direction of propagation z and the perpendicular coordinates $x_\perp$. For a real light pulse, E has to obey Maxwell's equations, therefore the choice of the functions S and Λ can be restricted. For instance, for a radially polarized pulse, S and Λ cannot be Gaussian simultaneously [21].

The instantaneous pulse power $P(t)$ in a dispersionless medium is derived from Poynting theorem as [20]

$$P(t) = cn\epsilon_0 \int_{\mathcal{A}} dS \frac{1}{T} \int_{t-\frac{T}{2}}^{t+\frac{T}{2}} E^2(t')dt', \tag{3.2}$$

where c is the speed of light, ϵ_0 is the dielectric permittivity of the medium, n is the refractive index, T is the period of oscillation and the term $\int_{\mathcal{A}} dS$ represents the integration over the beam cross section $\mathcal{A}$. The corresponding energy $\mathcal{E}$ [J] contained in the pulse is therefore given as $\mathcal{E} = \int_{-\infty}^{+\infty} \mathcal{P}(t')'dt'$. The time dependent intensity $I(t)$, defined as the power per unit area [W/m^2], is given as

$$I(t) = cn\epsilon_0 \frac{1}{T} \int_{t-\frac{T}{2}}^{t+\frac{T}{2}} E^2(t')dt' = \frac{1}{2} c\epsilon_0 \Lambda^2(t). \tag{3.3}$$

In practice, if the duration τ and the total energy $\mathcal{E}$ are known for an ultrashort laser pulse, then $P = \mathcal{E}/\tau$ is taken as an average power by approximating the temporal profile of the pulse to a uniform distribution, for the sake of convenience—which otherwise depends on the temporal profile of the pulse. The intensity profile of a transverse mode of a laser for which the electric and magnetic fields are perpendicular to the direction of propagation, is described using Laguerre polynomials for cylindrically symmetric modes, referred to as TEM$_{pq}$ (transverse electromagnetic) modes, where p, q are the Laguerre polynomial indices [22]. The simplest of the

transverse modes, the TEM_{00} or the Gaussian mode, is given as $I(r) = I_0 \exp^{\frac{-r^2}{2\sigma^2}}$, where I_0 is the intensity at the center, r is the distance from the center and σ is the room mean square (rms) beam size.

3.2 Time–Bandwidth Product of a Light Pulse

We now discuss the theoretical limitations of producing ultrashort pulses of light (in general, of any wave) and then discuss the practical limitations. It turns out that a very short light pulse has to have a very broad frequency distribution within itself, independent of the practical limitations. This is a direct consequence of Fourier analysis. The Fourier transform (FT) of a function $f(x)$ is given as

$$\mathcal{F}(k_x) = \int_{-\infty}^{\infty} dx f(x) e^{-2\pi i x k_x} \qquad (k_x \in R) \tag{3.4}$$

where the variable k_x represents the Fourier conjugate of x. $\mathcal{F}$ is a function (continuous) that gives the amplitude(s) of the *frequencies* of the sine waves $f(x)$ is made of, as a function of the *frequencies*. Given $\mathcal{F}(k_x)$, $f(x)$ can be obtained through the inverse FT as

$$f(x) = \int_{-\infty}^{\infty} dk_x \mathcal{F}(k_x) e^{-2\pi i x k_x} \qquad (x \in R). \tag{3.5}$$

For a given set of functions the existence of the absolute minima of [the spread in] Fourier variable–Fourier conjugate variable product, i.e $\Delta x \Delta k_x$, is implied in the FT formulation. So far x and k_x which form a Fourier variable pair have been kept as general variables. In our context, the variables of interest are time t and angular frequency ω of a light wave which form a Fourier variable pair (ω indeed is

proportional to the energy $h(\frac{\omega}{2\pi})$ of the light wave, where h is the Planck's constant). Therefore, there is an absolute minima for the product $\Delta t \Delta \omega$, which implies that a short light pulse has a broad frequency spread. To demonstrate this statement let us define the real part of the electric field E at a point in space of a light wave comprised of n number of frequencies as $E = \Sigma_1^n A \cos(\omega_n t)$ where the common amplitude $A = 1$ and $\omega_n = n \in \mathbb{N}$. Here we have assigned the initial phases of all frequencies be at 0. We want to see how E evolves with n. In practice, E^2, whose value cannot be negative, is much easier to measure—hence can be used instead of E.

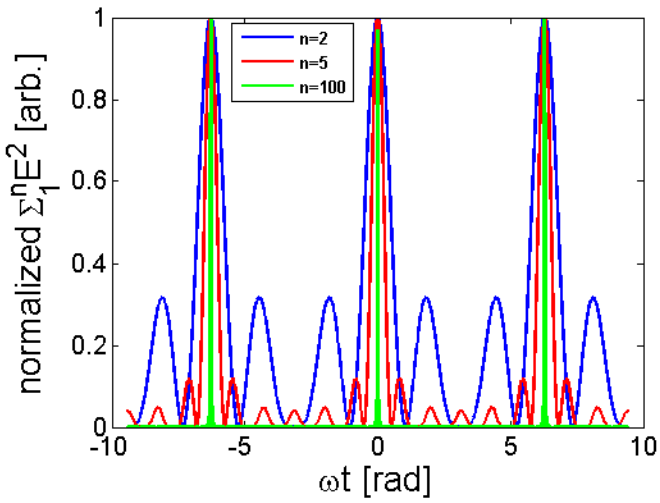

Figure 3.2: Electric field intensity E^2 of light pulses made of different number of frequencies n.

Figure 3.2 shows the normalized E^2 as a function of t for different values of n. It can be noted that as n increases, the pulse width Δt gets shorter and the side peaks tend to disappear. The converse is also true; n cannot be less than a minimum value to obtain a certain Δt ($\equiv \tau$). There is also another important effect; the periodicity of $E^2(t)$ becomes larger with n. In an extreme case, a Dirac delta function in time will have a spectrum with non-vanishing values over the

full frequency domain. These effects are quantitatively expressed in the Fourier uncertainty product relation.

The convention of the width of a function is not trivial, especially if the function has a non uniform shape. In optical science it is customary to use the full width at half maximum (FWHM) of a function which is defined as the width of the function at half of its maximum value. If we consider a laser pulse with Gaussian temporal profile given as $I(t) = I_0 e^{\left(\frac{-t^2}{2\sigma_t^2}\right)}$, where $I_0 = I(0)$ and σ_t is the standard deviation (rms), then the FWHM is given as $\Delta t (\equiv \tau) = 2\sigma_t\sqrt{\log 2}$, computed from solving the equation $I(t_{0.5})^2 = \frac{1}{2}I_0^2$ for $t_{0.5}$ and finding Δt as the difference between the roots $t_{\pm 0.5}$. Similarly, if we compute the FWHM of the frequency spectrum of $I(t)$, which is FT of $I(t)$, we arrive at [23]

$$\Delta t \Delta\omega \geq 2.773, \quad \text{or } \Delta t \Delta\nu \geq 0.441. \tag{3.6}$$

Relation 3.6 is called the time–bandwidth product relation for a Gaussian (temporal) light pulse, where Δt is the FWHM pulse duration and $\Delta\nu$ [Hz] is the FWHM linear bandwidth of the light pulse.

3.2.1 Transform-limited Pulse

Unless special care is taken, the time–bandwidth product $\Delta t \Delta\omega$ of a laser pulse is easily greater than the absolute minima. If this product is equal to the absolute minima, we call it a transform-limited pulse. In practice, a perfect transform-limited pulse cannot be easily produced, e.g. due to dispersion effects in a laser cavity, unless the dispersion is properly controlled. For a Gaussian pulse, we can write the duration of the transform-limited pulse given the available bandwidth as

$$\Delta t \sim 0.441 \frac{\lambda^2}{c\Delta\lambda}, \tag{3.7}$$

where c is the velocity of light, $\lambda \equiv \frac{c}{\nu}$ is the center wavelength and $\Delta\lambda$ is the pulse wavelength bandwidth. For HBESL's laser oscillator (OCTAVIUS-85M) with typical $\lambda \approx 800$ nm, $\Delta\lambda \sim 200$ nm, relation 3.7 yields a transform-limited pulse duration $\Delta t \approx 4.7$ fs. This corresponds to ~ 2 optical cycles of $\lambda = 800$ nm optical pulse.

3.3 Overview of HBESL's Laser System

The HBESL laser oscillator is based on a Titanium Sapphire ($TiAl_2O_3$) (Ti:Sapph) lasing medium. The Ti:Sapph medium has a peak absorption at $\lambda = 532$ nm and a broad emission spectrum from 600 nm to 1200 nm. Therefore Ti:Sapph systems can support a very large bandwidth necessary for the production of ultrashort pulses. The oscillator pulses are then amplified by a regenerative amplifier via chirped pulse amplification (CPA). Before the amplification stage, an acousto-optic programmable dispersive filter (AOPDF) is employed to manipulate the seed (oscillator) pulses for optimizing amplified pulse duration. The amplified pulses out of the amplifier are then sent through a set of nonlinear optics for frequency upconversion where the 800-nm pulses are converted to 266-nm pulses. Figure 3.3 shows the schematic of the laser system and the main specifications of its components. More details of the system components are described in the following sections. Table 3.1 summarizes the manufacturer and model names of the laser apparatus mentioned in Fig. 3.3.

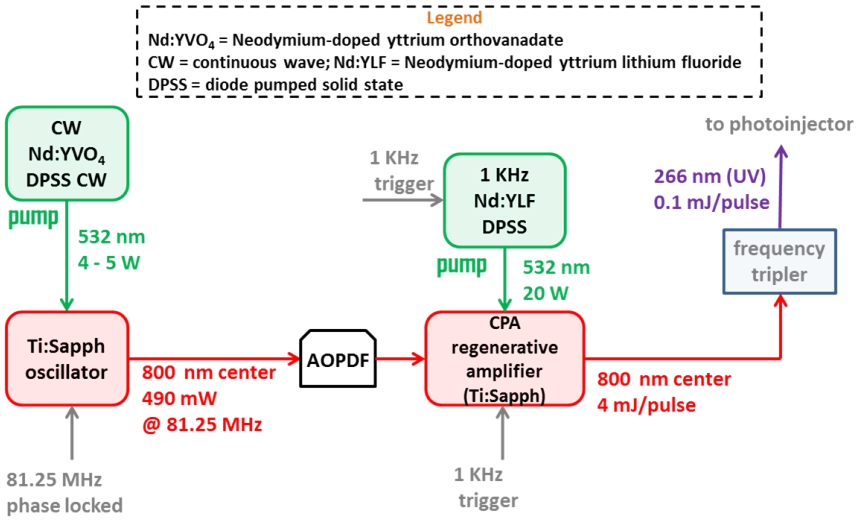

Figure 3.3: A schematic of the primary laser system at HBESL.

Table 3.1: HBESL laser lab primary apparatus model specifications.

System	Model	Maker
Nd:YVO_4 pump	Millennia Pro	Spectra-Physics
Ti:Sapph oscillator	Octavius-85M	idestaQE/Thorlabs
AOPDF	Dazzler	Fastlite
Nd:YLF pump	Empower	Spectra-Physics
CPA amplifier	Spitfire Pro	Spectra-Physics

3.4 The Octavius-85M Oscillator Laser

HBESL upgraded the seed laser to the Octavius-85M Ti:Sapph broadband oscillator laser early 2012 to pursue the generation of femtosecond ultrashort pulses. Currently Ti:Sapph is the best choice for the gain medium in ultrafast lasers because of the supported broad bandwidth [24] along with high thermal conductivity allowing for effective cooling. The Octavius is one of the fastest commercially available lasers in the market, originally developed at MIT. The laser features a bandwidth of up to > 300 nm and has generated pulses as short as 6 fs [25]. To maintain and

operate a laser of such a kind requires some understanding of the physics and the design of broadband lasers, hence this section.

Ultrashort pulses are generated in an oscillator laser and are typically amplified in an amplifier laser as required. A laser pulse travels back and forth in the oscillator's cavity, hence the name oscillator. There are certain conditions that have to be met for a stabilized pulsed output of an oscillator. The free-wave equations we obtain from Maxwell's equations by performing the operations $\boldsymbol{\nabla} \times (\boldsymbol{\nabla} \times \boldsymbol{E})$ and $\boldsymbol{\nabla} \times (\boldsymbol{\nabla} \times \boldsymbol{B})$ to decouple $\boldsymbol{E}$ and $\boldsymbol{B}$ are given as

$$\nabla^2 E = \mu_0 \epsilon_0 \frac{\partial^2 E}{\partial t^2} \ ; \ \nabla^2 B = \mu_0 \epsilon_0 \frac{\partial^2 B}{\partial t^2}. \tag{3.8}$$

The exact solution to Eqns. 3.8 depends on the initial and boundary conditions. Hence the light wave that can be sustained in a laser cavity depends on the cavity design. A laser cavity may support different transverse modes characterized by the transverse shape of the electromagnetic field. Each transverse mode can have different longitudinal modes differed in frequency (or wavelength) of the wave. The most common transverse mode in pulsed lasers is the fundamental TEM_{00} mode, which has a cylindrically symmetric Gaussian intensity distribution. We are primarily concerned about the longitudinal modes which differ only in frequency and play a critical role in generation of ultrashort pulses .

If we consider the picture presented in Fig. 3.2, we can see a pulsed output as a superposition of several continuous waves or longitudinal modes supported by the laser cavity. Imagine a continuous wave making a round trip inside the laser cavity being reflected off by the end mirrors. It is important that this wave constructively interferes with itself after the reflection so that the pulses that come out of the oscillator have stable intensity output, over time. Therefore the following standing

wave condition has to be achieved for each longitudinal mode characterized by its specific wavelength λ;

$$\frac{m\lambda}{2} = L, \qquad \text{with } m \in \mathbb{N} \tag{3.9}$$

where m is called the order of the longitudinal mode and L is the cavity length. Only those modes that satisfy Eq. 3.9 and fall in the emission profile of the gain medium—here Ti:Sapph—can sustain (see Fig. 3.4). Using $\nu = c/\lambda$, Eq. 3.9 can be written as $\nu_m = mc/2L$, where ν_m is the linear frequency of the mth (order) mode. Therefore for a given L, the frequency seperation $\delta\nu$ between any two adjacent modes is given as

$$\delta\nu = \nu_{m+1} - \nu_m = \frac{c}{2L}. \tag{3.10}$$

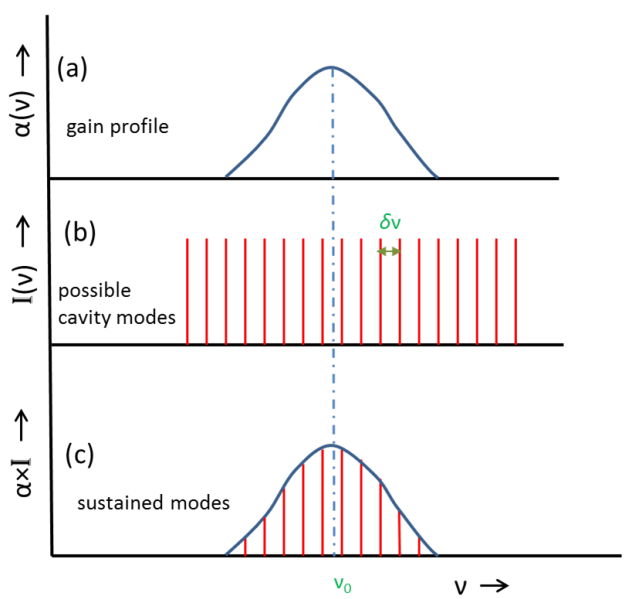

Figure 3.4: The gain coefficient profile α of the lasing medium (a), arbitrary intensity profile of the cavity modes (b), and the sustained longitudinal modes in the laser cavity (c).

Alternatively, the intermodal wavelength seperation $\delta\lambda$ is given as $\lambda^2/2L$. The repetition rate $\mathcal{R}$ of the laser—defined as the number of output pulses per second—depends on the time T taken by a pulse for one round trip (covers $2L$ distance) and is given as

$$\mathcal{R} = \frac{1}{T} = \frac{c}{2L}. \tag{3.11}$$

By comparing Eqns. 3.10 and 3.11 we can see that the repetition rate $\mathcal{R}$ and the frequency separation between any two adjacent modes $\delta\nu$ are the same. For a desired $\mathcal{R}$ of 81.25 MHz of the OCTAVIUS, the cavity length $L \approx 1.84$ m.

3.4.1 Self-phase Modulation (SPM)

In a Ti:Sapph oscillator, the natural lasing happens in a continuous mode with only a few longitudinal modes. For a pulsed operation, especially for an ultrashort pulsed operation, many modes have to be induced and sustained. Self-phase modulation (SPM), a nonlinear effect resulting from Kerr effect, generates the additional longitudinal modes required for the generation of ultrashort pulses. Kerr effect is the linear electric field intensity dependence of the refractive index inside a medium. The index is given by the following equation (for a cylindrically symmetric pulse);

$$n(I, r) = n_1 + n_2 I(r), \tag{3.12}$$

where r is the spatial coordinate, n is the net refractive index at a point r in the Kerr medium, I is the laser electric field intensity, n_1 is the linear refractive index and n_2 is the second order nonlinear (dependence on E as $I = E^2$) refractive index of the Kerr

medium which, in this case, is the Ti:Sapph lasing medium. The Kerr effect occurs in almost all materials but the strength of the effect varies among different materials. Kerr effect produces two relevant important nonlinear effects which together are responsible to generate ultrashort laser pulses; the first is leading to the generation of additional bandwidth in the cavity, and the second is self-focusing of the laser beam leading to mode locking (ML). The latter is discussed in the next section. SPM is the change in the phase of an intense pulse due to the temporal nonlinear refractive index introduced by the pulse itself. For an optical pulse whose Gaussian temporal intensity profile is given as

$$I(t) = I_0 e^{(-\frac{t^2}{\tau^2})}, \tag{3.13}$$

and as the pulse propagates through the medium, the refractive index varies with time and is given by the derivative of Eq. 3.12 as

$$\frac{dn}{dt} = n_2 \frac{dI}{dt} = \frac{-2t}{\tau^2} n_2 I_0 e^{(\frac{-t^2}{\tau^2})}. \tag{3.14}$$

The instantaneous phase $\phi(t)$ of the pulse is given by $\phi(t) = \omega_0 t - k_0 z = \omega_0 t - k_0 n(I) l$ where ω_0 is the carrier frequency, k_0 is the carrier wavenumber $(2\pi/\lambda_0)$ in vacuum and l is the distance the pulse has propagated in the medium. The instantaneous frequency $\omega(t)$ is given by

$$\omega(t) = \frac{d\phi(t)}{dt} = \omega_0 - k_0 l \frac{dn(I)}{dt} = \omega_0 + \frac{2lk_0 n_2 I_0}{\tau^2} t e^{(\frac{-t^2}{\tau^2})}. \tag{3.15}$$

From the time dependent part in $\omega(t)$ i.e $t \exp(-t^2/\tau^2)$ we can see the head of the pulse $(-\tau/2)$ is red-shifted while the tail $(+\tau/2)$ is blue-shifted increasing the overall bandwidth of the original pulse, creating some bandwidth outside of the Ti:Sapph

emission profile. The pulse width remains constant if dispersion is neglected, but in practice, the dispersion in the Kerr medium chirps the pulse. The typical spectrum of HBESL's OCTAVIUS-85M is shown if Fig. 3.5. A part of the spectrum is created by SPM.

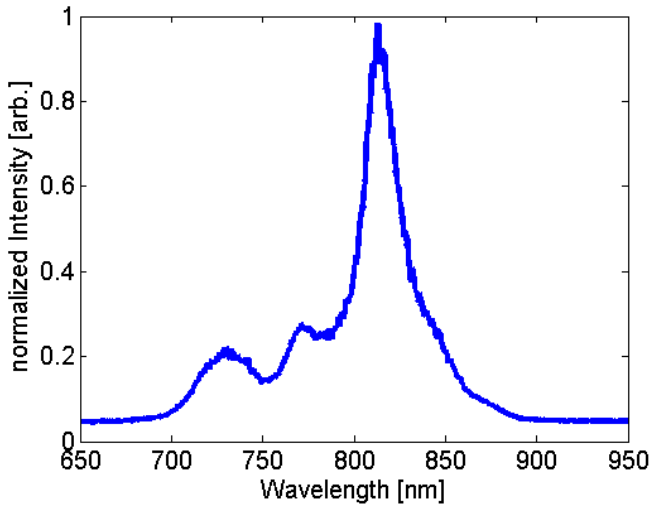

Figure 3.5: The typical spectrum of the OCTAVIUS-85M at HBESL.

3.4.2 Kerr Lens Mode Locking

The phase relation among all the modes inside the laser cavity defines the pulse width for a given bandwidth. In an ideal laser cavity, all the modes in the laser pulse travel at the speed of light with no dispersion and with a fixed phase relationship. In practice, dispersive optical elements like lenses, mirrors and the lasing medium introduce a wavelength dependent dispersion among the modes causing the optical pulse intensity to change with time, if not taken care of. A process called mode locking (ML) along with dispersion compensating elements forms well defined stable optical pulses. Mode locking refers to locking the relative phases among the

different 'competing' longitudinal modes. Kerr-lens mode locking (KLM), a passive ML technique, is used in ultrashort oscillators including the OCTAVIUS. In passive ML, unlike in active ML, there are no external modulators in the cavity employed to maintain the ML. KLM is another nonlinear effect resulting from Kerr effect as mentioned in the previous section.

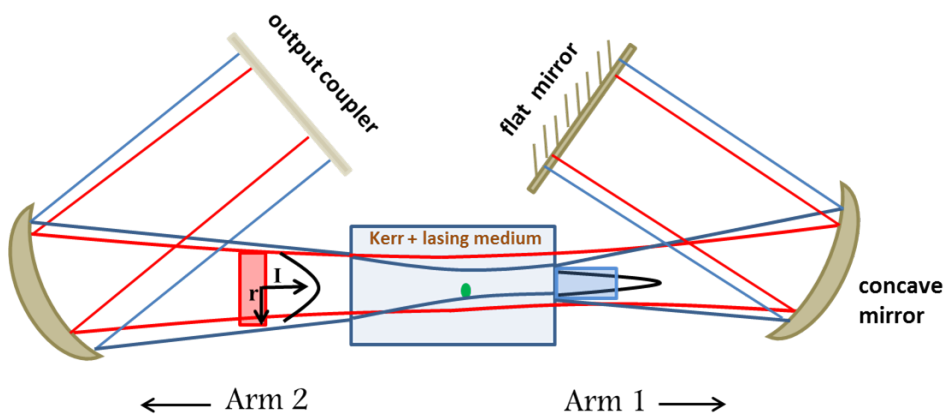

Figure 3.6: Kerr lens mode locking of a stable cavity with soft apperture (OCTAVIUS-85M).

The intensity profile of the fundamental transverse mode (TEM_{00}) assumes a Gaussian transverse distribution. The more intense core of the beam experiences higher refraction towards the center than the rest of the beam, which leads to self-focusing as the pulse passes through the Kerr medium (see Eq. 3.12). The reduction in the beam size is eventually limited by diffraction effects. The small spot size of the pump beam which is on the order of a few microns, helps the core of the beam obtain most gain. Once ML is started by a chosen mechanism, at the exit of the Kerr medium (steady state) the beam size is smaller in the center with a pulsed output and with higher peak intensity (blue beam) as shown in the Fig. 3.6. The minimal affected and the less intense continuous wave (CW) (red beam in Fig. 3.6) in the Kerr medium has lower divergence and gets reflected off of the cavity mirrors and

eventually gets damped out—this is an example of a soft aperture. Soft aperture works because the curvature of the concave mirrors are designed for the wavefront of the intense beam; so any other wavefront that significantly deviates from the design will not obtain the gain. The collective processes of maximal gain in the core of the beam and SPM (KLM processes) along with soft apperture and precise dispersion control (design processes) account for the sustainability of pulsed output (ML) for every round trip of the oscillating pulse in the cavity.

The passive ML can be initiated by a rapid physical movement, colloquially referred to as *kicking*, of a cavity mirror which creates a sudden fluctuation in the cavity intensity inducing a strong Kerr effect and a pulsed output.

Ultrashort lasers like the OCTAVIUS are less stable than picosecond lasers for several reasons which include smaller focus of the pump beam (high heat flux in the medium), high peak powers due to strong Kerr effect, existence of large number of modes to ML etc.

3.4.3 Operation of the Octavius-85M

The OCTAVIUS laser has a Ti:Sapph crystal longitudinally pumped by a frequency doubled CW 532-nm Nd:YVO_4 DPSS laser (SP MILLENIA PRO) (see Fig. 3.3). The pump laser propagates into the oscillator's cavity in the direction shown by the green arrow in Fig. 3.7, traverses through the pump lens (PL), and focuses inside the crystal. Here, either side of the laser crystal is referred to as an arm. Arms 1 and 2 together make up the laser cavity. Arm 1 has five chirped mirrors including a concave mirror and two pairs of flat dispersion compensation mirrors (DCM). Arm

2 has two chirped mirrors—a concave mirror and a flat mirror—and the output coupler (OC) as shown in Fig. 3.7.

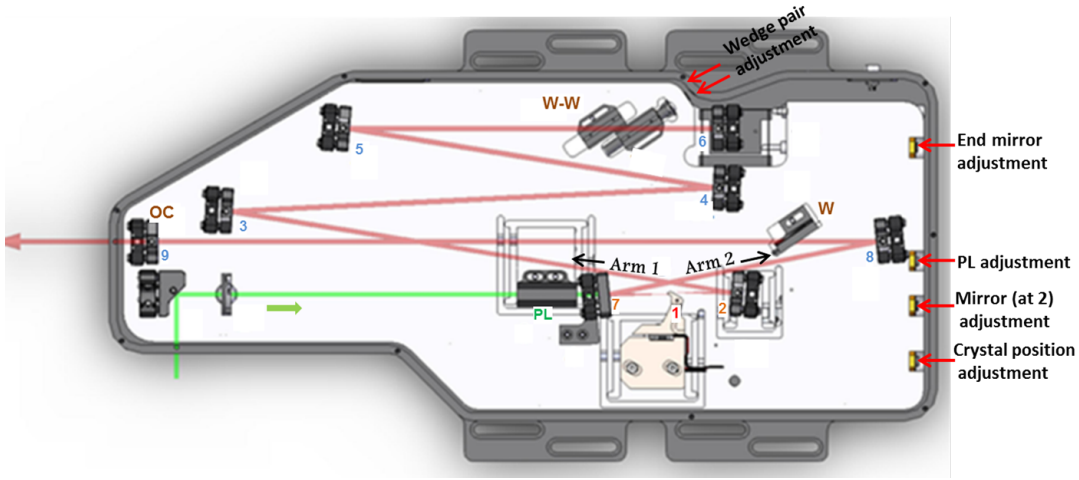

Figure 3.7: Layout of the OCTAVIUS-85M oscillator laser [26].

Initially, photons produced through stimulated emission propagate in both directions (along the two arms) but when the steady state condition is reached, only one pulse oscillates within the cavity. The crystal is cut for the Brewster's angle, so only the photons whose polarization has zero reflectance at the surface of the crystal obtain the gain (in the steady state) leading to a polarized output. Every time the pulse gets reflected by the output coupler, a partial reflector, a small fraction of the pulse is leaked outside of the cavity to form the output pulse. Hence, the power inside the cavity is much higher than the output power.

The pulse travels from points 1 to 6, retrieves back to 1 and travels to 7 to 9 and retrieves back to 1—for one round trip (see Fig. 3.7). This total path length corresponds to $2L$. For every pass through the crystal, the pulse acquires a gain. There is a window 'W' and an adjustable pair of wedges 'W-W' (see Fig. 3.7) for dispersion compensation, all made of Barium Fluoride (BaF_2). The wedge pair induces negative dispersion in the pulse by causing the *redder* wavelengths travel

Table 3.2: Typical operating parameters of HBESL's OCTAVIUS system.

Parameter	Value
Pump Power	4.2 W
Pump wavelength	532 nm
Oscillator power	470 mW (CW*), 490 mW (P†)
Oscillator wavelength	700 - 900 nm
Oscillator repetition rate $\mathcal{R}$	81.25 MHz
Avg. energy/pulse	$\approx$ 6.03 nJ
Pulse duration	$\sim$ 26 fs FWHM

*continuous wave.
†pulsed.

more distance inside the wedge material than the *bluer* wavelengths. The window induces a positive dispersion. The DCM mirror pairs have over 200 layers of coatings to precisely control the group velocity dispersion [26].

The positions of the concave mirror at point 2, the end mirror at point 6, the pump lens (PL), and the crystal and the wedge pair W-W can be adjusted by translating them by using the corresponding screw adjustments shown on the right side of Fig. 3.7. Typically, only the adjustment of the mirror at point 2 is adequate to achieve a stable ML configuration. The cavity length can be adjusted by translating the end mirror which is also used to induce KLM via *kicking*. Typical operating parameters of HBESL's OCTAVIUS laser are given in Table 3.2.

3.5 Regenerative Amplification

The energy per pulse of the laser pulses coming out of an oscillator laser can be too low for most applications like photoemission, frequency upconversion etc. Hence amplification of the oscillator pulses (seed pulses) is often required. The goal

here is to amplify the OCTAVIUS-85M's pulses from nJ level to mJ level for multiple applications. Amplification of femtosecond pulses is particularly challenging because of a few reasons; there is a limitation on the maximum peak power an amplifying medium can endure during amplification (due to damage threshold), also it is hard to closely preserve the pulse bandwidth and time duration of the seed pulses. Chirped pulse amplification (CPA) is one popular technique of dispersing or 'chirping' the input seed pulse prior to amplification in the gain medium [27]. The chirping is done by using dispersive devices like diffraction gratings or dispersive materials where the pulse is stretched by about 10000 times to ps range, hence reducing the peak power of the seed pulses. This is done by the stretcher optics. The pulse is then amplified in the regenerative amplifier cavity to increase the energy to mJ level, then finally the amplified pulse is sent to the compressor optics to re-compress and attain high peak powers. There is a trade-off between the repetition rate of the amplifier and the maximum amplified energy attainable by the seed pulse. Lower repetition rates of the amplifier can yield more energy per output pulse without altering the average output power of the amplifier. In our case, the seed pulses are selected at the rate of 1 KHz from a 81.25-MHz pulse train of the oscillator by a commercially available amplifier (SP SPITFIRE PRO). The 1-KHz seed pulses are amplified one at a time for a 1-KHz repetition rate of the amplified pulses.

The SPITFIRE PRO amplifier is diagrammed in Fig. 3.8. The stretcher optics consists of a diffraction grating which disperses the seed pulse by making the longer wavelengths travel longer distances than the shorter wavelengths, between mirrors in multiple reflections. The chirped (stretched) pulse is then collimated close to the original spot size using the grating itself and is sent to the regenerative amplifier cavity for amplification. After the amplified pulse exits the regenerative cavity, the pulse is re-compressed close to its original duration in the compressor optics—which

is similar to the stretcher optics except that the longer wavelengths travel shorter distances leading to the temporal compression of the pulse. A schematic of the stretcher and compressor optics is shown in the Fig. 3.9.

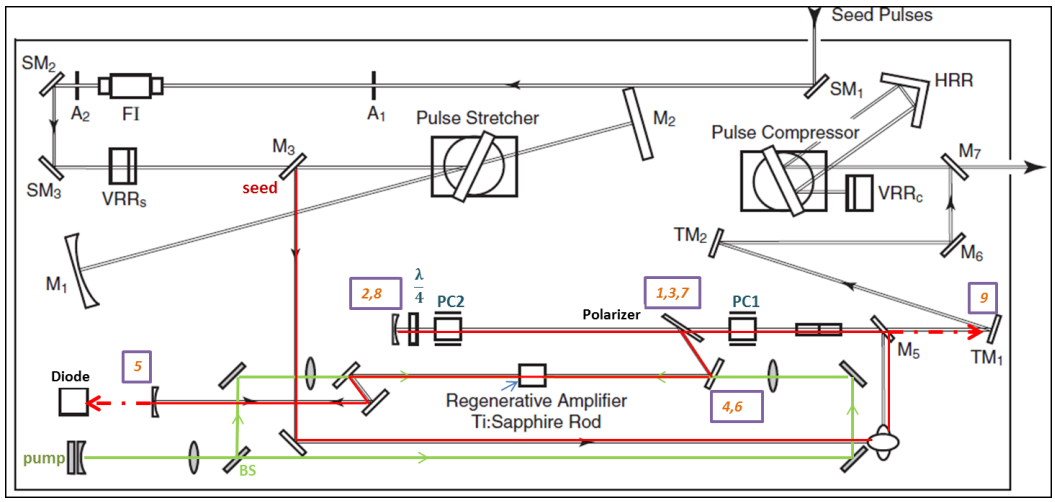

Figure 3.8: A diagram of the regenerative cavity of the Spitfire Pro regenerative amplifier [28]. The path of the pump laser is represented by the green lines. The red lines show the path of the seed pulse during amplification. The sequential path of the pulse during the last round trip is numbered 1-9.

In the regenerative amplification stage, the stretched pulse is sent through the regenerative cavity which has a Ti:Sapph rod (gain medium) pumped by a frequency doubled 532-nm Q-switched Nd:YLF pump laser (SP Empower) (see Fig. 3.3). The crystal pumping is done from both ends of the Ti:Sapph crystal by equally splitting the pump laser with a beam splitter (BS). The pulse is passed through the rod several times until maximum amplification is achieved. The three most important process of selecting, confining and releasing the seed pulses for amplification, one at a time, is done by using time-controlled Pockels cells (PCs). The PCs are electro-optic devices that when active act like a waveplate, rotating the polarization of the passing pulse by a certain amount. The Spitfire Pro amplifier's regenerative cavity is designed in such a way that only vertically polarized pulses are trapped in

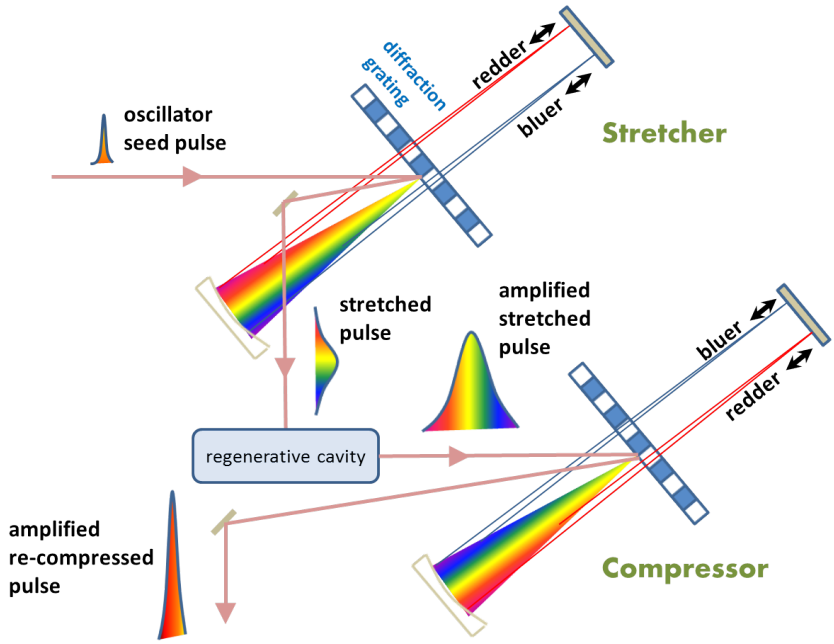

Figure 3.9: Schematic of chirped pulse amplification.

the cavity, or otherwise released. The amplification process using the PCs is done as follows (see Fig. 3.8);

1. The incoming vertically polarized chirped seed pulse arrives at PC1. PC1 is turned on and its timing set by a timing delay generator (TDG) selects one pulse from the 81.25-MHz pulse train of the incoming seed at the rate of 1 KHz. The polarization of the selected pulse which transmits through PC1 rotates to horizontal, then transmits through a polarizer and enters the regenerative cavity.

2. The horizontally polarized pulse arrives at PC2 which is turned off. The pulse passes through the quarter-wave plate (QWP) ($\lambda/4$) which rotates the polarization by 45^0. After being reflected from a concave mirror, the pulse passes through the QWP back, to have an additional rotation of polarization of 45^0. Hence the pulse is now vertically polarized and transmits through PC2

(turned off). Since the polarizer reflects only vertically polarized pulses, the pulse is now directed towards the Ti:Sapph rod for amplification.

3. The pulse gets amplified twice for each round trip—once for each pass through the Ti:Sapph rod (path 4-5-6 in Fig. 3.8). When the pulse arrives at PC2 for the second trip, PC2 is turned on to rotate the polarization of the passing pulse 45^0 for each pass. Hence the polarization of the pulse is rotated by 180° every time it traverses through the combination of PC2 and the QWP. Therefore the polarization of the pulse remains vertical. The pulse gets redirected to the Ti:Sapph rod for the second round trip amplification.

4. PC2 remains on for about 14 roundtrips, or until the pulse reaches its peak amplification. After the final roundtrip (when the maximum gain is reached) PC2 is turned off before the pulse passes through it, hence the passage of the pulse twice (back and forth) through the QWP now changes its polarization to horizontal. The pulse then transmits (exits) through the polarizer to outside of the cavity as the polarizer reflects only a vertically polarized pulse.

5. The output pulse is directed towards the compressor gratings for compression.

A photodiode behind the mirror at 5 connected to an oscilloscope collects some leaked power from the mirror for every round trip. The measurement of the pulse intensity (relative) on the oscilloscope shows the user the relative gain for every subsequent roundtrip of the pulse to determine the number of round trips required for maximum amplification. This helps the user set the timing specifications for the TDG. The pulse takes about 12 ns for each round trip, so the photodiode signals are separated by 12 ns for a given seed pulse. The normalized spectral intensity of the

pulse at various stages of amplification is shown in Fig. 3.10. The typical operating parameters of HBESL's Spitfire Pro amplifier are shown in Table 3.3.

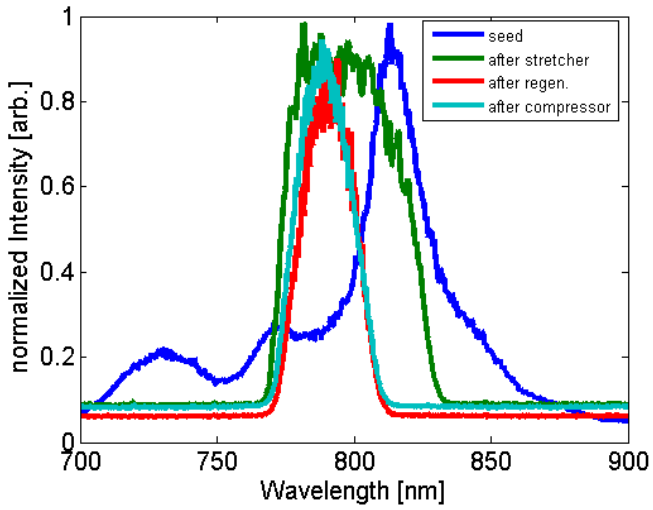

Figure 3.10: Spectral intensity of the original seed pulse at various stages of CPA. The seed spectrum refers to that of the Octavius-85M. The spectra are normalized to unity.

3.6 Laser Pulse Shaping

Shaping of ultrashort laser pulses has many applications in accelerator science, such as optimizing the pulse length, shaping of electron beams via photoemission [29], electron bunch diagnostics [30] and other applications that require custom-shaped laser pulses. The HBESL employs the Dazzler, a commercially available acousto-optic programmable dispersive filter (AOPDF), primarily to optimize or vary the amplified seed laser pulse duration. In an AOPDF, an incoming optical pulse along the ordinary axis is diffracted by a programmable collinear acoustic signal inside a birefringent crystal. The diffracted optical pulse, diffracted into the extraordinary axis, is the desired shaped output signal (see Fig. 3.11). The acoustic

Table 3.3: Typical operating parameters of HBESL's SPITFIRE PRO amplifier.

Parameter	Value
Pump power	18 - 20 W
Pump wavelength	532 nm
Amplifier repetition rate $\mathcal{R}$	1 KHz max.
Amplification factor	$\sim 7.0 \times 10^5$
Amplified energy/pulse	$\simeq$ 4 mJ
Bandwidth output	30 nm max. (800 nm center)
Bandwidth input	50 nm max. (800 nm center)
Pulse duration	$\sim$ 100 fs FWHM

signal is produced using a piezoelectric transducer attached to one end of the crystal. The shape of the output optical signal is defined by the shape of the acoustic spatial signal which is produced by a user-programmed transducer temporal signal.

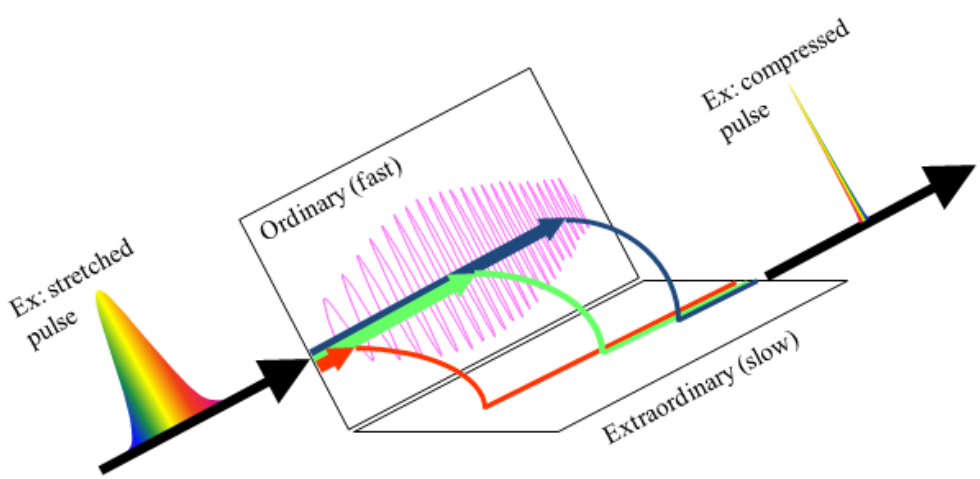

Figure 3.11: The principle of AOPDF, adopted from [31, 32].

When the input optical signal of (angular) frequency ω_{in} travels collinear to the acoustic signal of frequency Ω, the acousto-optic diffraction is efficient only at the phase-matching condition given by [33]

$$\frac{\omega_{out} n_{out}}{c} = \frac{\omega_{in} n_{in}}{c} + \frac{\Omega}{V}, \tag{3.16}$$

where ω_{out} is the frequency of the diffracted output pulse, c is the speed of light, V is the acoustic speed in the crystal, n_{in} and n_{out} are the indices of refraction along the ordinary and extraordinary axes respectively. Under the approximation $\omega_{out} \approx \omega_{in}$, Eq. 3.16 reduces to [33]

$$\omega_{in} \approx \frac{\Omega}{\alpha} \tag{3.17}$$

where

$$\alpha = (n_{out} - n_{in})\frac{V}{c}. \tag{3.18}$$

If $E_{in}(t)$ is the temporal input electrical signal, $S(t/\alpha)$ is the transducer temporal signal and $E_{out}(t)$ is the diffracted (output) optical signal, then it has been shown that E_{out} is proportional to the convolution of E_{in} and S as [31]

$$\begin{aligned} E_{out}(t) &= E_{in}(t) \otimes S\Big(\frac{t}{\alpha}\Big) \\ &= \int_{-\infty}^{\infty} E_{in}(t') S\Big(\frac{t-t'}{\alpha}\Big) dt', \end{aligned} \tag{3.19}$$

or in the frequency domain we have

$$E_{out}(\omega) = E_{in}(\omega) S(\alpha\omega). \tag{3.20}$$

When an ultrashort pulse travels through the birefringent crystal, each frequency ω gets diffracted efficiently at a particular longitudinal position $z(\omega)$ where the phase matching happens according to Eq. 3.16. $z(\omega)$ is profiled by the programmed $S(t/\alpha)$. Hence in the schematic shown in Fig. 3.11, the *bluer* wavelengths are diffracted later than the *redder* wavelengths for the given acoustic spatial profile (pink). For $n_{out} > n_{in}$, this introduces a phase delay to the *redder* wavelengths with respect to the *bluer*. Thus the relative spectral phase delay of the output pulse can be controlled by $S(\alpha\omega)$. Profiling of $S(t/\alpha)$ is done using numerical methods.

The Dazzler's integrated software allows the user to change the relative optical spectral phase of the output pulse by allowing for the user input optical delay coefficients. When the complex amplitude of a spectral wave is defined as $A(\omega)e^{i\phi(\omega)}$, then $\phi(\omega)$ can be written as [34]

$$\phi(\omega) = -\sum_{l=1}^{N} a_l(\omega - \omega_0)^l \tag{3.21}$$

where a_l is the lth order coefficient. The Dazzler's software allows the user to change the coefficients upto a_4. At HBESL, these coefficients are changed to adjust the spectral phase of the seed pulse going into the Spitfire amplifier for optimum compression of the amplified pulse. It can be noted that the compressor optics are optimized for a certain spectral phase of the input seed pulse. To maintain optimum compression (short duration) of the amplified pulse, it is easier to adjust the coefficients a than to tune the compressor optics. The second order coefficient a_2 has the most effect on the pulse duration, hence can usually be used alone to optimize the pulse duration as shown in Fig. 3.12.

Laser pulse shaping is possible by adjusting the spectral amplitude as mentioned earlier. Keeping the seed spectrum smooth and symmetric about the center wave-

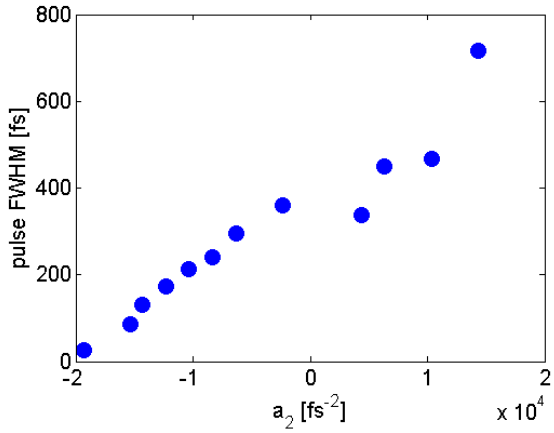

Figure 3.12: FWHM of the pulse measured using FROG (see Section 3.8) for various a_2 values in the DAZZLER's software.

length (here 800 nm) is important for proper amplification of the seed pulses in the regenerative cavity. The DAZZLER's software also allows the user to lower the spectral amplitude in a chosen spectral window of interest by any amount, hence allowing for pulse shaping. Figure 3.13 shows how a spectrally asymmetric seed pulse (blue trace) is shaped more symmetric (green trace) by reducing the spectral amplitude for wavelengths greater than 800 nm accordingly. The symmetrically shaped seed pulse is sent into the amplifier.

3.7 Frequency Upconversion

Higher laser frequencies are routinely generated from an original source laser in labs using the process of frequency upconversion like second harmonic generation (SHG). Such frequency upconversion processes employ nonlinear materials to generate different harmonic frequencies from the original source frequency, which serve as economical ways, and in some cases as essential ways to generate certain laser frequencies. In 1961, Franken et. al were the first to detect the generation of blue light

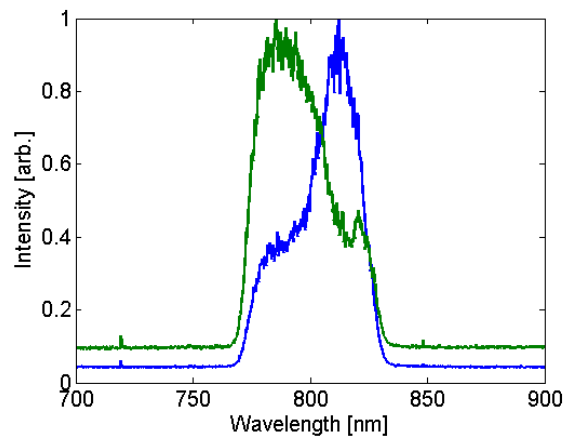

Figure 3.13: Pulse spectral shaping using the DAZZLER. The blue curve is the original seed pulse spectrum, while the green is the shaped spectrum out of the DAZZLER.

(347 nm) from a ruby laser beam (694 nm) via SHG after the beam was propagated through a quartz crystal [35]. The principle behind the harmonic generation is that nonlinear response of a material to the high intensity electric field of a source laser beam can generate higher harmonics. Recently, high harmonic generation (HHG) in gases like H, Ne and Kr has led to the generation of soft x-rays [36]. If we consider a laser pulse of (angular) frequency ω whose real electric field magnitude is $E(\omega)$ propagating in a nonlinear crystal of dielectric polarization P, the polarization response of the material is given as

$$P = \epsilon_0 \chi^{(1)} E(\omega) + \epsilon_0 \chi^{(2)} E(\omega)^2 + ... \tag{3.22}$$

where $\chi^{(n)}$ is the dielectric susceptibility of order n. χ is typically a tensor, but for simplicity, here we have considered it as a scaler by assuming that the nonlinear material is isotropic. By substituting $E(\omega) = A\cos(\omega t)$ in Eq. 3.22, where A is the field amplitude, we get

$$P = \frac{1}{2}\epsilon_0\chi^{(2)}A^2 + \epsilon_0\chi^{(1)}A\cos(\omega t) + \frac{1}{2}\epsilon_0\chi^{(2)}A^2\cos(2\omega t). \tag{3.23}$$

The appearance of the cosine term with the frequency 2ω in Eq. 3.23 is the source of the SHG. Similarly 3ω and higher frequencies can be generated under stronger electric field intensities and higher order χ terms in appropriate nonlinear media; but such a method gets very inefficient as $\chi^{(n)}$ quickly decreases with n. A more efficient process called sum frequency generation (SFG) can be used to generate the frequency 3ω from ω using $\chi^{(2)}$. If we consider a laser beam which has two frequency components ω_1 and ω_2 (where $\omega_1 > \omega_2$) given as $E = A_1\cos(\omega_1 t) + A_2\cos(\omega_2 t)$, where A_1 and A_2 are the amplitudes of the components, then Eq. 3.22 gives a polarization term

$$P_{\omega_1 \pm \omega_2} = \frac{1}{2}\epsilon_0\chi^{(2)}A_1A_2\cos(\omega_1 \pm \omega_2)t, \tag{3.24}$$

which acts as the source for the frequency $\omega_1 + \omega_2$ (SFG) or $\omega_1 - \omega_2$ (difference frequency generation (DFG)). The choice of SFG or DFG can be set by a phase-matching condition imposed by the crystal medium that is efficient for only one of these processes. The phase-matching is an experimental optimization condition that is typically set by utilizing a crystal medium of a specific birefringence, tailored to maximize the output of a converted frequency. For $\omega_1 = 2\omega$ and $\omega_2 = \omega$, we have $\omega_1 + \omega_2 = 3\omega$, a tripled frequency generated via SFG. It can be noted that SHG is a special case of SFG where $\omega_1 = \omega_2 = \omega$.

So far, we have considered E and P as scalars, but a vector picture of these variables reveals that the generated upconverted frequency component (electric field) is orthogonal to the source component. Hence it is important that the source components have the same polarization for optimum SFG output. Since χ is a tensor in

a typical real case, orientation adjustment of the nonlinear crystal (for maximum χ) with respect to the incoming source laser beam is necessary for optimization of frequency upconversion.

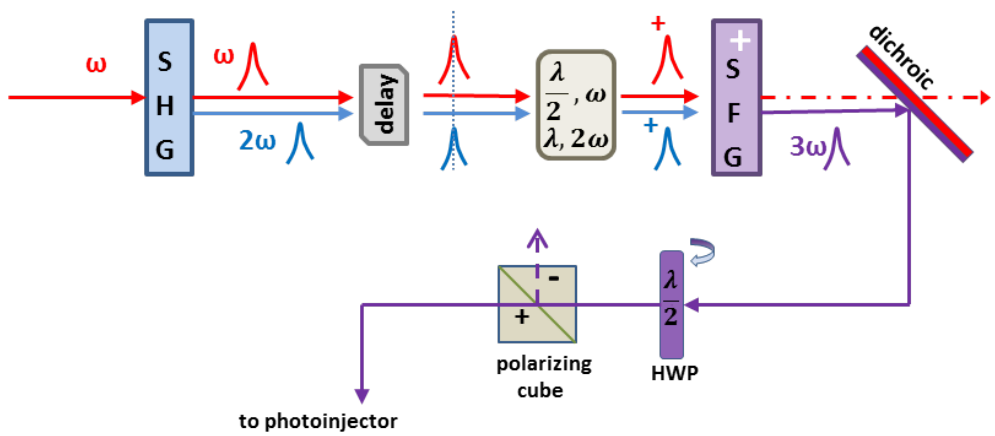

Figure 3.14: Production of ultra-violet (UV) pulses at HBESL through frequency tripling.

At HBESL, ultra-violet (UV) laser pulses of wavelength 266 nm are generated from high intensity infrared (IR) pulses of 800 nm center wavelength through SHG followed by SFG as shown in Fig. 3.14. Effectively, the UV pulses are produced as a third harmonic of the IR pulses, hence the optics that are used to upconvert the IR frequency ω to the UV frequency 3ω are referred to as the tripler optics. An IR pulse of 800 nm (ω) center wavelength first goes through an SHG crystal resulting in partial conversion of the pulse into a 400 nm (2ω) blue pulse. The delay between the left over IR pulse and the blue pulse can be adjusted by a delay optic (a piece of calcite), and then the two pulses are superimposed inside an SFG crystal that combines the frequencies ω and 2ω into the frequency 3ω, resulting in the 266-nm UV output pulse. Prior to the SFG stage, the ω and 2ω components go through a half-wave plate (HWP) for the IR laser which is a full-wave plate (FWP) for the blue laser which makes their polarizations parallel to each other.

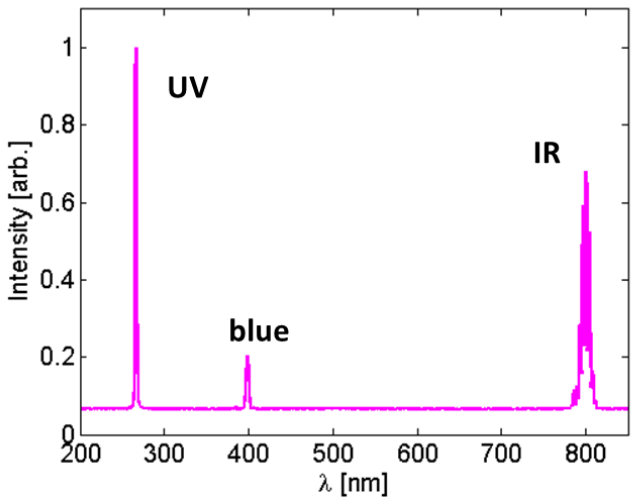

Figure 3.15: A typical spectral intensity of the output pulse from HBESL's tripler optics after frequency upconversion of 800 nm (IR) laser pulse into 266 nm (UV).

Any presence of the IR after frequency tripling is minimized by using a dichroic mirror that reflects the UV and transmits the IR. The intensity of the UV pulse directed towards the photoinjector can be controlled by a pair of a UV HWP and a polarizer (see 'Varying the laser energy' in Section 5.3), where the HWP can be remotely rotated. Typically, the efficiency of converting an IR pulse into UV is about 2.5 % at HBESL. The efficiency can be improved by increasing the peak power of the IR pulse—normally by shortening the pulse duration—as the processes of SHG and SFG nonlinearly depend on the pulse's peak electric field. A typical spectrum of the pulse exiting the polarizing cube measured with a spectrometer is shown in Fig. 3.15.

3.8 Temporal Laser Diagnostics

To measure an event in time, a shorter or equal event is necessary. Laser pulses as short as a few femtoseconds are often produced in labs. Autocorrelation techniques were developed for pulse duration measurement where the pulse to be measured is split and overlapped with itself inside a nonlinear medium to get an intensity autocorrelation function. The duration of the pulse can be approximately estimated from this function. However, the phase information of the pulse cannot be measured using conventional autocorrelation methods. Hence advanced autocorrelation methods like frequency resolved optical gating (FROG) have been developed to fully characterize ultrashort laser pulses [37]. The FROG method is one of the most commonly used measurement technique to characterize ultrashort pulses.

In the general procedure of FROG methods, the pulse to be measured is split into two equally intense pulses and then the pulses are overlapped inside a nonlinear medium. The amount of overlap is adjusted by precisely controlling the path length of one of these pulses using a delay stage. The nonlinear medium produces a 'gated' signal, only when the two pulses overlap (in time and space). This gated signal is spectrally resolved using a spectrometer. The spectrum data is collected for various user-set delay settings and the resulting 2D spectrogram is referred to as FROG sonogram.

HBESL utilizes SHG FROG, a widely used FROG technique due to its simplicity and ease of use. A schematic of an SHG FROG setup is shown in Fig. 3.16. If $E(t)$ is the electric field magnitude (in time t) of one of the pulses and $E(t - \delta t)$ is the field of the delayed pulse delayed by δt, then the gated signal E_{gat} generated from a

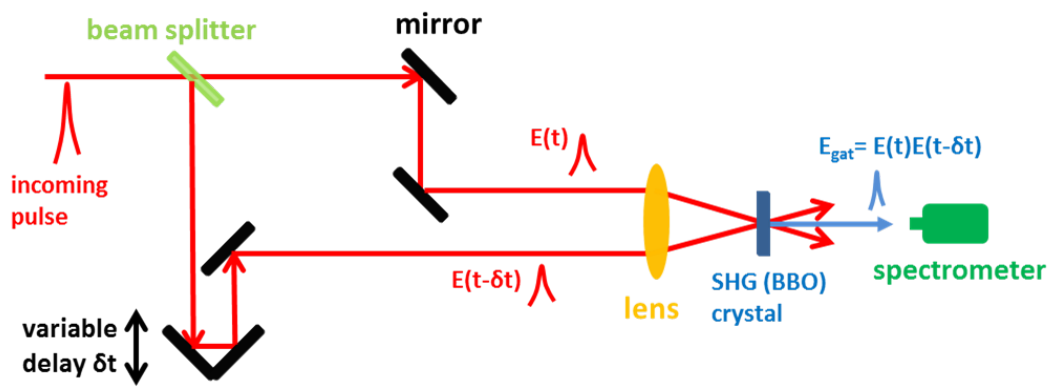

Figure 3.16: A schematic of an SHG FROG setup.

SHG medium [here a Barium Borate (BBO) crystal] due to the overlap of the two pulses is given as

$$E_{gat} = E(t)E(t - \delta t). \tag{3.25}$$

In our case, E_{gat} has a wavelength $\lambda = 400$ nm (SHG) while $E(t)$ and $E(t-\delta t)$ have $\lambda = 800$ nm. The FROG sonogram of the gated signal is mathematically represented by the gated pulse intensity $I(\omega, \delta t)$ as follows, where ω is the angular frequency;

$$I(\omega, \delta t) = \Big|E_{gat}(\omega, \delta t)\Big|^2 = \Big|\mathcal{F}[E_{gat}(t, \delta t)]\Big|^2 = \Big|\int_{-\infty}^{+\infty} E(t)E(t - \delta t)e^{-i\omega t}dt\Big|^2. \tag{3.26}$$

An estimation of the pulse width can be obtained from the autocorrelation of the two pulses, and such a way of determining the pulse width would be equivalent to the conventional methods used prior to FROG. In FROG, due to the spectral resolution of the autocorrelation function, the determination of the pulse electric field and the phase can be done using a phase-retrieval algorithm that utilizes the iterative method of generalized projections (GP). Once the gated signal through the

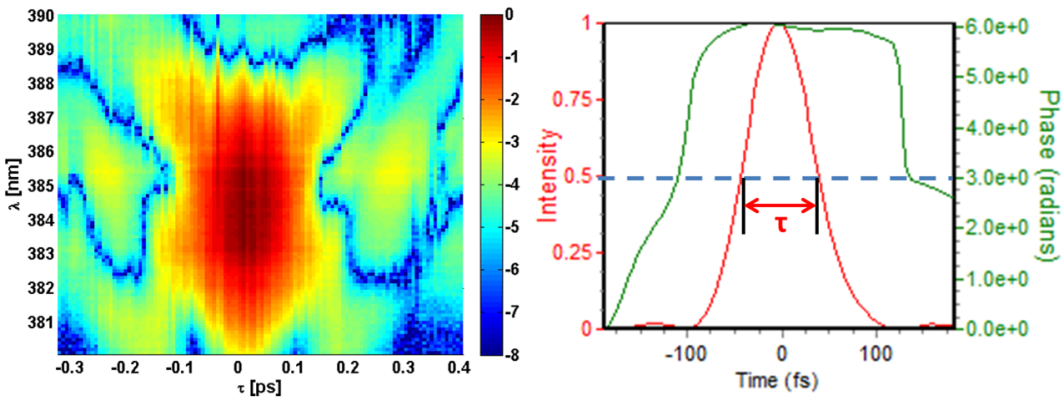

Figure 3.17: The FROG sonogram (left) and the corresponding pulse field intensity and phase retrieved using a GP algorithm (right), of an amplified pulse from HBESL's Spitfire Pro amplifier.

nonlinear medium, i.e. in this case Eq. 3.25, is known, the GP algorithm iterates to find the unique solution that satisfies the equation constraints 3.25 and 3.26 simultaneously [38, 39]. The GP algorithm, since being iterative, has to converge to obtain an accurate retrieval of the pulse field and the phase from the corresponding FROG sonogram. However, the solution may not converge if the sonogram has significant noise or is asymmetric due to poor FROG alignment—or jitter. Figure 3.17 shows the FROG sonogram (left) obtained from an SHG FROG method and the corresponding pulse field intensity and the phase (right) retrieved by a commercial GP algorithm, of an amplified pulse from HBESL's Spitfire Pro amplifier. The FWHM of the pulse is estimated to be $\tau \simeq 75$ fs.

CHAPTER 4

LASER SYNCHRONIZATION WITH THE RF GUN

Radio frequency (RF) guns are popular devices used to produce and rapidly accelerate electrons to relativistic energies. At HBESL, the klystron powers the RF gun at a rate of 0.5 Hz. The RF pulse duration is adjustable from 0 - 60 μs and the electric field amplitude from 0 - 40 MV/m. As mentioned in Chapter 2, in the case of photoemission, a laser pulse hits the photocathode located on the back plane of the RF gun and the emitted electrons are accelerated by the RF electric field. The maximum energy of the electron beam is achieved when the laser hits the photocathode in the right phase of the RF. Hence synchronization of the laser pulse with the RF pulse is essential for photo-emitted beams. More importantly, a jitter in phase between the laser and the RF pulses, from shot-to-shot, will translate into a jitter in the energy and the time of arrival of the bunch at a point farther from the gun. This is because beams accelerated by the RF pulse at slightly different phases will gain different energies, hence can get differently focused and steered by various photoinjector elements. Figure 4.1 shows a numerical simulation of how the laser–RF relative injection phase affects the mean beam energy and the bunch charge at a point 3 m from the cathode, where the initial beam charge emitted at the cathode is taken to be 1 nC. One of the disadvantages of employing photoemission in photoinjectors is the requirement for the laser to be at tight synchronization with the RF.

A diagram of the RF–laser pulse timing with the typical parameters of HBESL is shown in Fig. 4.2. The time lapse between any two successive klystron shots is

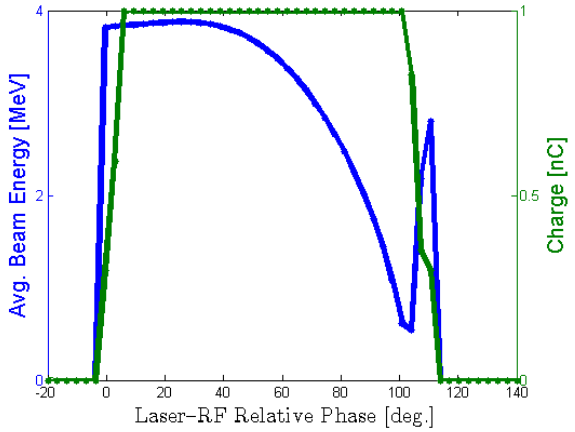

Figure 4.1: Dependence of mean beam energy and the bunch charge output, on the injection phase of the laser.

2 s (0.5 Hz). The 1.3-GHz RF standing wave completes the corresponding 1300 cycles per μs of the RF macro-pulse. The RF macro-pulse envelope takes the shape as shown in Fig. 4.2. The laser is fired on the photocathode at the rate of 0.5 Hz, once for every RF macro-pulse, but within one of the 1.3-GHz RF wave cycles. The relative phase between the laser and the 1.3-GHz RF wave can be adjusted to make sure the laser emits charge from the photocathode while operated at the desired phase.

The synchronization of the laser with the RF at A0 photoinjector is extensively described by T. Maxwell et. al in [40]. To summarize, the synchronization of the Ti:Sapph laser pulses with the photoinjector RF is done at two levels; the ns-scale and the fs-scale synchronizations. The Spitfire amplifier selects the 81.25-MHz pulses from the oscillator laser at the rate of 1 KHz. A 1-KHz trigger which has to be supplied to the amplifier for this purpose is derived from the 1.3-GHz master oscillator clock that also supplies the 0.5-Hz RF signal for the klystron macro-pulse; this corresponds to the ns-scale synchronization between the 1-KHz amplifier output pulse train and the 0.5-Hz RF macro-pulse. The fs-scale synchronization corresponds

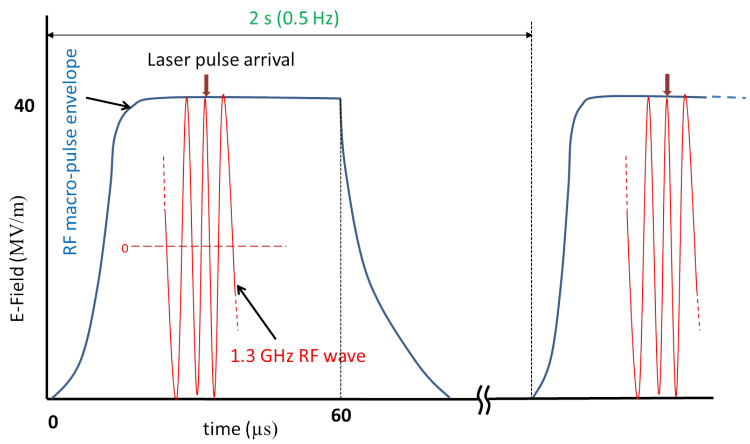

Figure 4.2: A diagram of the RF–laser timing with typical HBESL operating parameters. Note: items not scaled.

to the synchronization between the 81.25-MHz oscillator laser pulses to the 1.3-GHz RF standing wave. This is done by phase-locking the 81.25-MHz oscillator pulse train with that of a 81.25-MHz signal derived from the 1.3-GHz master oscillator signal that drives the 1.3-GHz RF wave in the gun.

Here we describe the upgrades performed to the laser and the locking of the repetition rate of the laser, which is a part of the fs-scale synchronization.

4.1 81.25-MHz Phase Locking

HBESL utilizes the previously existing coarse synchronization (ns-scale) between the Dazzler (see Section 3.6), the Spitfire amplifier, and the RF gun. Since the Tsunami oscillator, which had its integrated frequency locking system, was replaced with the Octavius-85M oscillator, new electronics were installed to lock the repetition rate of the Octavius. The locking of the repetition rate of a laser involves precisely stabilizing the cavity length (see Eq. 3.11), which otherwise changes due to the cavity temperature fluctuations. The Octavius has one of its end mirrors at-

tached to a piezoelectric actuator. The piezo-actuator thus changes the cavity length based on the voltage applied to it by a contol system. Figure 4.3 is the schematic of the repetition rate locking electronics which consists of a servo-controller, frequency mixer, piezo-controller and a bandpass filter (BPF).

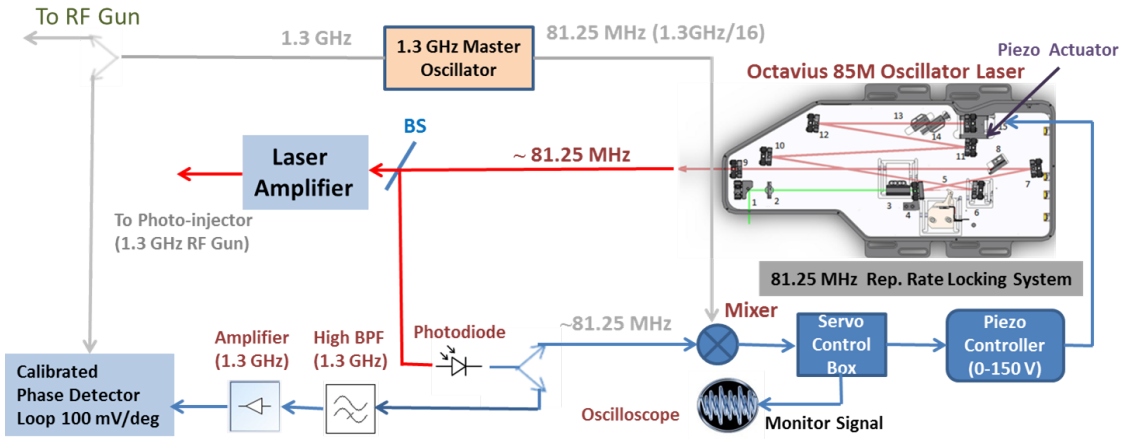

Figure 4.3: Schematic of the 81.25-MHz repetition rate locking loop. BPF stands for band-pass filter.

As shown in the Fig. 4.3, a fraction ($\sim 5\%$) of the oscillator's laser is sent to a photodiode which detects each pulse produced by the oscillator laser (see Fig. 4.4, left). HBESL's OCTAVIUS is tuned to produce a pulse train with a 81.25-MHz repetition rate, corresponding to the $1/16^{\text{th}}$ harmonic of 1.3 GHz. The photodiode signal is mixed with a (81.25-MHz) reference signal that is derived from the same master oscillator that triggers the klystron, by the frequency mixer. The frequency mixer multiplies the two input signals and outputs a voltage signal V_{out} as

$$\begin{aligned} V_{out} &= A_1 \cos(f_1 t + \phi_1) \times A_2 \cos(f_2 t + \phi_2) \\ &= \frac{A_1 A_2}{2}[\cos[(f_1 - f_2)t + \phi_-] + \cos[f_1 + f_2)t + \phi_+], \end{aligned} \tag{4.1}$$

where $A_1 \cos(f_1 t + \phi_1)$ represents the photodiode's signal with frequency f_1 and initial phase of ϕ_1, $A_2 \cos(f_2 t + \phi_2)$ represents the reference signal derived from the master oscillator, with frequency f_2 and an initial phase of ϕ_2, and $\phi_{\mp} \equiv \phi_1 \mp \phi_2$. Both f_1 and f_2 are close to 81.25 MHz but not equal when the repetition rate is not locked. A locked repetition rate with respect to the reference signal within a 1-ps jitter would mean $|f_1^{-1} - f_2^{-1}| < 1$ ps. The mixed signal is then sent to the proportional–integral (PI) servo-controller (New Focus LB1005) with a low-pass filter (filters out the term with $(f_1 - f_2)$) [41], which then tries to minimize the lower frequency signal by making $f_1 - f_2$ zero; this refers to phase locking of f_1 and f_2. The servo-controller continuously tries to achieve this locking, i.e making $f_1 - f_2$ zero, by sending the appropriate voltage $u(t)$ to the piezo-actuator via the piezo-controller to tune the cavity length in such a way that f_1 matches with f_2 in real time. If we define the voltage corresponding to the error signal as $e(t) \propto (f_1 - f_2)$ then the PI process is mathematically described as [42]

$$u(t) = [K_p e(t) + u_0] + K_i \int_0^t e(\tau) d\tau \tag{4.2}$$

where K_p (proportional gain), K_i (integral gain) and u_0 (voltage offset) are the servo-controller user settings, and τ is the time step of the integration. The proportional term $[K_p e(t) + u_0]$ and the integral term $K_i \int_0^t e(\tau) d\tau$ in Eq. 4.2 can be interpreted as the error correction terms in the *current* time and for *past* error respectively.

In order to measure the actual jitter between the 1.3-GHz RF and the laser in real time, we use a previously installed calibrated phase detector. The phase detector is a frequency mixer which takes the 1.3-GHz trigger signal from the RF and the 1.3-GHz signal from the laser (photodiode) as the input, then outputs a DC signal calibrated to 100 mV/deg jitter between the input signals. A 1.3-GHz

signal is obtained from the photodiode's 81.25-MHz signal by using a 1.3-GHz high BPF and an amplifier as shown in Fig. 4.3. The BPF (model MFC MN10) was commercially manufactured to meet the specifications of 1.3-GHz center frequency transparency with a maximum band width of 6 MHz FWHM [43]. It can be noted that the photodiode's frequency spectrum mostly consists of 81.25 MHz signal, but also some amount of higher harmonics due to the short temporal nature of the laser pulse. Figure 4.4 demonstrates this by showing an example 81.25-MHz diode signal train created numerically and the corresponding fast Fourier transform (FFT). It can be seen that the FFT of the diode signal consists of several higher harmonics of 81.25 MHz with a decreasing trend in strength with n of the nth harmonic. Hence, an amplifier is used to increase the strength of an nth harmonic frequency after that harmonic is extracted using a high BPF ($> n$) .

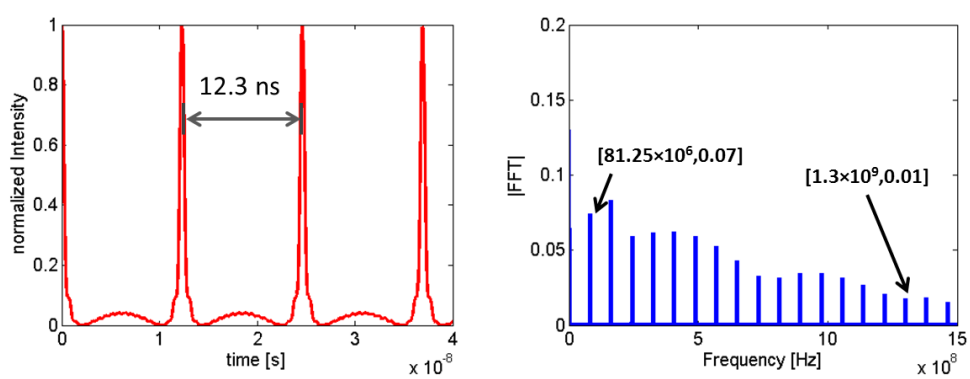

Figure 4.4: A numerically created example 81.25-MHz pulse train signal of the diode (left) and the corresponding FFT (right). The original 81.25-MHz frequency and the 16th harmonic of the original frequency, i.e 1.3-GHz are shown.

The phase detector measures the actual phase jitter between the RF wave inside the gun and the laser. A degree of phase jitter between two 1.3-GHz signals corresponds to 2.13 ps jitter in time. For the repetition rate locking loop using the two 81.25-MHz signals setup described above (Fig. 4.3), a peak-to-peak jitter

of about 5 degree has been measured by the phase detector. Such a 5 degree jitter cannot produce a stable beam; a peak-to-peak jitter of less than 1 degree is necessary. Hence, the 81.25-MHz repetition rate (phase) locking loop was upgraded to 1.3-GHz repetition rate locking system described in the following section.

4.2 1.3-GHz Phase Locking

The 81.25-MHz repetition rate locking setup shown in Fig. 4.3 was upgraded to the 1.3-GHz repetition rate locking system as shown in Fig. 4.5. In the upgrade, instead of locking the phase of two 81.25 MHz signals, two higher frequency signals (1.3 GHz) are phase-locked for stable repetition rate.

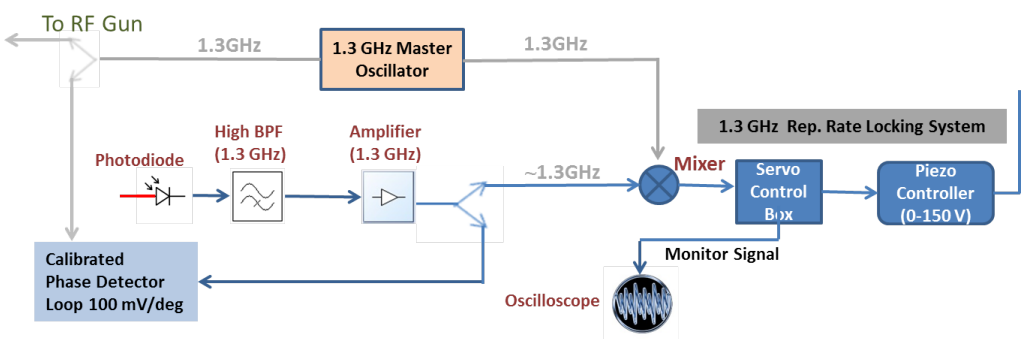

Figure 4.5: Schematic of the 1.3-GHz repetition rate locking loop. Compare with Fig. 4.3.

The jitter in time when two 1.3-GHz signals are phase locked, say within a degree, is 16 times lower (in jitter in time) than when the same phase-locking is done for the two 81.25-MHz signals. As a result, the jitter in time is reduced greatly. As shown in Fig. 4.5, the mixer is fed a 1.3-GHz signal from the master oscillator and a 1.3-GHz signal from the photodiode. As mentioned before, the photodiode signal's frequency spectrum contains a 1.3-GHz component. Thus the 1.3-GHz harmonic

($n = 16$) can be extracted from the photodiode's signal by using a BPF and then amplified as needed. The servo-controller works the same way as in the case of the 81.25-MHz locking loop, but the controller settings are to be adjusted for proper locking. The jitter measurements from the phase detector, of the 81.25-MHz and the 1.3-GHz repetition rate locking loops are compared in Fig. 4.6.

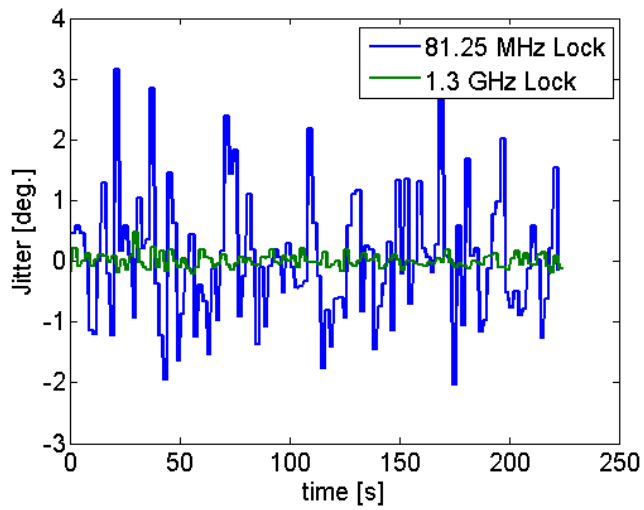

Figure 4.6: Comparison of the jitter from the 81.25-MHz and 1.3-GHz repetition rate locking loops as measured by the calibrated phase-detector.

It can be noted that a peak-to-peak phase jitter of about 5 degree (10.7 ps) in the case of the 81.25-MHz repetition rate locking loop is reduced to about 0.8 degree (1.7 ps) of jitter by upgrading to the 1.3-GHz locking loop. With the peak-to-peak phase jitter under a degree, the beam has been verified to be stable over time.

A histogram (see Fig. 4.7) of the data presented in Fig. 4.6 confirms the reduction of jitter as more events are concentrated around zero jitter in the case of the 1.3-GHz repetition rate locking loop indicating that the beam stability has been achieved for most shots. The achieved rms jitter was ≈ 200 fs.

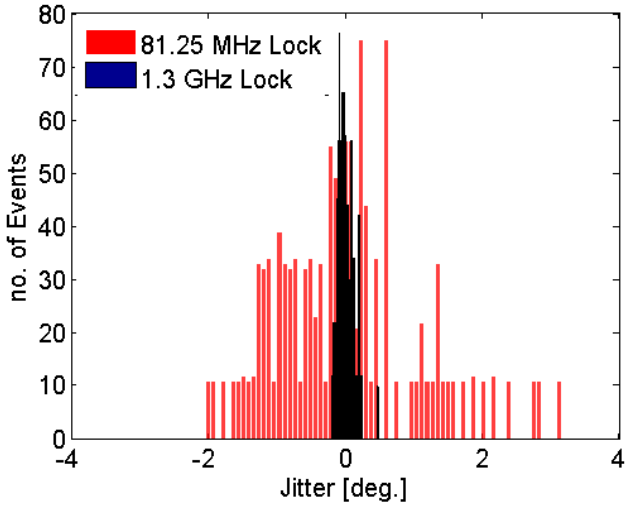

Figure 4.7: A histogram of 70 bins of the data presented in Fig. 4.6.

CHAPTER 5

LINEAR AND MULTIPHOTON PHOTOMISSION FROM CESIUM TELLURIDE PHOTOCATHODE

Photocathodes are excellent sources for production of short electron bunches. In addition to producing beams with high brightness, photocathodes naturally produce short bunches with durations comparable to those of the drive laser. Therefore, production of bunches much smaller than the RF period (order of ~ 100 ps) are possible by using picosecond drive laser pulses combined with fast-response photocathodes. Photoemission allows generating higher peak current bunches when compared to field- and thermionic emissions, and also with overall small transverse beam emittance. The high peak current comes at the expense of lower average current (limited by the laser repetition rate). Development of high-energy high repetition rate lasers is an active area of research. Generation of polarized electron bunches is also possible using photocathodes, e.g. using Gallium Arsenide (GaAs) [44] photocathode. One important figure of merit associated with a photocathode is the quantum efficiency (QE), defined as the number of electrons emitted per photon impinged. Experimentally, we can calculate the QE (here designated as η) of a photocathode based on the correlation between the charge emitted Q by a given photocathode and the corresponding drive laser energy $\mathcal{E}$ as follows

$$\eta = \frac{N_e}{N_p} = \frac{Q/e}{\mathcal{E}/hc\lambda^{-1}} = \frac{Q}{\mathcal{E}}\left(\frac{hc}{\lambda e}\right), \tag{5.1}$$

where N_e is the number of electrons emitted, N_p is the number of photons impinged, λ is the wavelength of the drive laser, e is the electronic charge, h is the Planck's constant, and c is the velocity of light. Metallic photocathodes have prompt emission response times when compared to semiconductor photocathodes, but have lower quantum efficiencies (10^{-3} to 10^{-2} %) due to higher reflectivity of the laser and electron-electron scattering of the excited electrons. Hence semiconductor photocathodes are good candidates for generation of high charge bunches. QEs of up to 40% and 11% have been attained for respectively GaAs [45] and Cesium Telluride (Cs_2Te) [46] cathodes. However, semiconductor photocathodes have some disadvantages including the requirement of ultra-high vacuum (UHV) and their shorter lifetimes when compared to metallic photocathodes.

Photoemission can occur only if the energy of the incoming photon is at least the photoemission threshold of the photocathode. Figure 5.1 shows the band diagram of a p-type semiconductor, where characteristically the Fermi level is closer to the valence band than it is to the conduction band. The work function (ϕ) is defined as the energy difference between the Fermi level and vacuum level, while the photoemission threshold is the energy difference between the maximum of valance band and vacuum level; see Fig. 5.1. Thus the photoemission threshold in semiconductors is higher than the work function unlike in metals where they are equivalent (since for metals the Fermi level lies in the upper levels of the valence band). The first process of photoemission, the photoexcitation leading to photoemission, happens when an electron in the valence band absorbs a photon of energy $h\nu$ greater than the photoemission threshold, and excites to the conduction band. More details of photoemission processes are discussed later in this chapter.

Cs_2Te is a commonly used semiconductor photocathode due to its high quantum efficiency and good lifetime [47, 48]. The QE of Cs_2Te can largely vary from

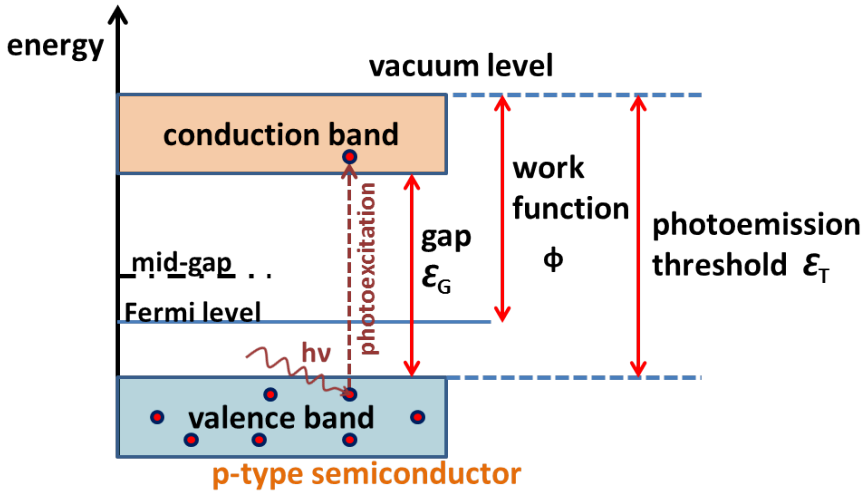

Figure 5.1: Energy band diagram of a p-type semiconductor [49]. Photoexcitation leading to photoemission happens when an electron in the valence band absorbs a photon of energy $h\nu$ ($h\nu > \mathcal{E}_T$) and excites to the conduction band.

4-20% [48] depending on the vacuum level, composition, and the exact cathode preparation synthesis [50]. The photoemission threshold of Cs_2Te can be $\mathcal{E}_T \sim 4.5$ eV, corresponding to the laser wavelength of 266 nm falling in the ultra-violet (UV) region of the electromagnetic spectrum. Since most of the commercially available lasers include lasing media with high gain in the infrared (IR), frequency upconversion to the UV is often required for linear photoemission from metallic and some semiconductor cathodes. For Titanium Sapphire (Ti:Sapph) based systems ($\lambda \approx 800$ nm), UV pulses for photoemission are obtained from frequency tripling of the IR pulses using a two-stage process consisting of a second harmonic generation (SHG) stage followed by a sum frequency generation (SFG) as discussed in Section 3.7. In order to preserve the short pulse duration during the upconversion process, both processes generally use thin BBO crystals, which results in low IR-to-UV conversion efficiency typically $< 5\%$. There is further reduction in the UV energy due to the absorption of UV by the nonlinear crystals. This limitation along with re-

cent results with regards to a copper photocathode [52] prompted us to explore possible multiphoton photoemission from Cs_2Te using a Ti:Sapph laser, given its capability to achieve high intensity. If an IR laser were to be used for photoemission of Cs_2Te, then more than one photon emission—specifically three-photon emission (simultaneous absorption of three photons by one electron)—has to take place if we assume the charge emission is strictly from photoemission and the photoemission threshold is unaltered. Our goal here is to explore the possibility of the multiphoton photoemission from Cs_2Te at HBESL. The study explains whether Cs_2Te exhibits any significant nonlinear (multiphoton) photoemission; and if such a nonlinear photoemission has any practical importance with regards to improving the overall photoemission efficiency when compared to the performance of ordinary (single-photon) photoemission.

5.1 Spicer's Three-step Model

Spicer developed the first photoemission model in 1958, specifically for semiconductors, which is commonly referred to as the 'three-step model' (TSM) [51]. This model explains photoemission by treating it as a bulk effect as opposed to an earlier belief that photoemission was a surface effect. The TSM describes that photoemission from semiconductor photocathodes happens in three steps, hence the name. In the first step, an electron absorbs a photon and gets excited from the valance band to the conduction band. In the second step, the excited electron transports to the surface. In the third step, the electron escapes to the vacuum level resulting in emission. Each of these steps is associated with the corresponding factor(s) that represent the probability of the particular step happening, derived from the bulk

optical and surface properties of the photocathode. The following derivation of QE using the TSM helps understand multiphoton photoemission [51].

Essential to the TSM is the recognition that bulk absorption (attenuation) coefficient governs the excitation of photoelectrons. The light intensity $I(x, hv)$ after it traverses a thickness x of the solid is given by

$$I(x, h\nu) = I_0(h\nu)[1 - R(h\nu)]e^{-\alpha(h\nu)x} \tag{5.2}$$

where I_0 is the intensity of the incident light of photon energy $h\nu$; $R(h\nu)$ is the light reflectivity from the surface of the solid; $\alpha(h\nu)$ is the attenuation coefficient of the medium.

The light intensity absorbed (not necessarily for photoexcitation) in the bulk of the element dx at a distance x from the surface is given by

$$dI(x) = [1 - R]I_0 e^{-\alpha(h\nu)x}\alpha(h\nu)dx. \tag{5.3}$$

A fraction of the intensity $dI(x)$ will photoexcite some electrons in the element dx at a distance x from the surface, some of which will travel to the surface and escape. The contribution from the element dx to the overall photoelectron yield is given by

$$di(x) = P_{0\alpha}(h\nu, x, dx)P_T(h\nu, x)P_E(h\nu) \tag{5.4}$$

where $P_{0\alpha}$ is the probability of exciting the electrons in the element dx above the vacuum level, which is given as

$$P_{0\alpha} = \alpha_{PE}(h\nu)I(x)dx = \alpha_{PE}(h\nu)I_0[1 - R]e^{-\alpha(h\nu)}xdx, \tag{5.5}$$

where α_{PE} represents the coefficient of absorption for the vacuum level, or the number of electrons that are excited to the vacuum level that can possibly photoemit, per unit laser intensity available in the element dx. It is this step that distinguishes between single-photon photoemission from multiphoton photoemission. In single-photon photoemission the intensity dependence of QE goes away (if other nonlinear processes are ignored), as we'll see in Section 5.2. In multiphoton photoemission α_{PE} additionally depends on the intensity of the light besides $h\nu$, as the nonlinear "simultaneous" absorption of multiple photons (of lower energy) has to occur to excite an electron to the vacuum level. Hence shorter laser pulses are required for higher order photoemission. Once the electrons get excited, the rest of the emission processes i.e. electron transport to the surface and electron escape are independent of the order (the number of photons involved per electron excitation) of photoemission.

$P_T(h\nu, x)$ is the probability that electrons in the element dx will reach the surface with sufficient energy to escape. These electrons should not have undergone scattering to reach the surface, the probability of which decreases with the depth x of the element.

$$P_T(h\nu, x) = e^{-x/L(h\nu)}, \tag{5.6}$$

where L is called the escape length defined as the distance traveled by an electron perpendicular to the surface before undergoing scattering. $P_E(h\nu)$ is the probability that an electron at the surface with sufficient energy to escape, escapes. Now expanding the contribution of the element dx to the overall photoelectron yield in terms of all the parameters we have

$$di(x) = I_0[1-R]\alpha_{PE}(h\nu, I)e^{-\alpha x}e^{-x/L}P_{E(}h\nu) \tag{5.7}$$

For a semi-infinite slab, the total electron yield is

$$i(h\nu) = \int_0^\infty di(x) = I_0[1-R]\frac{\alpha_{PE}}{\alpha + 1/L}P_E(h\nu). \tag{5.8}$$

The QE is therefore given as

$$\eta = \frac{i(h\nu)}{I_0} = [1-R]\frac{P_E\alpha_{PE}(h\nu)/\alpha}{1+1/\alpha L}. \tag{5.9}$$

Here all the parameters are functions of $h\nu$. The estimation of the variables in Eq. 5.9 depends on the type and the structure of the material. For example, L for metals is to be derived from the dominating mode of electron–electron scattering, while for semiconductors electron–lattice scattering must be considered [51].

Fowler-Dubridge model is derived for photoemission for metallic photocathodes based on the three-step model. Multiphoton emission has been experimentally observed in metallic photocathodes like copper [52, 53], tungsten, molybdenum [54] but not for semiconductor photocathodes like Cs_2Te so far.

Rewriting the Eq. 5.1 in engineering form for the two wavelengths of interest i.e. 800 nm (IR) and 266 nm (UV) we get

$$\eta_{UV} = 4.7 \times 10^{-6}\frac{Q[pC]}{\mathcal{E}[\mu J]}, \tag{5.10}$$

$$\eta_{IR}(E) = 1.6 \times 10^{-6}\frac{Q(\mathcal{E})[pC]}{\mathcal{E}[\mu J]}. \tag{5.11}$$

Usually, the QE is not defined for a multiphoton photoemission process as the ratio $Q/\mathcal{E}$ is not a constant since it increases with the laser energy (due to the intensity dependence of α_{PE}). But we can define η_{IR} as a function of $\mathcal{E}$ as described by Eq. 5.11 to provide a basis for comparison with single-photon emission.

5.2 Multiphoton Processes

Multiphoton processes are the light–material interactions where more than one photon is involved. These processes are nonlinear functions of the applied electromagnetic field. Examples of multiphoton processes include harmonic generation and multiphoton absorption. Multiphoton photoemission can be explained by multiphoton absorption where two or more photons are simultaneously absorbed to excite an electron from its initial to final state. The order of the photoemission is determined by the number of photons that are involved in the absorption. In the case of multiphoton photoemission, in the first step of the three-step model, α_{PE} additionally depends on the intensity I. This nonlinear dependency is not material specific (unlike the constant of proportionality) and can be shown using higher order perturbation theory [55]. If $\mathcal{H}$ is the Hamiltonian of the electron (material) system, and $\mathcal{H}'(t)$ is the time-dependent perturbation introduced to the system given as

$$\mathcal{H}'(t) = \sum_j e\mathbf{r_j}.\mathbf{E_0} \cos \omega t, \tag{5.12}$$

the rate of electronic transitions from an initial state of $|i\rangle$ to a final state of $|f\rangle$ can be solved for in terms of I. Here $\mathcal{H}'$ is written in terms of the dipole interaction between the electrons and the incoming laser as it is the main contribution. $\mathbf{r_j}$ is the position vector of the electron j, and $\mathbf{E_0}$ is the vector amplitude of the interacting

laser with angular frequency ω. The general equation for the rate of electronic transitions $R_{i\to f}$ from state $|i\rangle$ to state $|f\rangle$ is given using perturbation (higher-order) theory as [55]

$$R_{i\to f}(t) = \frac{2\pi}{\hbar^2}\Bigg|\langle f\,|\mathcal{H}'|\,i\rangle + \frac{1}{\hbar}\sum_{l}\frac{\langle f\,|\mathcal{H}'|\,l\rangle\langle l\,|\mathcal{H}'|\,i\rangle}{\omega_i-\omega_l}\ldots$$
$$+\sum_{l_1}\sum_{l_2}\ldots\sum_{l_{n-1}}\frac{\langle f\,|\mathcal{H}'|\,l_1\rangle\langle l_1\,|\mathcal{H}'|\,l_2\rangle\ldots\langle l_{n-1}\,|\mathcal{H}'|\,i\rangle}{(\omega_i-\omega_{l_1})(\omega_i-\omega_{l_2})\ldots(\omega_i-\omega_{l_{n-1}})}\Bigg|^2$$
$$\times\delta(\omega_i-\omega_f), \tag{5.13}$$

where the states $|l\rangle$ in the above equation represent the intermediate *virtual* states, ω_l represent the light frequencies corresponding to the states $|l\rangle$, and the other symbols have their usual meanings. A virtual state is not an eigen state, so the system is never observed in that state. An electron cannot get excited to a virtual state, so virtual states can be only seen as a mechanism of an electronic transition to a real state. Harmonic generation happens via virtual states where no electronic transitions happen, hence the net effect is equivalent to multiple photons *combining* into a single photon. In multiphoton absorption, transitions happen between the eigen states $|i\rangle$ and $|f\rangle$ via virtual states $|l\rangle$. In Eq. 5.13, we look at the necessary n^{th} term for the corresponding n-photon process (absorption). Hence we can see that $R^{(n)}_{i\to f} \propto (E^n)^2$ where E is the laser electric field magnitude $E_0\cos(\omega t)$; or

$$R^{(n)}_{i\to f} \propto I^n, \tag{5.14}$$

where $R^{(n)}$ is the rate of electronic transitions for an n-photon process, here the n-photon absorption. Hence we determine an n-photon photoemission based on the

experimental relation between the drive laser intensity and R (in Eq. 5.14) which represents the charge emitted. The generalized Fowler-Dubridge (FD) theory for metals gives the emitted current density J from a metallic cathode as the sum of partial current densities J_n emitted through the corresponding n-photon photoemission as [56]

$$J = \sum_n J_n(h\nu) = \sum_n a_n \Big[\frac{e}{h\nu}(1-\mathcal{R}_\nu)I\Big]^n AT^2 F\Big(\frac{nh\nu - e\Phi}{K_b T}\Big), \tag{5.15}$$

where a_n is related to α_{PE}, A is the Richardson's constant, e is the electronic charge, $h\nu$ is the drive laser photon energy, $\mathcal{R}_\nu$ is the reflectivity of the cathode material at frequency ν, T is the mean electronic temperature, F is the Fowler function, Φ is the work function, and K_b is the Boltzmann constant. The relation between I and J in FD theory is still valid for semiconductors since the FD theory follows TSM approach. In Eq. 5.15 if we write $J_n = \frac{Q_n}{\tau\mathcal{A}}$ and $I = \frac{\mathcal{E}}{\tau\mathcal{A}}$ we get the relation

$$Q_n \propto \frac{\mathcal{E}^n}{\tau^{n-1}\mathcal{A}^{n-1}}, \tag{5.16}$$

where Q_n is the charge emitted through n-photon photoemission, $\mathcal{E}$ is the laser energy, τ is the laser pulse duration, and $\mathcal{A}$ is the laser transverse spot area. Equation 5.16 shows the equivalence of τ and $\mathcal{A}$, in the sense that both parameters have equivalent effects on I. Further, writing the QE as proportional to $Q/\mathcal{E}$ we get the relation

$$\eta_n \propto \frac{Q_n}{\mathcal{E}} \propto \frac{\mathcal{E}^{n-1}}{\tau^{n-1}\mathcal{A}^{n-1}}. \tag{5.17}$$

From relation 5.17 we see that in single-photon photoemission ($n = 1$), the QE doesn't depend on the laser total energy, spot size or the duration contrary to the case for multiphoton photoemission ($n > 1$).

5.3 QE Measurement for a Cs_2Te Photocathode

The QE of the Cs_2Te photocathode at HBESL can be measured using the traditional 266 nm UV laser for any future comparison with the photocathode's performance using 800 nm infrared (IR) laser. For the calculation of the QE of a cathode experimentally, one needs to know the charge emitted by the cathode per unit laser energy input. Hence, the charge emitted and the energy input must be properly measured for the accuracy of the experimental measurement of the QE. The following is the procedure that has been employed at HBESL to measure the QE of Cs_2Te cathode using UV laser.

In order to obtain the charge emitted per unit energy by a particular pulse of the drive laser, simultaneous measurements of both the charge and the laser energy is required, especially in cases where there are laser energy fluctuations from pulse-to-pulse. Therefore, splitting the laser pulse using a beam splitter (BS) and measuring a known fraction of the laser energy directed into the photoinjector will lead to the correct estimation of the laser energy directed into the photoinjector and emitting the charge. Figure 5.2 shows the set up used at the HBESL photoinjector.

Say, detector P measures a fraction of the actual laser energy directed into the photoinjector. Now the task will be to calculate that fraction to know the actual laser energy being directed onto the photocathode surface. In order to do that, we place detector C in front of the photoinjector, in the path of the drive laser

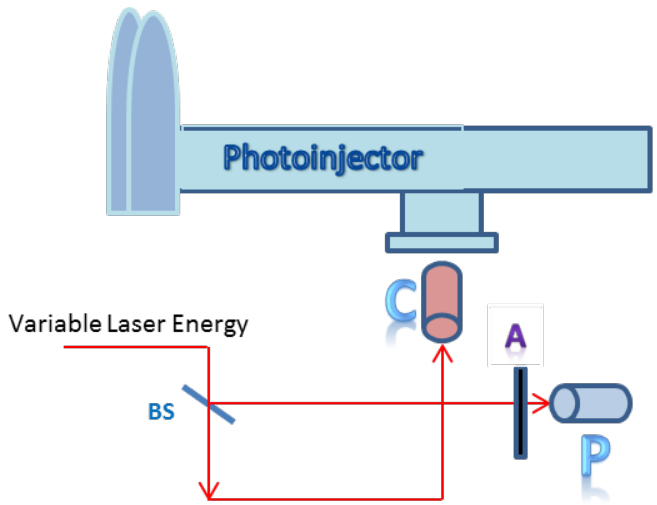

Figure 5.2: Schematic of the setup used at the HBESL photoinjector to calibrate the laser energy. Detectors P and C, and an attenuator 'A' are shown.

and measure simultaneously the readings of detectors P and C for different laser energies. If detector C itself is not calibrated, meaning that the voltage measurement of detector C (V_C) doesn't represent the absolute laser energy, then calibration of detector C is required. An energy meter available at HBESL may not be used in the place of detector C as the range of the laser energy directed into the photoinjector is well below the range of the energy meter.

Varying the laser energy: since the UV laser is polarized, a combination of a half-wave plate (HWP) and a polarizer can be used to vary the laser energy (see Fig. 5.3). By rotating the HWP ($\lambda/2$ in the figure), the polarization of the laser is rotated accordingly and subsequently the intensity out of the polarizer is changed, as the polarizer transmits only the polarization component parallel to its optical axis. It can be noted that the single-photon emission from a cathode is independent of the polarization of the drive laser for normal incidence as in our configuration.

We use an energy meter (LaserProbe RM-3700) that measures the absolute laser energy ($\mathcal{E}$). The accuracy of this energy meter is cross checked with a calibrated

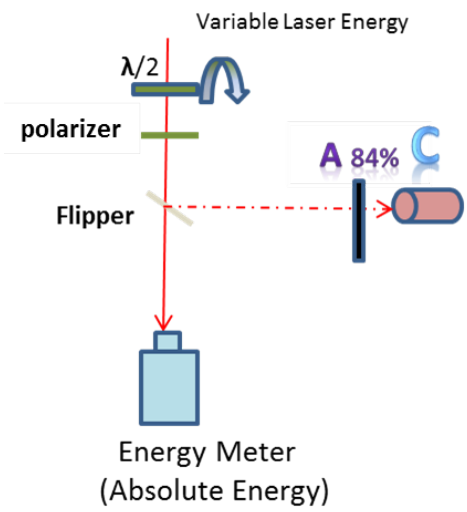

Figure 5.3: Schematic showing the calibration of detector C with an energy meter. '$\lambda/2$' is the HWP, 'A' is the 84 % attenuator.

power meter. We may not be able to make simultaneous measurements of the laser energy using the energy meter and detector C (V_C) due to the unavailability of proper BS. Hence a 10 point average of the readings of the energy meter and detector C are compared to calibrate detector C. So the average of the first 10 laser pulse energies by the energy meter are recorded against the average of the next 10 laser pulse energies recorded by detector C for a given set point of the laser energy. The 10 point average reduces the error due to slight energy fluctuations from pulse-to-pulse. The process is repeated for different UV energy set points. The energy meter has a built-in feature to average a given number of measurements; and the averaging of the detector C readings (V_C) is done by a computer program. Online digitizer channels are used to acquire the data from the instruments and can be accessed by the program. A flipper mirror is used to manually aim the laser beam into the energy meter and detector C alternatingly, for every 10 pulses of the laser (see Fig. 5.3). A verified 84% attenuator is used in front of detector C as the direct laser energy saturates the detector. The actual reading of the detector is determined after taking

the attenuation into account. Figure 5.4 confirms the linear relationship between $\mathcal{E}$ and V_C. From a linear fit we obtain

$$\mathcal{E}[\mu\text{J}] = 0.7V_C[\text{V}] - 0.81. \tag{5.18}$$

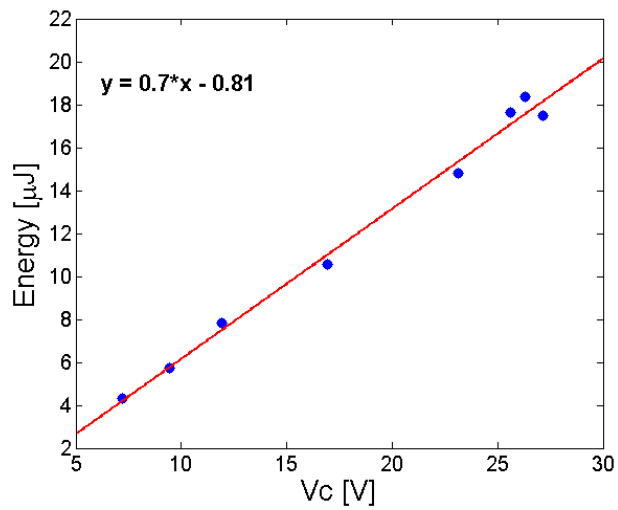

Figure 5.4: Energy ($\mathcal{E}$) as a function of detector C voltage.

Calibration of detector P with detector C: now that detector C is calibrated to the actual laser energy, calibrating it with respect to detector P will allow us to estimate the actual drive laser energy based on the detector P (V_P) data (setup shown in Fig. 5.2). It can be noted that the attenuator 'A' in front of detector P is installed only to prevent the detector from saturation and does not interfere with the calibration as long as A and detector P are used together. Simultaneous recordings of the data, for different laser energies, from detectors C and P are done by connecting the detectors to their respective digitizer channels and storing the data corresponding to the laser energy values using a computer program. Figure 5.5 shows the data and the calibration between detectors C and P. From a linear fit we have

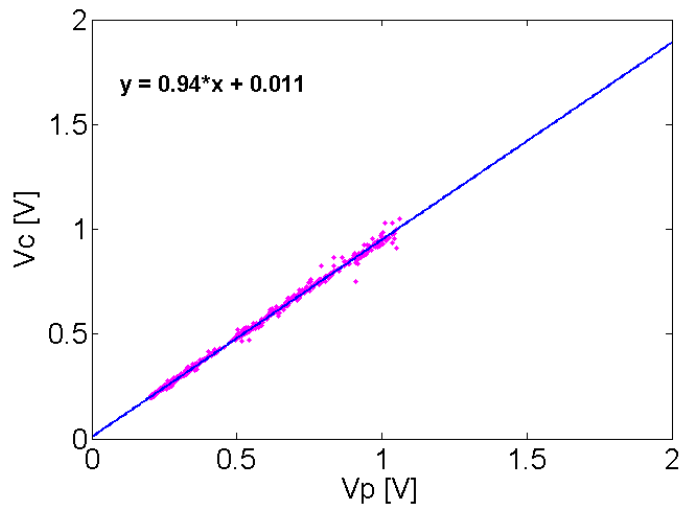

Figure 5.5: Detector C voltage as a function of detector P voltage.

$$V_C = 0.94V_P + 0.011. \tag{5.19}$$

Combining Eq. 5.18 and Eq. 5.19, we finally arrive at an absolute calibration for detector P as

$$\mathcal{E} = 0.66V_P - 0.8023. \tag{5.20}$$

Charge vs. detector P voltage: the charge emitted by the photocathode is obtained from the integrated current transformer (ICT) installed downstream of the RF gun. The corresponding laser energy is calculated based on the voltage reading from detector P (V_P) using Eq. 5.20. Figure 5.6 is the plot of charge Q vs. detector P voltage (V_P). From a linear fit in Fig. 5.6, we obtain the relationship between the emitted charge and the detector P voltage;

$$Q[\text{nC}] = 0.3V_P[\text{V}] - 0.068. \tag{5.21}$$

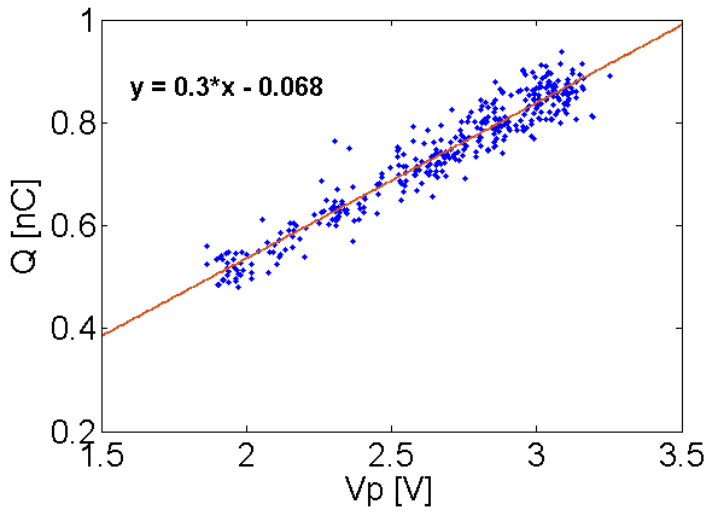

Figure 5.6: Charge emitted as a function of detector P voltage.

From Eq. 5.20 and Eq. 5.21, we get

$$Q[\text{nC}] = 0.459\mathcal{E}[\mu\text{J}] + 0.300. \tag{5.22}$$

Equation 5.22 shows the experimental absolute relation between the charge Q[nC] emitted by the Cs_2Te photocathode and the UV drive laser energy $\mathcal{E}[\mu\text{J}]$. Figure 5.7, which was plotted using Eq. 5.20 and Fig. 5.6, represents the same. The norm of residuals shown in the plot is defined as the square root of the sum of the squares of the differences of the data points from the fit line. Substituting $Q[\text{pC}]/\mathcal{E}[\mu\text{J}] = 459$ in Eq. 5.10, we obtain $\eta = 0.00216$ or

$$\eta_{UV} = 0.216\%. \tag{5.23}$$

Over the last decade, $\eta_{UV} \simeq 0.2\%$ has typically been measured at the same facility.

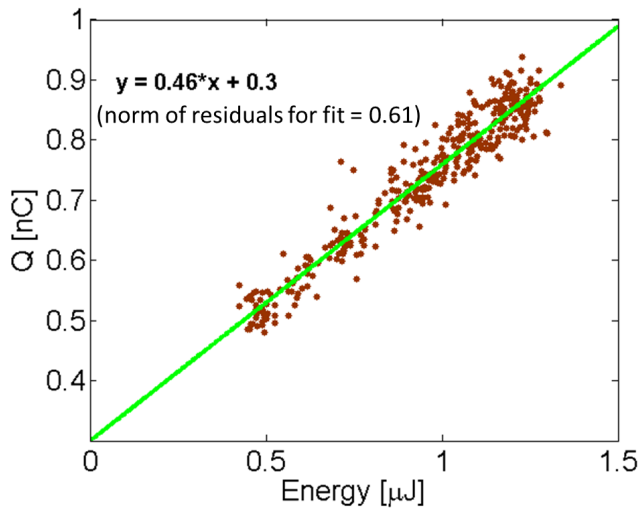

Figure 5.7: Charge emitted as a function of UV laser energy.

5.4 Multiphoton Photomission from Cs_2Te using 800-nm IR Laser

Obtaining the plot of charge Q vs. laser energy $\mathcal{E}_{IR}$ for the 800-nm IR follows similar procedure described in the previous section, except that detector C can directly be replaced with the energy meter as the IR pulses have an average energy of about couple mJ per pulse—enough for the energy meter to detect. Hence the calibration of detector P is directly done without the involvement of detector C. Appropriate attenuator 'A' (Fig. 5.2) is chosen to prevent detector P from saturation.

The energy meter and detector P are connected to digitizer channels for simultaneous measurements of both readings. Figure 5.8 shows the calibration between the drive laser energy ($\mathcal{E}_{IR}$) and V_P which corresponds to 150 μJ/V.

The IR pulses were directly sent to the photocathode to check for any charge emission. The charge was measured using the Faraday cup (FC) as the ICT does not provide sufficient sensitivity for low charge values ($<$ 50 pC) produced in this

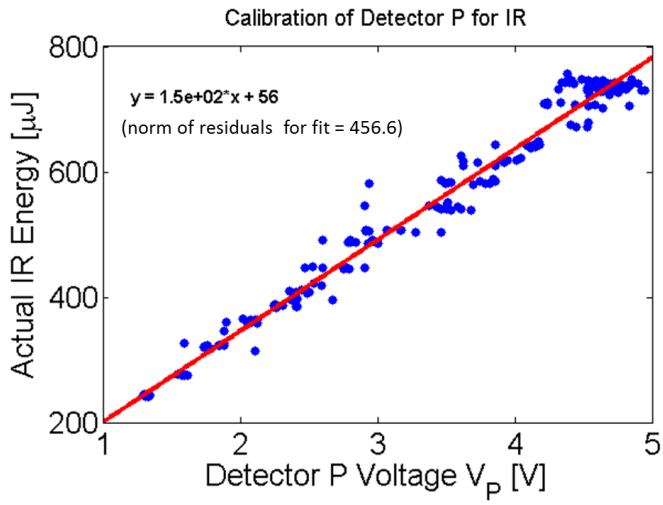

Figure 5.8: IR Laser energy ($\mathcal{E}_{IR}$) as a function of detector P voltage.

experiment. One good way to check for photoemission is to see if the charge emitted varies with the relative phase between the laser and the RF gun. Three different laser spot sizes were considered to study the effect of the energy flux (energy per unit area) on the charge emission process. Figure 5.9 left images show the laser beams corresponding to the three spot sizes considered. The sizes of the spots were measured as the rmsd (rms deviation) of their vertical laser intensity profiles as shown in the figure, on the right. A smaller spot would mean higher energy flux for a given total energy of the laser pulse. The shape of the phase scan traces for the three laser spot sizes, viz. 'Smaller', 'Medium' and 'Bigger' spots, shown in Fig. 5.10 confirms that the charge yield is from photoemission (compare with Fig. 4.1), since any other emission process is independent of the laser–RF phase. Figure 5.11 shows the charge yield in the FC as a function of the laser energy for the same three laser spots.

The stronger (nonlinear) dependence of the charge on the laser energy for the smaller spot size indicates that higher energy flux (J/m^2) produces higher charge in

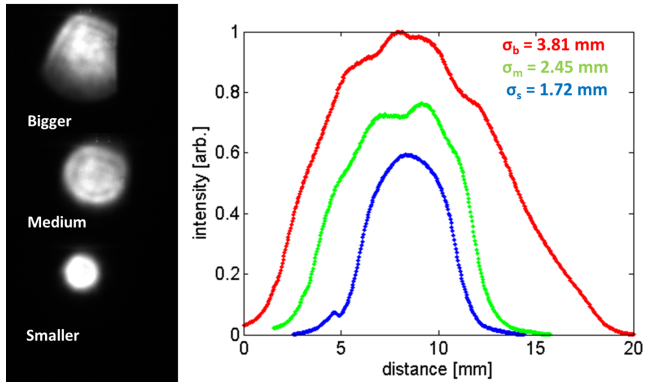

Figure 5.9: Images of the laser beam corresponding to the three spot sizes considered (left) and their corresponding intensity projections along the vertical direction.

photoemission from the IR laser. Taking the laser's transverse density to follow a Gaussian distribution, smaller spot sizes obtained by clipping a larger spot impinges a higher laser flux for a given IR laser pulse energy and hence produces a higher charge. The nonlinear signature of the charge–energy traces reported in Fig. 5.11 hint to a nonlinear photoemission process. To further quantify the dependence of the charge on the laser energy, we plot the data represented by Fig. 5.11 on a log-log scale; see Fig. 5.12. The overall linear regression of the data confirms that the charge scales as $Q \propto I^2$ (where I is the laser intensity) suggesting that two-photon photoemission is the dominant process rather than the anticipated three-photon photoemission, based on Eq. 5.16. Also, the data suggests that the modified photoemission threshold of Cs_2Te–or otherwise the emitting material–for such a two-photon photoemission is < 3.1 eV, the energy corresponding to two photons of 800-nm laser. Some data points at lower charge/energy values with possible higher contribution from background noise were omitted for linear curve fitting.

We would like to look at Eq. 5.15 and confirm that the experimental data is within the equation's realm, meaning that there are no additional significant non-linear processes that have not been accounted for, e.g. material evaporation resulting

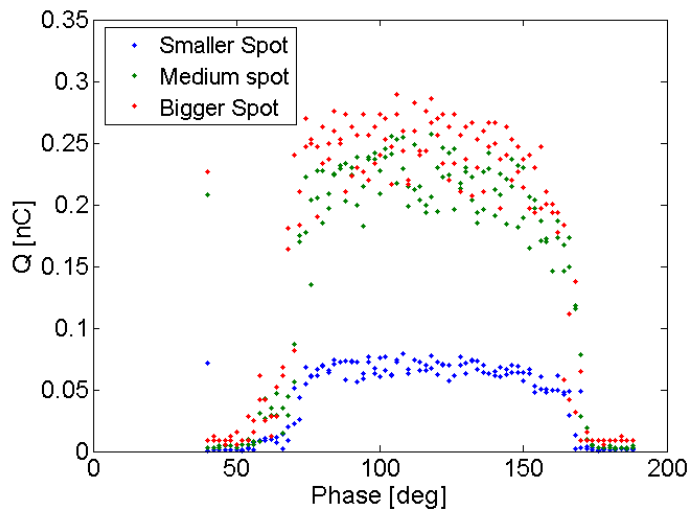

Figure 5.10: Charge dependence on the laser–gun relative phase (with an arbitrary phase offset). The blue, green, and red traces correspond respectively to the laser spot radii of 1.72, 2.45 and 3.81 mm on the photocathode.

from excessive laser heating. From Eq. 5.15, we get $J_2 = \mathcal{C}I^2$ for the current case, where $\mathcal{C}$ is a constant dependent on the material. More conveniently, we have

$$\log J_2 = 2\log I + \log \mathcal{C}. \tag{5.24}$$

where J_2 is the current density [C/m^2] and I is the laser intensity [W/m^2]. In Fig. 5.13, we see that the above equation holds well for all the three spot sizes, i.e all the three linear curves line-up closely with the y-intercept being $\log C \sim -5$. The yellow lines are the linear fits corresponding to the fit equations shown. The pink line in the figure corresponds to the linear photoemission from UV, which has a slope of unity (on a logarithmic scale); this was obtained by computing $J = \frac{Q}{\tau\mathcal{A}}$ and $I = \frac{\mathcal{E}}{\tau\mathcal{A}}$ from the linear fit (Q vs. $\mathcal{E}$) of the data corresponding to Fig. 5.7, where $\tau = 100$ fs and $\mathcal{A} = 45.6$ mm^2. In comparison with the two-photon photoemission, the UV yield can be noted to be several orders of magnitude higher than that of IR emission. The point of intersection between the IR and UV curves, if extrapolated in

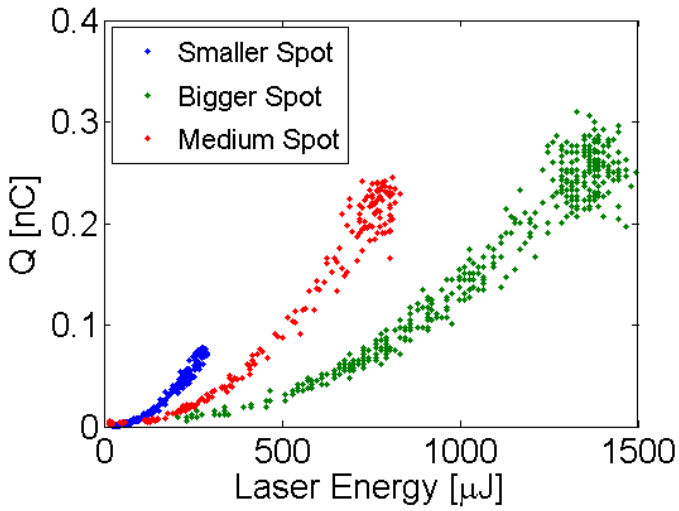

Figure 5.11: Charge variation as a function of laser energy for the three laser spot sizes considered in Fig. 5.10.

Fig. 5.13, happens at a much larger intensity scale than the experimental range; this indicates that the intrinsic efficiency of IR emission is well below that of UV emission in the intensity scale of practical importance. This indication is in contrast to the three-photon photoemission from Cu studied in [52], where the UV and IR emission curves (J vs. I) intersect within the experimental scale of intensity, suggesting that IR emission from Cu is preferential to the UV emission around $I \sim 20$ GW/cm^2. This observation can be attributed to two reasons; three-photon photoemission has a steeper slope (3) than two-photon photoemission (2), and the linear (UV) QE of Cu considered in [52] is $\simeq 100$ times lower than that of Cs_2Te considered in this study.

Photoemission is generally an independent process from charge acceleration, except in the cases where large accelerating gradients modify the emission properties of the photocathode. The charge yield out of the RF gun depends also on the electron beam dynamics subjected to the accelerating gradient in the gun. Figure 5.14 shows the log-log plots of charge as a function of laser energy for different acceler-

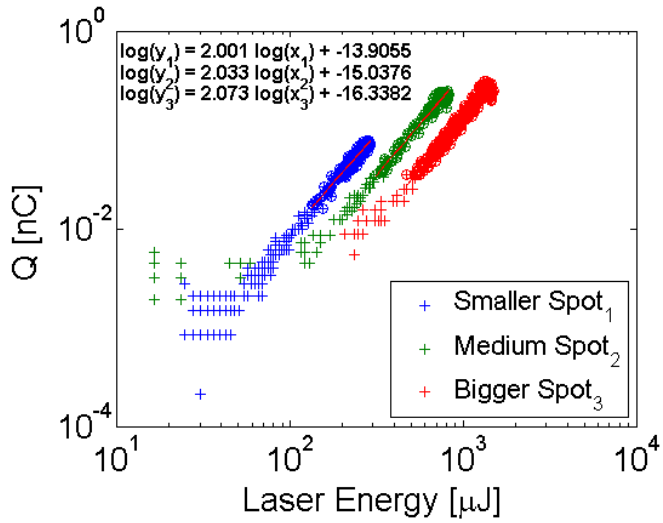

Figure 5.12: Logarithmic plots corresponding to the data presented in Fig. 5.11.

ating gradients (AD values) for the medium laser spot size. For a given logarithmic curve $\log(y) = n\log(x) + C$, the coefficient A of $y = Ax^n$ can be calculated as $A = \exp(C)$. In our case, $n = 2$ and A is the quadratic coefficient. The inset in Fig. 5.14 shows the variation in the quadratic coefficient with the accelerating gradient. This implies that a higher accelerating gradient does not necessarily yield a higher charge, because the collective effects of the work function modification (at high AD values) and image charge effects at high charge densities dictate the charge yield out of the RF gun.

Re-writing Eq. 5.11 for $\%\eta_{IR}$ in more convenient units of charge Q in nC gives

$$\%\eta_{IR}(\mathcal{E}) = 0.16 \times \frac{Q(\mathcal{E})[nC]}{\mathcal{E}[\mu J]}. \tag{5.25}$$

The quadratic coefficient A gives a measure of η_{IR} since $Q/\mathcal{E} = A\mathcal{E}$ resulting from $Q = A\mathcal{E}^2$ for two-photon photoemission. Therefore Eq. 5.25 for two-photon photoemission becomes $\%\eta_{IR} = 0.16 \times A\mathcal{E}$. From the constant (curve fit) terms in Fig. 5.12 viz. {-13.90,-15.04,-16.34} corresponding to the three laser spot sizes

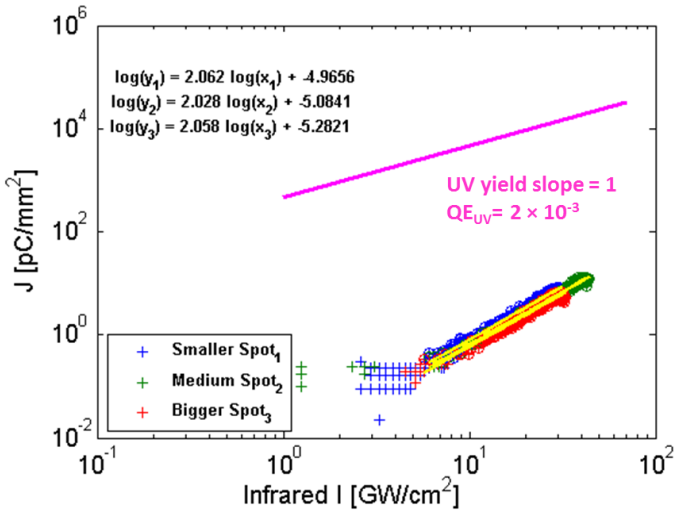

Figure 5.13: log-log plots of charge density vs. laser intensity. The yellow lines are the linear fits for the linear region of the respective data.

Smaller, Medium, and Bigger give the A values $\{9.14\times10^{-7}, 2.95\times10^{-7}, 0.80\times10^{-7}\}$ respectively. Figure 5.15 compares the %QE of the IR photoemission obtained for the different laser spot sizes. The smaller the spot, the greater is the laser flux and higher is the QE as shown in relation 5.17.

In conclusion, two-photon photoemission from Cs_2Te has been observed with a 800-nm IR laser although it is unclear whether such an emission has any contribution from the bulk Cs_2Te material. For instance, surface contamination, defects or grain boundaries can play a role in the two-photon process. A second Cs_2Te photocathode tested also exhibited two-photon photoemission from the IR laser, consistent with the cathode considered in this study. However, we can note that the QE of two-photon photoemission from Cs_2Te, or otherwise the emitting material, is several orders of magnitude ($>$ 6 orders) less than that of the ordinary emission from Cs_2Te, suggesting poor practicality of using such a nonlinear photoemission for the generation of higher charge from Cs_2Te. It can be noticed that at the laser energies where the QE from a nonlinear photoemission becomes comparable to that

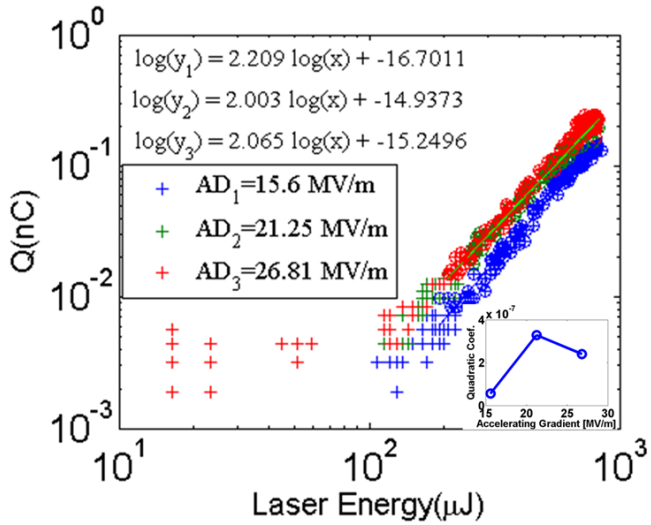

Figure 5.14: The effect of the accelerating gradient on the charge yield. Inset: the variation of the quadratic coefficient with the accelerating gradient.

of the ordinary photoemission, the cathode material's threshold energy must have well past—thus possibly resulting in evaporation of the material. On the other hand, the data presented in the current study can have implications in studies related to multiphoton processes in solid state physics; e.g. in knowing the definitive band structures of Cs_2Te.

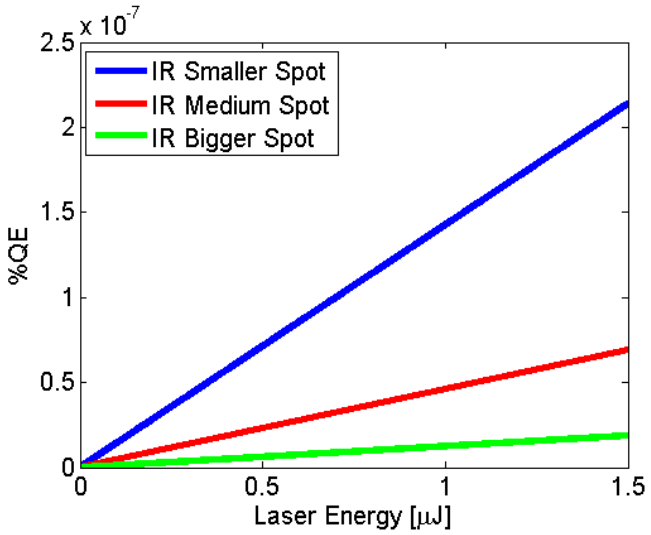

Figure 5.15: Comparison of the QE among the three spot sizes considered in this study.

CHAPTER 6

FIELD EMISSION CATHODES IN RF SOURCE

6.1 Theory of Field Emission

Field emission is an electron emission process where the emission occurs through the quantum mechanical process of tunneling. Considerable number of electrons from a material can tunnel through the surface–vacuum barrier if there are strong (normal) electric fields present at the surface. Such strong fields narrow the barrier potential at the surface as shown in Fig. 6.1, thus increasing the probability of quantum tunneling. Using Wentzel–Kramers–Brillouin (WKB) approximation [57], for the barrier width of $X_2 - X_1$ in Fig. 6.1, the probability of tunneling (transparency) $\mathcal{P}$ through the barrier for an electron at the Fermi level is given as

$$\mathcal{P}(\phi, E) \cong \exp[-\frac{4m}{\hbar^2}\int_{X_1}^{X_2}(\phi - xE)dx], \tag{6.1}$$

where ϕ in the work function of the metal, E is the applied external electric field, m is the electronic mass, $\hbar$ is the reduced Planck's constant.

Strong electric fields are difficult to generate, but field emission is enhanced by surface roughness. For instance, a sharp feature at the surface will locally increase the field in a similar effect as in the case of a lightening rod. If the electron emitting material has sharp features on its surface then a macroscopic electric field of magnitude E around the surface is enhanced to a field of $E_e = \beta_e E$ around the sharp feature where $\beta_e > 1$ is often referred to as the field enhancement factor

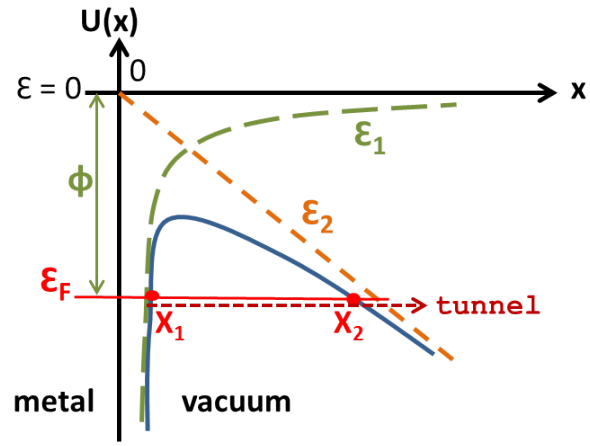

Figure 6.1: Potential energy (PE) U(x) (solid blue curve) of an electron near the surface of a metal (corresponding to x=0), as a function of the distance x from the surface in the presence of strong external electric field at the surface. $\mathcal{E}_1$ is the PE in the absence of the electric field, $\mathcal{E}_2$ is the PE in uniform external electric field alone, and $\mathcal{E}_F$ is the Fermi level of the metal. $X_2 - X_1$ is the potential barrier width in the presence of the electric field.

which depends on the geometry of the tip. The smaller the curvature of the tip, the higher the β_e. Typical local fields on the order of GV/m can be achieved at a rough surface subjected to a macroscopic field of $\sim$ 10 MV/m. Figure 6.2 demonstrates a numerical simulation of field enhancement around a 20-nm diameter metal tip inside a capacitor of size of 1.5 μm radius and 1 μm length with a potential difference of 1000 V between the plates.

Fowler-Nordheim (FN) theory successfully explained field emission in the early nineteenth century using quantum theory. Originally the theory was developed for bulk metals based on some assumptions like planarity of the metal surface (1D problem), temperature $T = 0$ K, and the electrons obeying Fermi-Dirac statistics [58]. Under such assumptions, the amplitude of the local current density j from an emitter is given as [59]

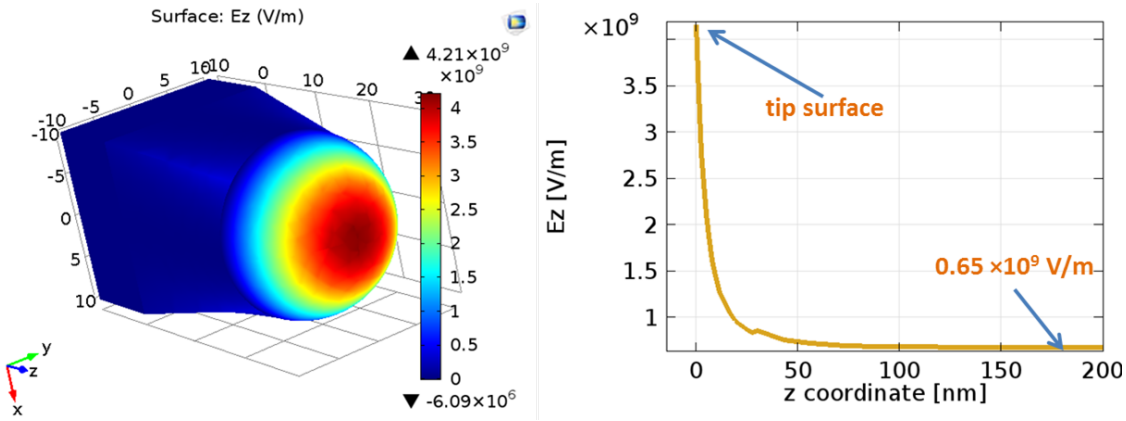

Figure 6.2: Enhancement of electric field around a metallic tip inside a capacitor. The longitudinal field distribution (E_z) on the surface of the tip is shown on the left, while the longitudinal field profile along the capacitor's axis (z) is shown on the right. The field enhancement corresponds to a $\beta_e \simeq 6.5$. The applied macroscopic field is $E \approx 0.65$ MV/m.

$$j = e \int N(\mathcal{E})\mathcal{P}(\mathcal{E}, E_e) d\mathcal{E}, \tag{6.2}$$

where e is the electronic charge and $N(\mathcal{E})$ is the number of electrons present (per unit area) in the energy band $\mathcal{E}$ and $d\mathcal{E}$. The overall current I derived in the FN theory from Eq. 6.2 (also see Eq. 6.1) under the assumption that j is uniform over the emission surface is given as [60]

$$I = j\mathcal{A} = \mathcal{A}a(\phi)E_e^2 \exp\left(\frac{b(\phi)}{E_e}\right), \tag{6.3}$$

where $\mathcal{A}$ is the effective emission area, $a(\phi) = \frac{1.42\times10^{-6}}{\phi}\exp(\frac{10.4}{\sqrt{\phi}})$ and $b(\phi) = -6.56\times 10^9\phi^{3/2}$ (in units of eV) are functions of the work function ϕ of the material, with image-charge correction. Although the FN equation is derived for metals, modifications are done to apply the theory for other materials like semiconductors. In the case of a time-dependent sinusoidal applied electric field

$$E_e = \beta_e \underbrace{E_0 \sin(\omega t)}_{E}, \tag{6.4}$$

where E_0 and ω are the macroscopic field amplitude and the angular frequency respectively, the average current $\bar{I}$ over the RF period T ($\equiv \frac{2\pi}{\omega}$) is obtained as [61]

$$\begin{aligned} \bar{I} = \frac{1}{T}\int_0^T I dt &= \mathcal{A}a(\phi)(\beta_e {E_0}^2)\frac{2}{T}\int_0^{\frac{T}{4}} \sin^2(\omega t)\exp\left[\frac{b(\phi)}{\beta_e E_0 \sin(\omega t)}\right] \\ &\simeq \frac{1}{\sqrt{2\pi}}\mathcal{A}a(\phi)(\beta_e E_0)^{2.5}\exp\left(\frac{b(\phi)}{\beta_e E_0}\right) \end{aligned} \tag{6.5}$$

where I is given by Eq. 6.3. It can be noted that in Eq. 6.5, the effective integration is performed over $T/2$ ($\equiv 2 \times \frac{T}{4}$) instead of T as the electron emission takes place for only half the RF period when the field polarity allows for electron extraction. Overall, the FN theory successfully explains the exponential-like dependence of experimental emission current on the applied field and the work function.

The process of tunneling happens in a finite time which can be defined as the 'tunneling time' τ_{tun}, assumed to be the mean time of interaction between a tunneling electron and the potential barrier. Equation 6.3 is valid when the applied field changes slow enough when compared to τ_{tun}, or $\tau_{tun} \ll \frac{2\pi}{\omega}$ which holds up to frequencies of the order of 10^5 GHz [58]. Hence, HBESL's operating RF frequency of 1.3 GHz is well within the frequency range where Eq. 6.3 is valid.

6.2 Motivation

Field-emitter (FE) sources offer significant advantages over photocathode and thermionic sources due to their ability to be operated without the need for an aux-

iliary laser system or a heating source. The demand for more efficient electron sources lead to the demand for cold cathode driven technologies, particularly FE sources [62]. FE cathodes also offer better portability as they typically do not require high vacuum pressures ($< 1 \times 10^{-5}$ torr). In terms of beam quality, FE cathodes can generate electron beams with low emittance and high average current. Electron beams with near quantum-limited transverse emittance can be produced via extremely small FE tips like carbon nanotube (CNT) and diamond [63]. Consequently FEs have been at the center of electron source developments for the last several years. Examples of applications of FEs can be found in THz vacuum electron sources [64], high resolution x-ray imaging which requires high current density electron beams [65].

Field-emitter arrays (FEA) are fabricated by arranging FEs in an orderly fashion as large arrays, thus can provide high average [66] and uniform currents making them ideal for most applications, e.g. in feild emission displays (FEDs) [58, 62]. Diamond FEAs, in particular, have applications in FELs as they are rugged and generate little heat [67, 68].

CNT emitters (patterned or randomly oriented) can generate substantial enhancement factors of more than 1000 [69]. These geometric properties coupled with low electrical resistance, high thermal stability and robustness at high temperatures can support large current densities making CNTs excellent FEs.

Most of the research done on FEs so far dwells around studies done in DC fields where the beam energy is limited by low accelerating voltage. In the current chapter we report field emission studies of FEs in an RF gun which can produce substantially higher accelerating gradients, on the order of tens of MV/m, when compared to DC electron guns. Consequently, high energy and high average current beams can be generated from FEs using RF fields. Particularly, we report pulsed field emission

studies from a diamond field emission array (DFEA) cathode (Section 6.3) and a CNT cathode (Section 6.4) utilizing HBESL's L-band (1.3 GHz) RF gun.

6.3 Diamond Field Emission Array Cathode in RF Gun

In this experiment, a diamond field emission array (DFEA) cathode was tested in HBESL's L-band RF gun. The DFEA cathode has $\sim 10^6$ diamond tips on their respective pyramids and was synthesized at Vanderbilt University (VU), Tenn. For the test, we chose a cathode with large number of tips to increase the average current.

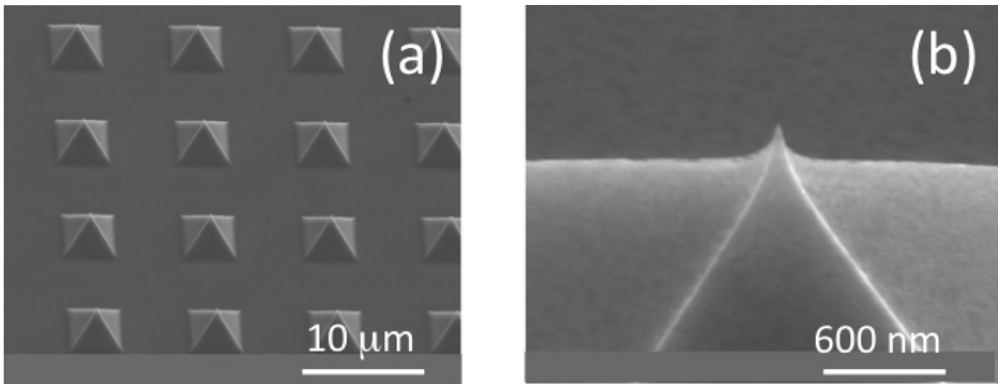

Figure 6.3: An SEM image of the DFEA pattern (a) and an SEM image of a single tip (b). Image courtesy of Bo Choi (Vanderbilt University).

The DFEA diamond tips on the pyramids were deposited on a circular area of 6 mm radius and are approximately separated from one another by 10 μm distance. The typical pyramid base is $\sim$ 4 μm and the radius of curvature of the tip is $\sim$ 10 nm. A scanning electron microscope (SEM) photograph of the DFEA pattern is shown in Fig. 6.3. The array is prepared using an inverse mold-transfer process [68]. Oxidized Si wafers (silica) are patterned (square) over silicon wafer substrates. A potassium hydroxide (KOH) etch on the pattern produces the inverse pyramids with

an opening angle of 70°. Then dry oxidation of the pyramids forms the molds for growing diamond. Due to the preferential oxidation of the silicon over the walls of a pyramid, a sharp recess at the tip of the pyramid is formed allowing for a mold that can produce a sharp tip of diamond at the vertex. Diamond is then grown in the molds with sharp tips using microwave-plasma chemical vapor deposition (MPCVD). With a few more steps, the silicon mold surface is removed and cleaned exposing the DFEA. A wafer was then brazed on a typical HBESL cathode plug; see Fig. 6.4. In the current experiment, FN characteristics were studied for different axial fields on the cathode edge. Current stability over continuous operation for hours, and operation after several months of being idle was tested. Numerical simulations were carried out to understand the field enhancement and field distributions/eigen-frequencies inside the gun for different experimental settings.

Figure 6.4: A photograph of the DFEA cathode brazed on an HBESL cathode plug [14]. The emitter area is the dark circular area on the plug surface.

6.3.1 Numerical Simulations

6.3.1.1 Electromagnetic Modelling

Finite element method (FEM) simulations using COMSOL MULTIPHYSICS® were done to estimate the field enhancement factor β_e and the longitudinal electric field profile near one tip. The simulations were also useful to estimate the tolerances on the longitudinal displacement of the cathode from the nominal position.

COMSOL MULTIPHYSICS® is a commercially available finite element analysis (FEA) multiphysics software that is used in many engineering and physics applications spanning analyses in thermodynamics, mechanics, electro-magnetism, fluid flow etc. [70]. Multiphysics softwares are particularly useful in solving problems involving interdisciplinary subjects of study; however, like in the current study, one can simply use such a software in any particular field of interest. We utilized COMSOL's RF module to perform frequency domain studies of HBESL's RF gun.

In the current study, an RF gun model was created with the dimensions of the HBESL gun. We are interested in the TM_{010} modes of the gun viz. the zero- and the π-modes, which have cylindrically symmetric EM fields if we consider the effect of the input coupler is negligible. Hence only quarter of the gun was modeled as shown in Fig. 6.5 to save computational time, with the appropriate material assignments and boundary conditions specified in Table 6.1.

Assigning the slice surfaces (see Fig. 6.5) the boundary condition (BC) of perfect magnetic conductor makes the problem equivalent to that of having the full gun (when solving for the zero- and the π-modes). All other surfaces were idealized with perfect electric conductor BC for simplicity and to avoid complex electric

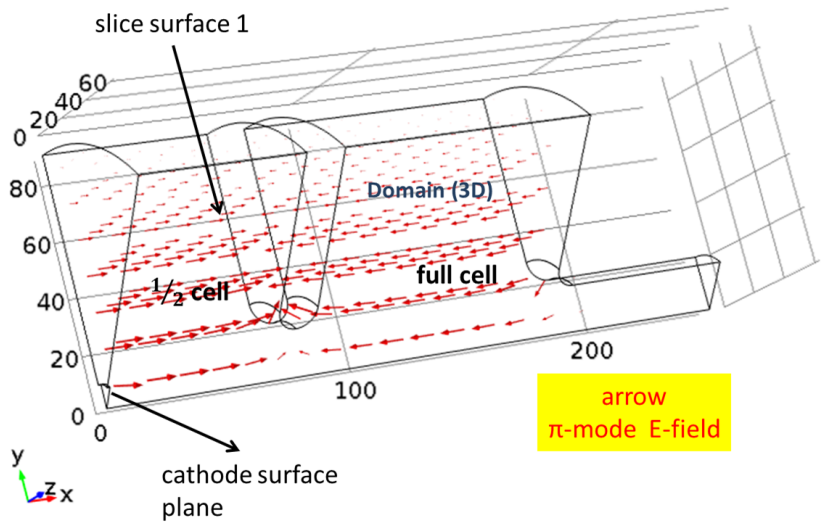

Figure 6.5: Finite element model of the HBESL RF (quarter) gun. The distances shown are in mm.

field/eigenfrequency solutions. The longitudinal position of the cathode surface plane, of size 8.29 mm radius, was parametrized to obtain solution to the first approximation when the cathode is displaced from the nominal position by a known amount.

With the conditions specified in Table 6.1, the following equation is solved in the entire spatial domain (3D) using the default eigenvalue solver available in COMSOL.

$$\nabla \times \mu_r{}^{-1}(\nabla \times \mathbf{E}) \quad = \quad k_0{}^2(\epsilon_r - \frac{i\sigma}{\omega\epsilon_0})\mathbf{E} \tag{6.6}$$

Table 6.1: Important specifications of the finite element modeling of the RF gun.

Object/parameter	Assignment
slice surfaces 1 & 2	perfect magnetic conductor ($\mathbf{n}\times\mathbf{H}=\mathbf{0}$)
all other surfaces	perfect electric conductor ($\mathbf{n}\times\mathbf{E}=\mathbf{0}$)
domain volume material	vacuum ($\epsilon_r = 1$, $\mu_r = 1$)
parametric surface	cathode plane
eigenfrequency solving neighborhood	1.3 GHz

$\mathbf{n}$=surface normal vector, $\mathbf{H}$=magnetic field intensity, $\mathbf{E}$=electric field, ϵ_r=relative permittivity, μ_r=relative permeability

where k_0 is the wave number ($2\pi/\lambda$), λ is the wavelength of the mode, ω is the (angular) eigenfrequency, $i = \sqrt{-1}$ and σ is the electrical conductivity. The electric field vector of the π-mode is plotted in Fig. 6.5 (arrow). In order to get a well balanced peak electric field magnitude in both the $\frac{1}{2}$ cell and the full cell of the gun, the radii of both cells are tuned within a micron. The final axial electric field along the gun's axis is shown in Fig. 2.3.

For the given geometry of the RF gun, the eigenfrequency of the π-mode is obtained to be 1.298686 GHz. Figure 6.6 shows how displacing the cathode along the longitudinal position affects the eigenfrequency of the π-mode and the peak electric field on the cathode surface. Correspondingly, Fig. 6.7 shows how the field profile is perturbed from the nominal case, for different cathode displacements. It can be noted that for the nominal cathode position (cathode displacement set to 0), the default arbitrary peak electric field is $\sim$ 810 V/m. This value can be normalized to any desired peak field. In the experiment [Fig. 6.21 (d)], the case of cathode *retracted* (cathode displacement $\sim$ -2 mm) is also considered for a reason to be explained later. For this case from Fig. 6.6, we observe a 22 % decrease in the peak field from 810 V/m to 630 V/m.

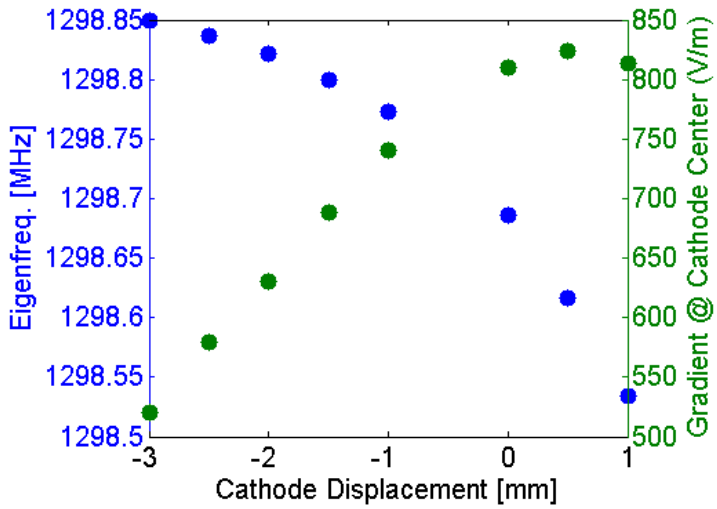

Figure 6.6: Effect of the cathode displacement on the π-mode eigenfrequency and the peak electric field on the cathode surface. The positive displacement is towards the full cell.

A tip of 10-nm radius was introduced on the cathode surface to obtain the field enhancement factor and the enhancement profile. The 10-nm hemispherical tip was integrated to the square face of a pyramid whose size was chosen $4 \times 4 \times 5$ $(\mu\text{m})^3$ in order to be dimensionally close to an actual DFEA tip used in the experiment. As the result of the introduction of the tip (perfect electric conductor BC), the electric field in the immediate neighborhood of the tip is enhanced from otherwise $\sim$ 810 V/m to $\sim$ 55680 V/m, suggesting an enhancement factor $\beta_e \sim 69$ (i.e $\frac{55680}{810}$); see Fig. 6.8. Further refinement of the meshing would improve the resolution around the tip, and hence would give higher enhancement factors; but this would considerably increase the requirements on the computing power and computational time. A challenge in introducing a nano-sized tip in a gun whose size is of several hundreds of centimeters is the mesh adaptation; the volume around the tip requires a much higher mesh resolution than that of the bulk of the gun. Hence in this model, three different sub-domains were created whose mesh element size limits were separately

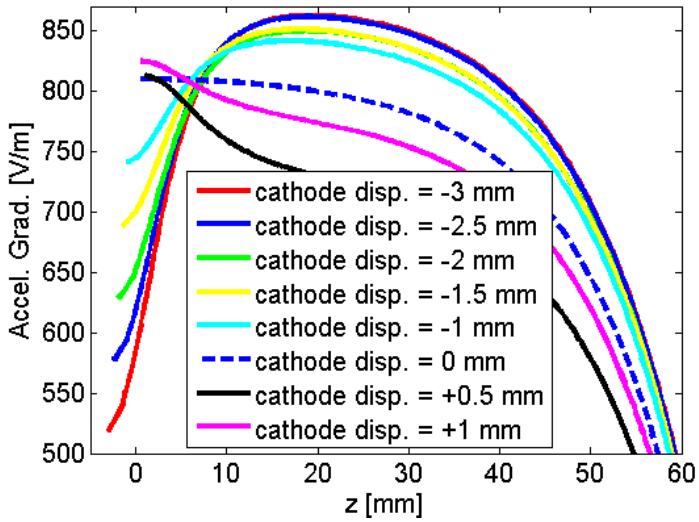

Figure 6.7: The accelerating gradient profiles near the cathode for the cathode displacements considered in Fig. 6.6.

set. At the intersection of these sub-domain surfaces, the default adaptive mesh control was used.

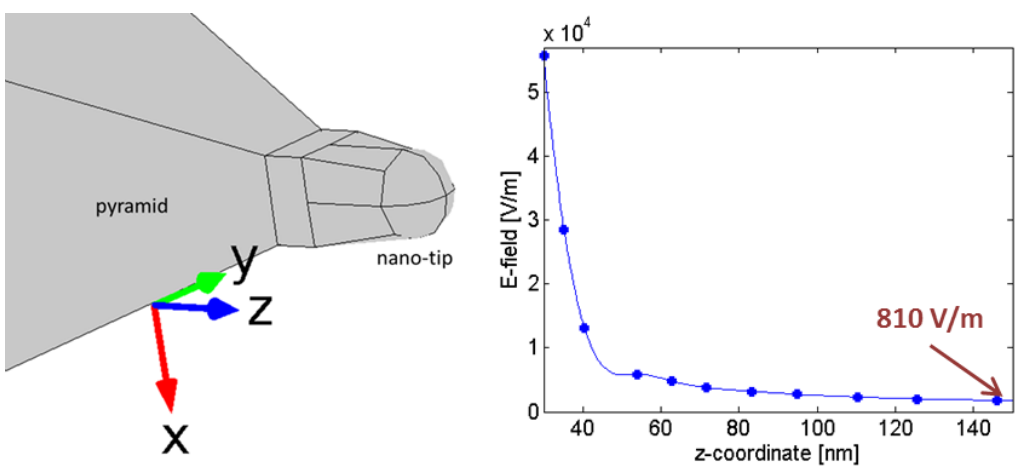

Figure 6.8: The 10-nm radius tip on a pyramid introduced on the cathode surface (left) and the field enhancement profile in the neighborhood of the tip (right).

6.3.1.2 Beam Dynamics Simulations

Numerical simulations using ASTRA (a space charge tracking algorithm), a Fortran based popular charged particle tracking program developed at DESY, Germany, were performed to understand the beam dynamics of an electron beam emitted from a single tip and accelerated by the RF gun. Later, the beam dynamics from an array of field-emitters was studied. In order to obtain the initial charge distribution, the electric field distribution on a 20-nm diameter nanotip, as shown in Fig. 6.9, was obtained from the COMSOL model considered in Fig. 6.2. The data points in Fig. 6.9 are approximately equally spaced.

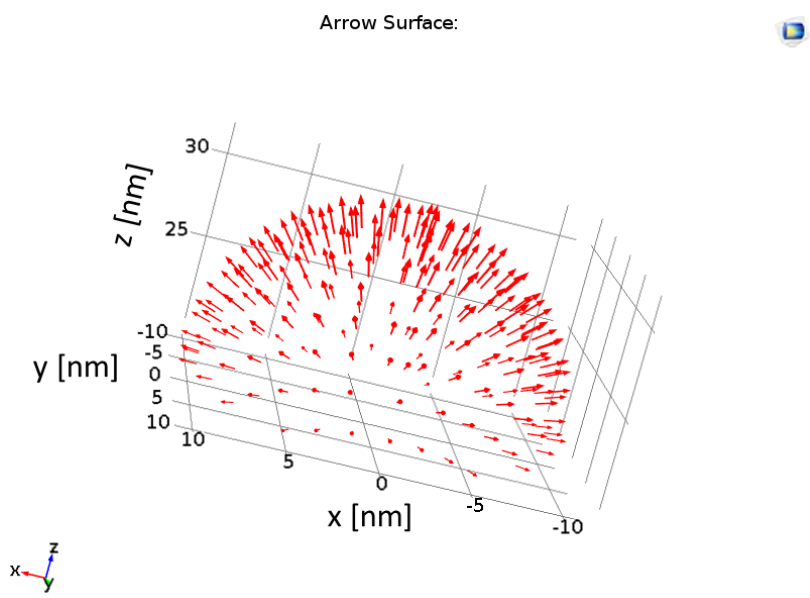

Figure 6.9: The electric field distribution on a 20-nm diameter nanotip for an arbitrary peak electric field. The size and the direction of an arrow represents respectively the magnitude and the direction of the field at the corresponding location. All dimensions are in nm.

The data represented in Fig. 6.9 corresponds to 198 points, while each point has three spatial coordinates (x, y, z) and the respective three electric field components

(E_x, E_y, E_z), where the field magnitude is given as $E_e(x, y, z) = \sqrt{E_x^2 + E_y^2 + E_z^2}$. From this data, an FN distribution of the charge density was created based on the current density given by Eq. 6.3. The absolute value of the actual maximum charge in the initial particle distribution is unimportant, because in ASTRA an arbitrary initial charge distribution can be automatically scaled to a specified total charge. Figure. 6.10 shows a scatter plot of the FN charge density ($\propto j$) distribution on the nanotip, obtained from the data corresponding to Fig. 6.9.

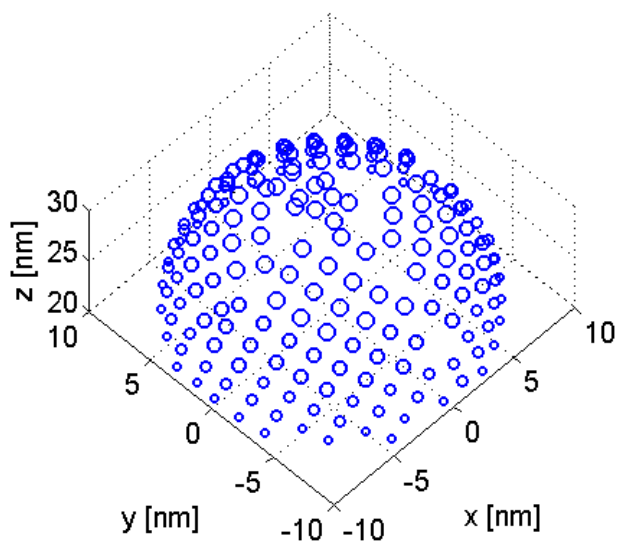

Figure 6.10: A scatter plot of an FN charge density distribution on the nanotip corresponding to the electric field represented Fig. 6.9 for an arbitrary total charge. The size of a marker represents the magnitude of the charge density at the corresponding location.

The cumulative initial charge distribution file for ASTRA needs the following information for each particle: $\{x^{(m)}, y^{(m)}, z^{(m)}, p_x^{(m)}, p_y^{(m)}, p_z^{(m)}, t^{(m)}, Q^{(m)}\}$ where the superscript m represents the particle index, p is the momentum, t is the time of emission and Q is the charge. In the current work, we considered the charge of the particle $Q^{(m)} \propto j^{(m)}$ to mimic an FN charge density distribution from approximately

equally spaced points. An initial momentum correlation of $p^{(m)}_{x,y,z} \propto E^{(m)}_{e\{x,y,z\}}$ was assumed since a particle of index m emitted via FE is initially briefly accelerated by the locally enhanced field $E^{(m)}_e$ leading to an initial momentum ($\propto E^{(m)}_e$), before the acceleration by the macroscopic field happens. It was verified that in the absence of this correlation, the simulations resulted in impractically low emittance values of the beam. A particle at the center of the tip was chosen to be the 'reference' particle which is used by ASTRA to set an RF injection phase that maximizes the reference particle's energy. This is critical for optimized acceleration of the bunch. The reference particle has coordinates $\{x, y, z\} = \{0, 0, 30\}$ nm, $t^{(m)} = 0$, and was assigned the maximum (among all the particles) total momentum $p_{max} \sim 500$ eV/c, a value comparable to that in an earlier work summarized in [71]. The temporal emission profile of the particle distribution was set to be a Gaussian utilizing ASTRA's particle generation program; the Gaussian is a good representation of an FN particle emission distribution generated by a sinusoidal (RF) electric field on the order of 10 MV/m, as shown in Fig. 6.11. The FN current density in the figure was computed using Eqns. 6.3 and 6.4 for the engineering values $E_0 = 15$ MeV, $\beta_e = 100$ and $\phi = 4.9$ eV, and normalizing the peak values of E and j to unity.

The total charge of the bunch was estimated from the experimental value. From Fig. 6.21, we see the maximum current from $\sim 10^6$ tips is $I_{max} \sim 15$ mA when operated at the RF frequency $f_0 = 1.3$ GHz and an accelerating gradient $E_0 \sim 25$ MV/m. This corresponds to a charge per bunch per RF period $Q \sim \frac{I_{max}}{10^6 f_0} = 1.15 \times 10^{-17}$ C (1.15×10^{-8} nC), which corresponds to the charge of about 72 electrons emitted per tip in one RF cycle. The rms transverse spot size of the tip was taken to be $\sigma_x = \sigma_y = \mathrm{XY_{rms}} = 20/4 = 5$ nm (uniformly spaced cylindrical particle distribution). The rms duration of the emission was taken as $T_{rms} = 64$ ps, which corresponds to $\frac{1}{6}^{\mathrm{th}}$ of the full Gaussian emission time of 384 ps ($\approx 0.5 f_0^{-1}$).

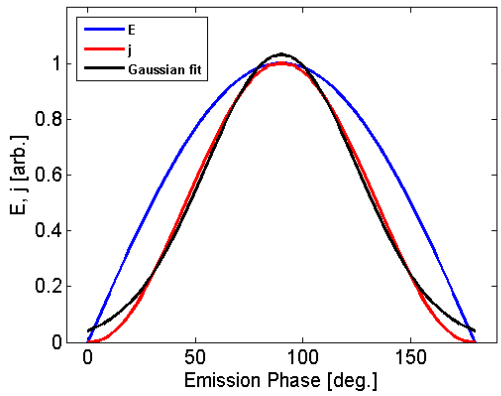

Figure 6.11: FN current density (red curve) corresponding to a sinusoidal (temporal) macroscopic electric field (blue curve). The black curve is a Gaussian fit to the FN current density.

With the initial particle distribution and the emission parameters described above set, the simulations were executed while including the space charge forces, and the solenoid (see Fig. 2.7) and RF fields ($E_0 = 25$ MeV) corresponding to the experimental values. Figure. 6.12 shows the evolution of the transverse and longitudinal beam emittance and size along the beamline computed by ASTRA. Figure 6.13 shows the transverse (x) phase space and the corresponding projection of the beam at $z = 1$ m.

It can be noticed that the transverse emittance for a single tip is on the order of 5 nm, which is expected due to very low charge per bunch. The red and blue curves in Fig. 6.12 are expected to overlap. However, due to the low number of particles (198), there are statistical errors that contribute to the $x - y$ asymmetry. Nevertheless, in the results, ϵ_x and σ_x values are observed to be close to ϵ_y and σ_y values respectively. The sharp peaks in the ϵ_z and σ_z curves occur due to loss of low energy particles in the 'tail' of the bunch around $z = 0.6$ m. A simulation corresponding to the parameters considered in Fig. 6.12 but excluding the space

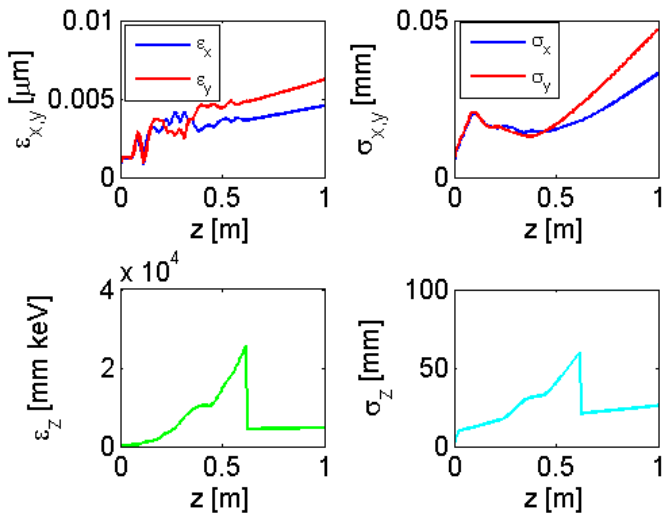

Figure 6.12: Evolution of transverse (x, y) and longitudinal (z) normalized emittance (ϵ) and rms beam size (σ) of the beam emitted from a single nanotip, along the beamline.

charge forces resulted in noticeably same results, indicating that the beam from a single tip is not space charge dominated, as expected due to low number of particles.

Figure 6.14 shows ASTRA results of the longitudinal phase space (LPS) and the corresponding projections of the bunch. It can be noticed that more particles are concentrated towards the head of the bunch ($\Delta z > 0$) in the energy distribution; this is because the acceleration is optimized for majority of the particles emitted

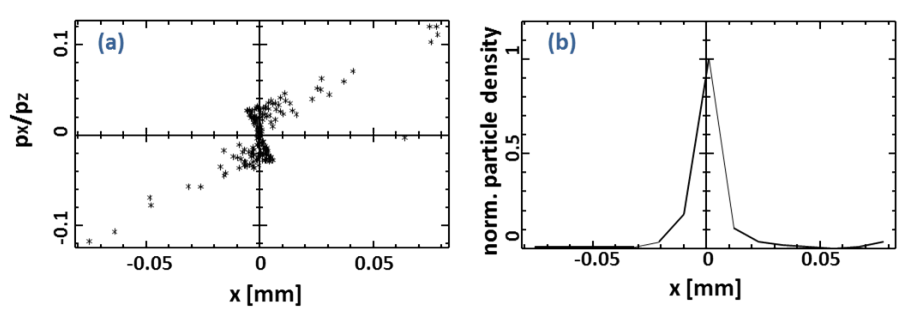

Figure 6.13: Transverse (x) phase space (a) and the corresponding projection (b) of the beam emitted from a single nanotip at $z = 1$ m.

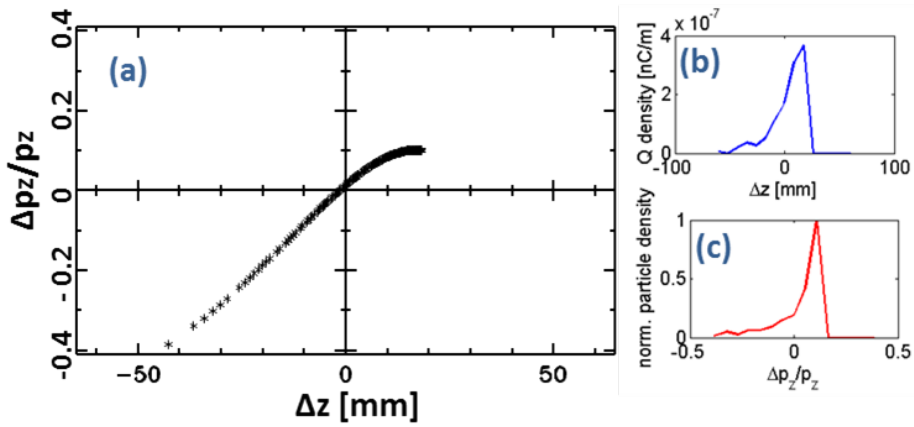

Figure 6.14: Longitudinal phase space (a) distribution of the bunch emitted by a single nanotip at $z = 1$ m and the corresponding projections [(b) and (c)].

from the area around the reference particle, which has high charge density. The minority of the particles that are emitted later in the RF period lag behind and gain lesser energy. The mean energy of the beam was computed to be ≈ 2.5 MeV.

Emission from an array: an array of tips was created by copying the distribution of a single tip at the nodes of 200 rows and 200 columns with a 10-μm pitch (inter-row and inter-column separation), containing a total of 40,000 tips. In order to reduce the total number of particles in the array to conserve computational time and memory, the number of particles on one tip was reduced from 198 to 51. The charge per particle was increased so that the charge per bunch was the same as before; this was done by specifying the total bunch charge in ASTRA as mentioned before. The total number of particles in the 40,000-tip array is therefore $40,000 \times 51 = 2.04 \times 10^6$. Figure 6.15 shows the new reduced particle distribution of a single tip with 51 particles. Figure 6.16 shows an array of 25 tips as an example of a subset of the 200×200 array.

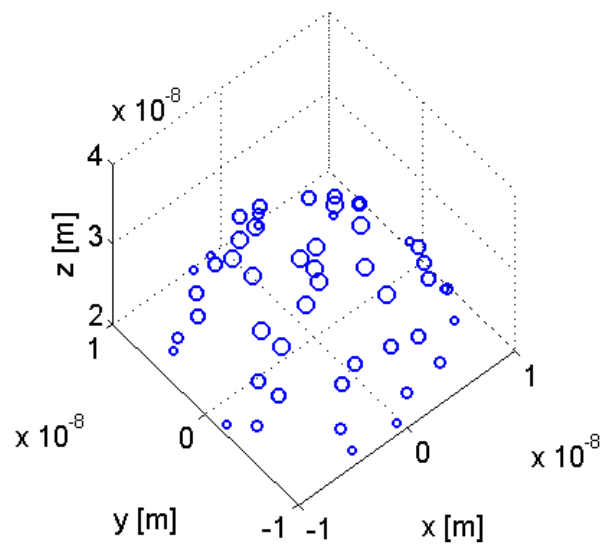

Figure 6.15: A scatter plot of the particle distribution on a nanotip with the number of particles reduced to 51, from previously 198. The size of a marker represents the magnitude of the charge density at the corresponding location.

The total size of the array is therefore 2-mm×2-mm (square), which corresponds to $\mathrm{XY_{rms}} = 2/\sqrt{12} = 0.577$ mm (uniform square distribution). The total charge emitted from the array is calculated as $Q = 40,000 \times (1.15 \times 10^{-8}) = 4.6 \times 10^{-4}$ nC. With these Q and $\mathrm{XY_{rms}}$ values, the simulations were executed for the 40,000-tip array particle distribution including the solenoid and the RF fields as before, but excluding the space charge forces to conserve computational time. An earlier study done on the 25-tip example array distribution considered in Fig. 6.16 concluded that space charge forces have no noticeable effect on the transverse and longitudinal beam dynamics.

Figure 6.17 shows the evolution of the transverse and longitudinal emittance and size of the beam emitted from the array, along the beamline. It should be noted that the x and y characteristics are identical in this case due to large number of particles involved, eliminating statistical errors. The LPS distribution for a beam with mil-

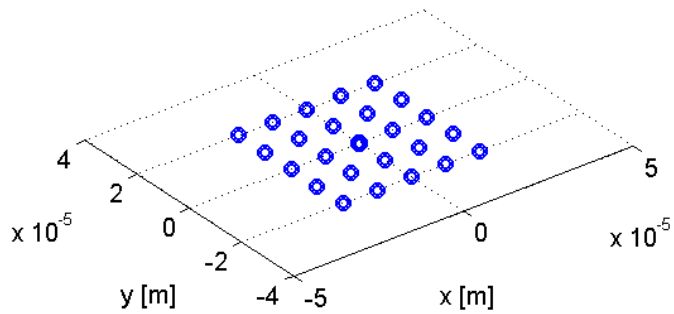

Figure 6.16: An array of 25 tips arranged in 5 rows and 5 columns. Each tip has a 3D particle distribution shown in Fig. 6.15.

lions of particles like the current case could not be computed due to computational limitations. The transverse (x) phase space and the corresponding projection of a beam emitted from a 3600-tip array is shown in Fig. 6.18.

Figure 6.19 compares the transverse parameters of a beam emitted from arrays of various sizes. The parameters $\epsilon_z = 1350$ mm keV, $\sigma_z = 20$ mm, energy spread $\Delta E = 450$ keV and mean energy $E = 2.51$ MeV did not change with the size of the array as expected.

6.3.2 Experiment

The DFEA cathode was inserted inside the gun using the load-lock mechanism. After inserting the cathode holder in the gun, its position was adjusted (longitudinally) to ensure the gun's resonant frequency remained at 1.3 GHz $\pm$100 KHz, as monitored with a network analyzer.

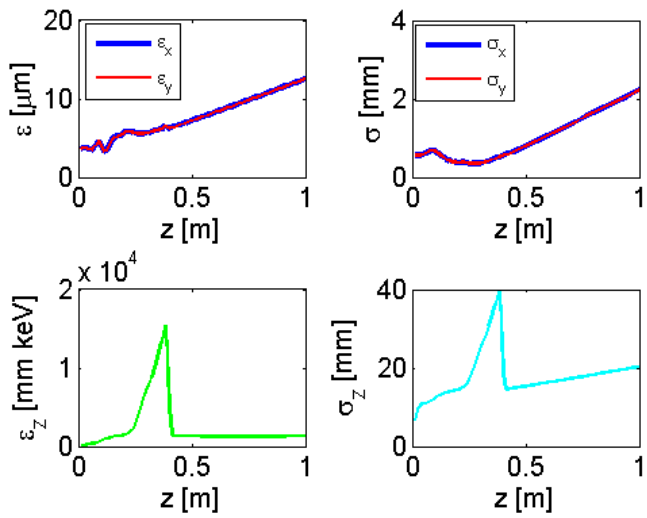

Figure 6.17: Evolution of the transverse and longitudinal normalized emittance (ϵ) and the rms beam size (σ) of the beam emitted from a 40,000-tip array, along the beamline.

The Cu-Be spring that surrounds the cathode plug was found to be a source of spurious but negligible field emission current. A series of measurements were made to characterize the spurious (background) field emission from the Cu-Be spring. For these studies, a standard Cs_2Te photocathode was initially used to quantify the spurious field emission current as measured by the Farday cup (FC). The DFEA was then inserted and its current was measured for several forward power levels. As

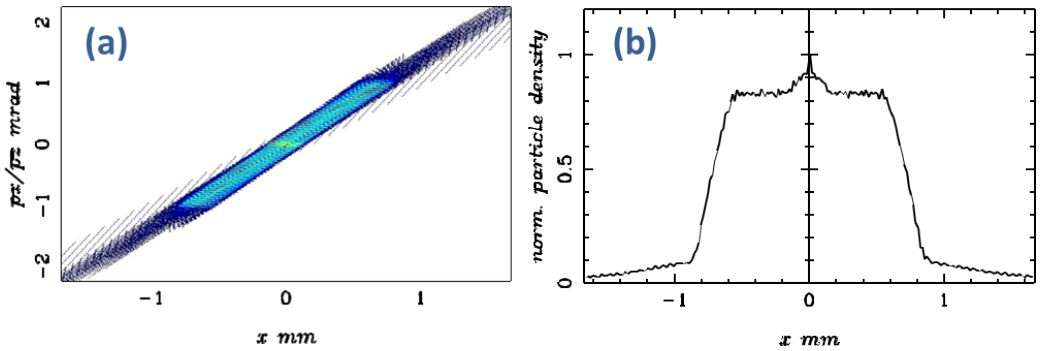

Figure 6.18: Transverse (x) phase space (a) and the corresponding projection (b) at $z = 1$ m, of the beam emitted from a a 3600-tip array.

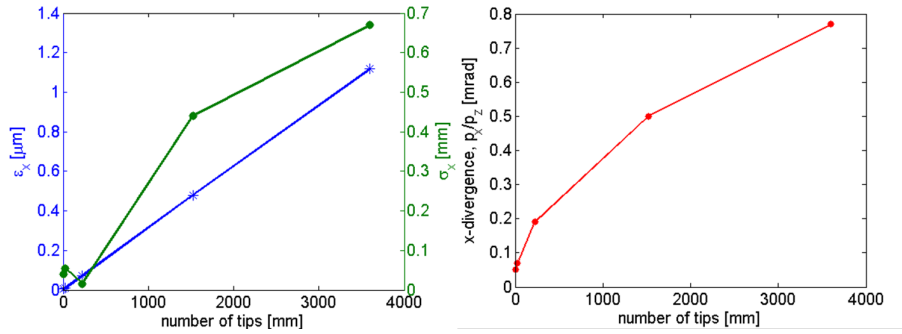

Figure 6.19: Evolution of ϵ_x, σ_x and $\sigma_x^{'}$ with the number of tips in the array.

shown in Fig. 6.20, the spurious field-emitted current from the Cs_2Te/Cu-Be spring was negligible ($I \leq 50$ μA) when compared with the current from the DFEA ($>$ 15 mA). The current waveform's slow rising time for $t \in [-10, 5]$ μs is consistent with the e-fold filling time of the RF gun $\tau = Q_\eta/2\pi f \simeq 3$ μs [72], where Q_η is the Q-factor of the gun (see Eq. 6.7) and $f = 1.3$ GHz.

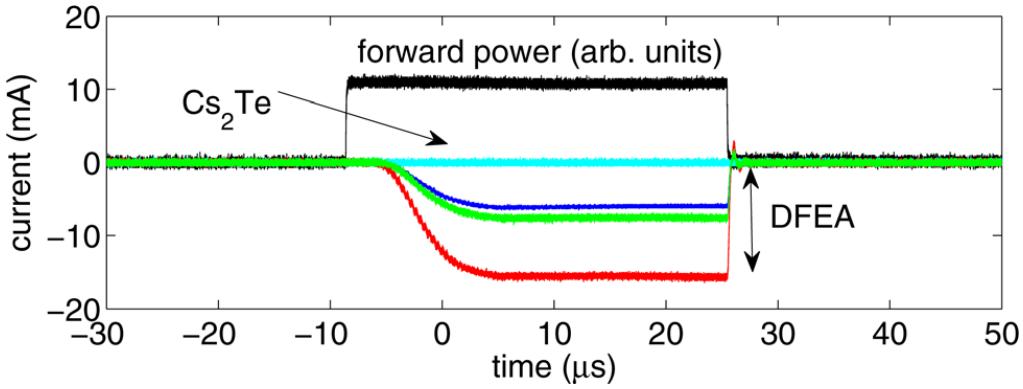

Figure 6.20: Current traces recorded with the DFEA cathode for 1.2 (blue), 1.3 (green), and 1.5 MW (red) forward power [14]. The turquoise trace shows the field-emitted 'background' current observed from the nominal Cs_2Te photocathode when inserted in the RF gun.

6.3.2.1 FN Characteristics

FN characteristics recorded over several days of operations and for different cases considered in this experiment are shown in Fig. 6.21. The (logarithmic) curves are characterized by high field slopes $\nu \equiv b(\phi)/\beta_e$ (see Eq. 6.3) obtained from the linear fits in the region $E_0^{-1} \leq 0.06$ (MV/m)$^{-1}$. Two cases of cathode positions, *nominal* and *retracted*, corresponding respectively to the cases when the cathode is flush with, and retraced $\sim$ 2 mm from the gun's backplane are considered. The retracted case gives lower axial field on the cathode edges as $E_z(r,z) \simeq E_z(0,z) - \frac{r^2}{2}(d^2E_z(0,z)/dz^2)$ [14]. Also the peak field at the cathode center is reduced by $\sim$ 22% (from Fig. 6.6). For the nominal case [Fig. 6.21(a)–6.21(c), 6.21(e), and 6.21(f) traces], the cathode performance and characteristic curves are very similar when the solenoids are turned off [plots (a) and (e)] or turned on to focus the beam at X1 [plots (b) and (f)]. Likewise, the measured slope with the solenoid off measured after 59 days [plot (c)] agrees within 10% with the initial slope [plot (a)]. The slope measured for the retracted position is 25% higher than for the nominal case. For all cases, the start-up macroscopic field was $E_0 \simeq 18$ MV/m.

6.3.2.2 Transverse Beam Density and Current Stability

Figure 6.22 shows the transverse beam density of the train of bunches emitted by the DFEA cathode, at position X3 with solenoids OFF [(a)] and ON [(b)] operated at field gradients 23.5 MV/m and 31 MV/m respectively.

The vacuum pressure was observed to be stable without any appreciable degradation ($\leq 1.2\times10^{-9}$ Torr) during the experiment. The current was recorded for a

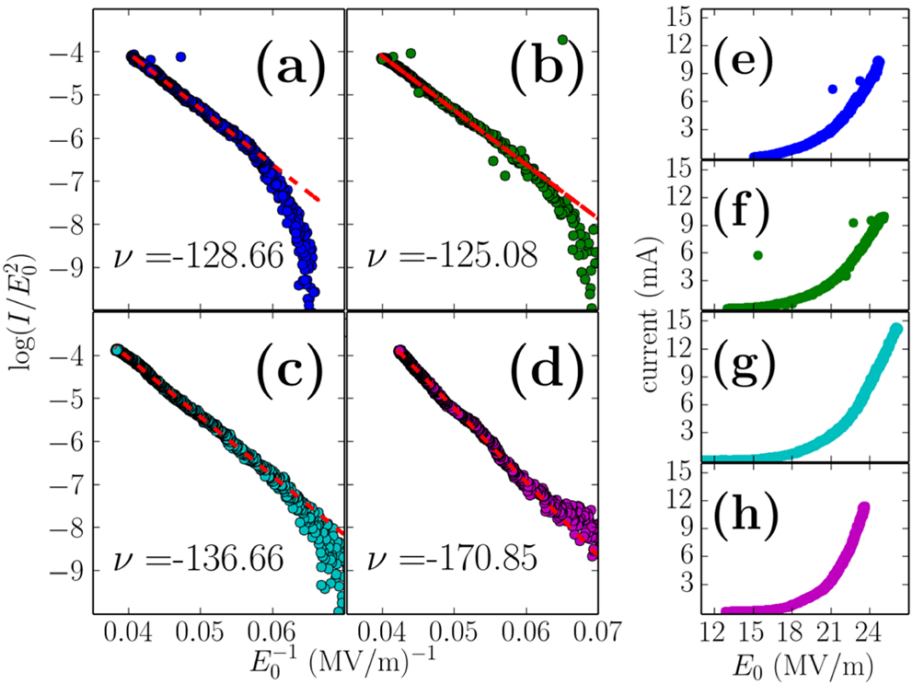

Figure 6.21: FN plots [(a)–(d)] and the corresponding characteristic curves [(e)–(g)] for the nominal [(a)–(c)] and retracted[(d)] cathode positions [14]. The traces [(a) and (e)] and [(b) and(f)] were acquired with the solenoids off and on respectively, and, traces [(c) and (f)] were taken for the same condition as [(a) and (e)] 59 days later. The dashed line in (a)–(d) is the result of the linear regression.

long period of up to 2 hours as shown in Fig. 6.23. An apparent current drift that was observed, was tracked back to the klystron power drifting in time. Accounting for the E-field drift by computing an instantaneous FN slope as $\mu \equiv E_0 \log(\frac{I}{E_0^2})$ (see Eq. 6.4) indicates that the emission was stable with typical relative rms variation $\left\langle [(\delta\mu)/\mu]^2 \right\rangle^{1/2} \simeq 0.37\%$ [14]. In practice, correlated changes due to klystron power drifts can be compensated using a feedback system, which was not used at the time of the experiment because of a gun temperature controller malfunction.

In summary, we demonstrated the operation of a DFEA cathode in an RF source nominally designed for photocathodes. It was also demonstrated that the DFEA cathode is robust under high field gradients providing a stable current. These results

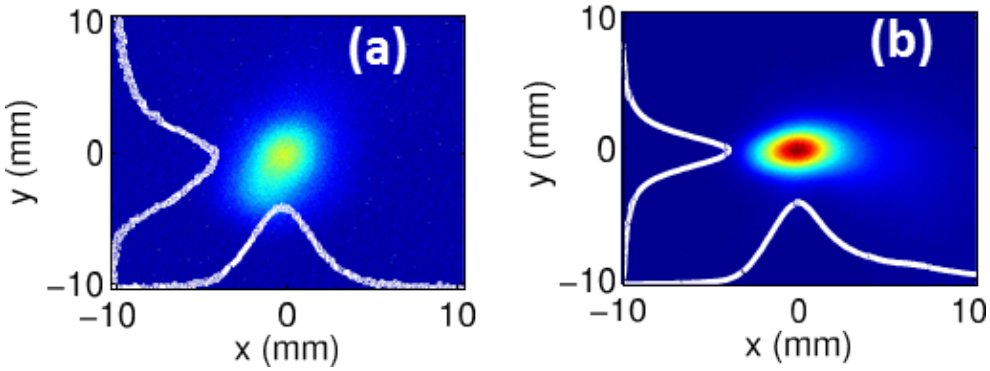

Figure 6.22: The measured transverse density of the beam at X3 with solenoids off (a) and focused with solenoids turned on (b) corresponding to the accelerating gradients of 23.5 MV/m and 31 MV/m respectively [14]

represent a significant step toward the realization of laser-free compact light sources for industrial, medical, and defense applications.

6.4 Carbon Nanotube Cathode in RF gun

A second type of cathode, carbon nanotube (CNT), was also tested in HBESL's L-band RF gun. Unlike the DFEA cathode which is an array of diamond FEs, the CNT cathode(s) used for the current experiment is an agglomeration of randomly oriented multi-walled carbon nanotubes (MWCNTs) having sharp tips of about a few nanometer radii. Such a nanotube offers an enhancement factor on the order of $\beta_e \sim 100 - 1000$, much higher than that of a DFEA tip. Two CNT cathodes were tested in the current experiment viz. the 'large' cathode and the 'small' cathode. The large cathode has a molybdenum substrate and consists of a 15-mm diameter CNT emitter area, while the small cathode has stainless steel substrate and consists of a 1.5-mm diameter emitter area [see Fig. 6.24 (b) and (c)].

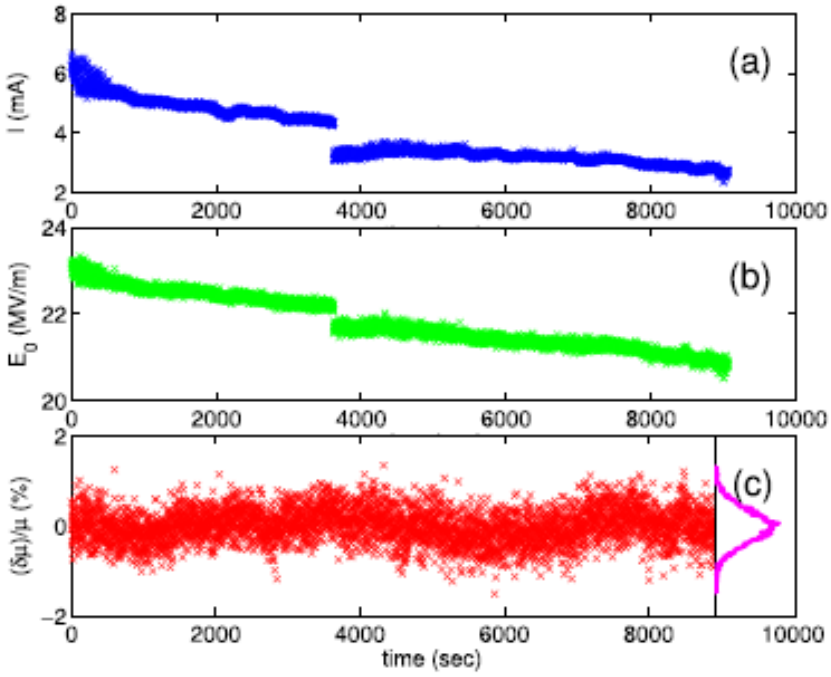

Figure 6.23: Longterm current stability studies for two cases of electric field values (initial setup points $E_0 \simeq 23$ MV/m for $0 \leq t < 3800$ s and $E_0 \leq 21.7$ MV/m for $3800 \leq t < 9000$ s). Evolution of the beam current (a), macroscopic field E_0 (b), and relative change in the FN slope μ (c). A time-integrated histogram of $\delta\mu/\mu$ is shown in (c) [14].

The CNT cathodes were synthesized using an electrophoretic deposition (EPD) process, which is a rapid and economical way of producing CNTs with varying properties in large numbers [73]. An EPD nano-deposition process consists of charged nano-particles suspended in a suitable solvent, which are deposited on to an electrode. The large cathode was synthesized at UCLA by pursuing the following procedure. A solution of 25 mL of methanol (CH_3OH) and 8.5 mg of a commercially bought CNT powder was sonicated for 15 minutes in a glass beaker. The CNT powder consisted of various allotropes of carbon including graphite, amorphous carbon, buckyballs and nanotubes. In order to make the nano-particles charged, 0.25 mg of Magnesium chloride ($MgCl_2$) was added to the suspension and the solution was

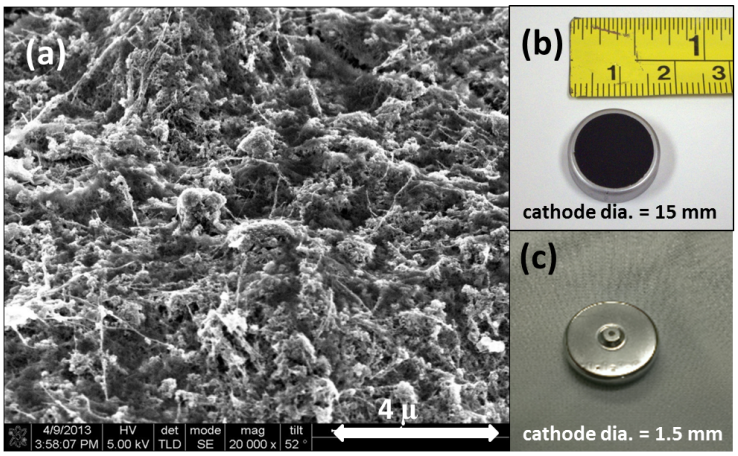

Figure 6.24: An SEM image of the large CNT cathode with a magnification of 20k showing CNTs and other structures (a), a picture of the large CNT cathode (b), and a picture of the small CNT cathode (c). (Photograph courtesy of UCLA and RadiaBeam Technologies, LLC.)

sonicated for an additional 5 minutes. The Mg^+ ions adhere to the carbon nanoparticles, thus making them positively charged. Immediately after the solution was sonicated, the solution was transfered into a glass beaker which had a stainless steel lining at the bottom that would act as the positive electrode. A Molybdenum (Mo) cathode substrate that mounts onto HBESL's cathode plug similar to the one shown in Fig. 6.4, which would act as the negative electrode, was then slowly lowered into the beaker with the Mo substrate facing the stainless steel sheet. At a gap of ~ 7 mm between the two electrodes, a DC voltage of 25 V was applied to the electrodes via electrical wires. After a deposition time of 30 minutes, the Mo substrate was then rinsed with isopropyl alcohol (C_3H_7OH) to remove $MgCl_2$ residue and any loose CNTs that didn't properly adhere to the substrate.

A scanning electron microscope (SEM) image with 20k magnification of the large CNT cathode is shown in Fig. 6.24 (a). The small cathode was also synthesized using an EPD process by a commercial industry but the process-specifications are unavailable. The small cathode has a different geometry [see Fig. 6.24 (c)] from the

large cathode, as a result of being synthesized at a different facility. A bossed structure of a size of approximately 2-mm diameter and 1.5-mm outward protuberance can be seen on the small cathode in Fig. 6.24 (c) [compare with (b)].

6.4.1 Numerical Simulations

6.4.1.1 Electromagnetic Modeling

FEM simulations using COMSOL were performed to support our studies. Geometrical differences between two cathodes could have compelling effects on the RF system, e.g, on the RF power sustained inside a resonating cavity and the maximum electric field that can be achieved. We are particularly interested in learning about how the quality factor, a.k.a the Q-factor, of HBESL's gun is effected by the bossed structure of the small cathode. The Q-factor Q_η of a resonator is a dimensionless quantity that is a measure of the ratio of the sustained power to the dissipated power in the resonator at a given frequency of resonance, and is defined as

$$Q_\eta(f) = 2\pi f \times \frac{\mathcal{E}_s}{P_d} \tag{6.7}$$

where f [Hz] is the resonating frequency of interest, $\mathcal{E}_s$ is the time-averaged stored energy [J] inside the RF resonator at frequency f, and P_d is the dissipated power [W] at frequency f. In the current section, we first compute the Q-factors of HBESL's RF gun for the zero- and π-modes for the geometries of the two cathodes considered in the experiment using COMSOL. Later on we obtain the modified axial electric field inside the gun for the case of the small CNT cathode.

The COMSOL model of HBESL gun described in Section 6.3.1 was utilized and extended for the current study. Here, the gun's geometric model was modeled with the parameter assignments specified in Table 6.1 except for the perfect metallic conductor BC, which was changed to the finite conductivity metallic conductor of copper. By doing so, an estimation of the Q-factor of HBESL's RF gun can be made since it is made of copper. The conductivity of copper was taken to be 5.96×10^7 S/m (input). In COMSOL, after executing the simulation computation, the time-averaged energy density $\mathcal{E}_s$ [W/m^3] and the surface loss density P_d [W/m^2] are written to file. Thus, the Q-factor can be computed by performing the following numerical integration of

$$Q_\eta(f) = 2\pi \times f \times \frac{\int_V \mathcal{E}_s(V)dV}{\int_S P_d(S)dS} \tag{6.8}$$

where the volume V corresponds to the entire volume of the gun and the surface S corresponds to all the outer surfaces (excluding the internal slice surfaces) of the gun's geometry shown in Fig. 6.5; both V and S are user-specified via COMSOL's graphic user interface (GUI) while Eq. 6.8 is user-specified as a definition that is to be numerically computed.

The estimation of the Q-factor for the case of small cathode was done in a similar way described above, but the geometry of the gun was modified accordingly by introducing a bossed structure as shown in Fig. 6.25. The results of the computed Q-factors that are summerized in Table 6.2 reveal that the geometry of the small cathode does not make any significant difference from the standpoint of the RF system, since the Q-factors for both gun (cathode) geometries are within $\sim 0.15\%$. The Q-factor computed for the case of nominal geometry (large cathode) agrees with the previously performed experimental Q-factor calculations. Fig 6.26 compares the

surface resistive loses showing only little difference between the two geometrical cases of the gun.

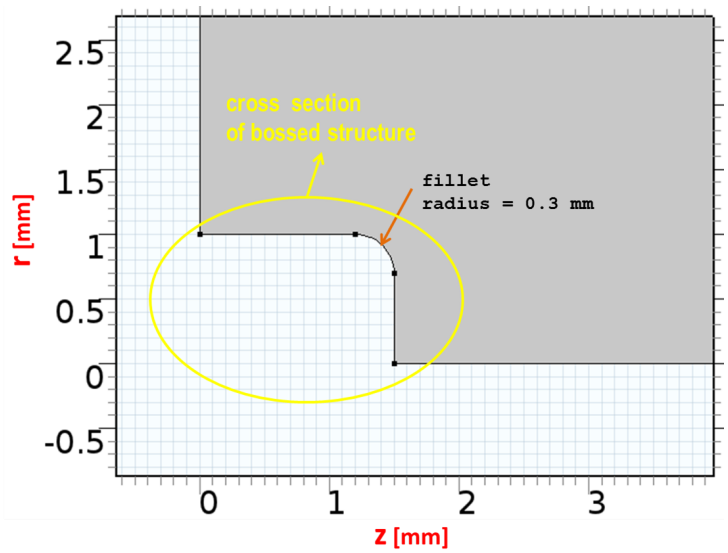

Figure 6.25: The cross-section of the (quarter) gun near the cathode region for the case of small cathode. The coordinate z corresponds to the longitudinal axis of the gun and r corresponds to the radial direction.

Figure 6.27 (left) shows that an additional field enhancement of ~ 2.22 ($\equiv \frac{1800}{810}$) occurs due to the bossed structure at the center of the small cathode. On the right of the figure, the longitudinal electric field is shown as a function of the radius of the gun, which shows that the field near the fillet of the bossed structure is greater than that of the center. Such a field distribution leads to higher current density from the small cathode around its edges than the center, contrary to a nominal flat cathode where the current density is maximum at the center.

In order to supplement and validate the numerical results on Q-factors, a set of network analyzer and spectrum analyzer measurements were performed on the RF gun for the two cases of nominal and small cathode geometries. A network analyzer measures the tune, or the resonant frequencies of a cavity in a given frequency range by sending a test power to the cavity. A spectrum analyzer measures the frequencies

Table 6.2: Numerical results of computations of Q-factors of HBESL's RF gun for the cases of large and small cathodes.

Case 1: large cathode (nominal)		
Mode	Eigenfrequency	Q-factor
π	1.29866e9+i27524.53768	23590.92537
zero	1.29597e9+i29099.37368	22267.94858
Case 2: small cathode		
Mode	Eigenfrequency	Q-factor
π	1.29865e9+i27483.2008	23626.16946
zero	1.29594e9+i29140.1135	22236.44309

sustained inside a cavity during the designed operation of the cavity i.e when the cavity is powered by the klystron.

A network analyzer of n-ports is a device that can send test (power) signals from any or all of its n-ports and receive and analyze the response signal from the device being tested to characterize the device. During the network analyzer measurements, the RF gun was disconnected from the klystron system and connected to the analyzer using a toggle switch. The network analyzer measurements considered here correspond to an s-parameter measurements of $S_{1,2}$ where the parameter $S_{m,n};\ [m,n] \in [1,2]$ (for a 2-port system) is defined here as $S_{12} \equiv P_m/P_n$, where P_m and P_n represent respectively the power sustained inside the RF gun near port m and the power supplied to the RF gun via port n. The antennas located inside and at each of the two port couplers of the RF gun measure the corresponding powers. In our case, there is only one antenna inside the RF gun to measure the power sustained in the gun.

The spectrum analyzer measurements were performed when the RF gun was being powered by the klystron during normal operation. In such a measurement,

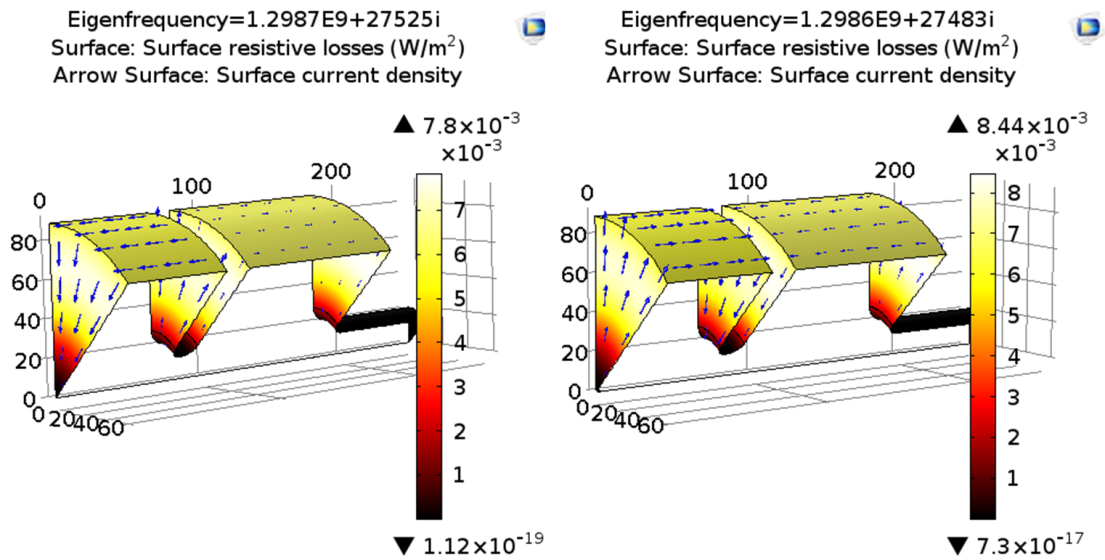

Figure 6.26: Comparison of surface resistive loses for the two cases of the large (left) and small cathodes (right) in RF gun's π-mode. Note: the maximum electric field in the cavity in the model is arbitrarily scaled to $\sim$ 810 V/m.

the antenna inside the gun supplies the spectrum analyzer with the response signal (electric field) whose frequency spectrum is obtained by the analyzer. The spectrum and network analyzer measurements compared in Fig. 6.28 for the two cases of nominal and small cathodes show no notable differences in the resonant frequencies of the gun, in agreement with numerical results presented in Table 6.2. The inter-modal frequency seperation between the zero- and π-modes in Fig. 6.28 is $\sim$ 2.52 MHz, in agreement with the simulations (2.69 MHz).

6.4.1.2 Beam Dynamics Simulations

Numerical simulations using ASTRA were performed to study the beam dynamics of the beam generated from a CNT cathode. Because the individual CNT emitters have a transverse size on the order of a few nm, the cathode was treated as

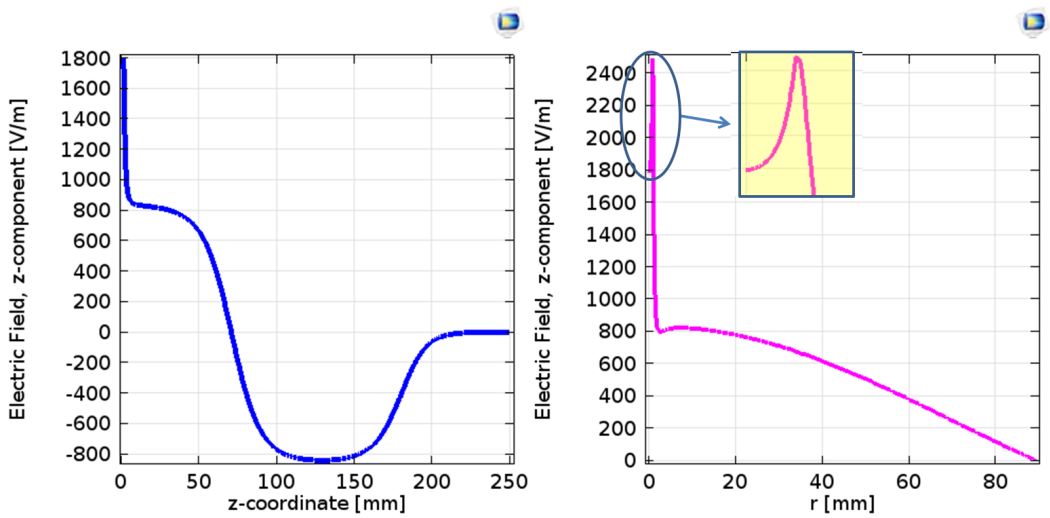

Figure 6.27: Longitudinal electric field along the axis (z) (left) and along the radial coordinate (r) of the gun for the case of small cathode. The inset corresponds to the region around the fillet of the bossed structure.

a homogeneous emission area, instead of a discretized array distribution considered in Section 6.3.1.2. Such a treatment is equivalent to a photoemission model where the beam is emitted by a laser pulse of Gaussian temporal duration estimated from the FN equation. An initial particle distribution of 100,000 particles was generated using ASTRA's particle distribution generator program.

The initial particle distribution was scaled to $T_{rms} = 64$ ps and $\mathrm{XY_{rms}} = 0.375$ mm (a cylindrical uniform distribution of 1.5-mm diameter) in ASTRA, and the corresponding simulations were executed with the space charge forces, solenoid and RF fields included. Figure 6.29 shows the transverse (x, y) and longitudinal (z) normalized emittance ϵ and beam size σ along the beamline. Figure 6.30 shows the transverse (x) phase space at $z = 1$ m. Figure 6.31 shows the longitudinal phase space distribution. The transverse characteristics of the beam are comparable to that of a photo-emitted beam. However, the longitudinal characteristics (energy

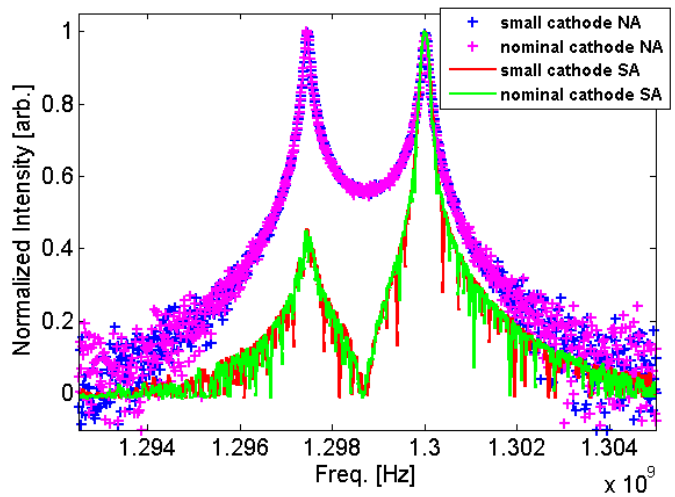

Figure 6.28: Comparison of spectrum and network analyzer measurements of HBESL's RF gun for the cases of small and nominal (flat) cathodes. NA stands for network analyzer and SA stands for spectrum analyzer. The peaks correspond to the zero- (left) and the π-mode (right) respectively.

spread and bunch length) are much larger when compared to photoemission, which arises from the long emission time corresponding to the RF pulse.

6.4.2 Experiment

6.4.2.1 FN Characteristics

The FN characteristics were studied for the large and the small cathodes. In each case, the cathode of interest was mounted on a standard HBESL cathode plug, inserted into the gun using the load-lock mechanism and then the gun was tuned for 1.3 GHz using a network analyzer. First, the emitted current as a function of applied macroscopic field was obtained for the large cathode for two cases of solenoid lenses turned on and off. Figure 6.32 on the left shows the expected exponential-like dependence of $\bar{I}$ on E_0 (see Eqns. 6.4 and 6.5) for the two cases and the corresponding

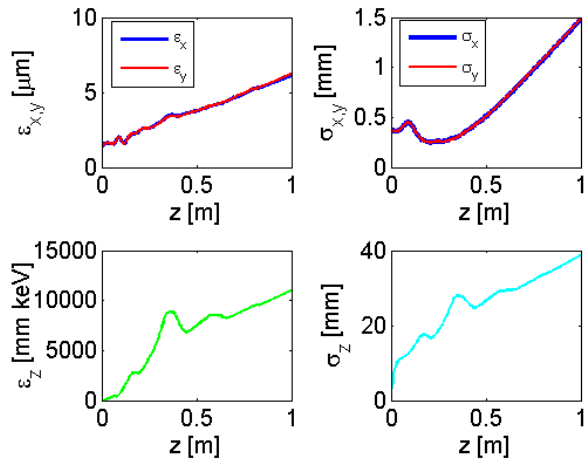

Figure 6.29: Evolution of transverse (x, y) and longitudinal (z) normalized emittance (ϵ) and rms beam size (σ) of the beam emitted from a CNT cathode, along the beamline.

FN plots are shown on the right. For the case of solenoid lenses on, the three lenses were maintained at same magnetic field strength in order to insure a zero-magnetic field at the cathode surface; this lead to only a $\sim$ 10% relative variation in the produced beam current, confirming that only a small fraction of the beam was lost before being captured by the FC.

Similarly, $\bar{I}$–E_0 curves and the corresponding FN curves were obtained for the small cathode as shown in Fig. 6.33. The blue and red plots in the figure corre-

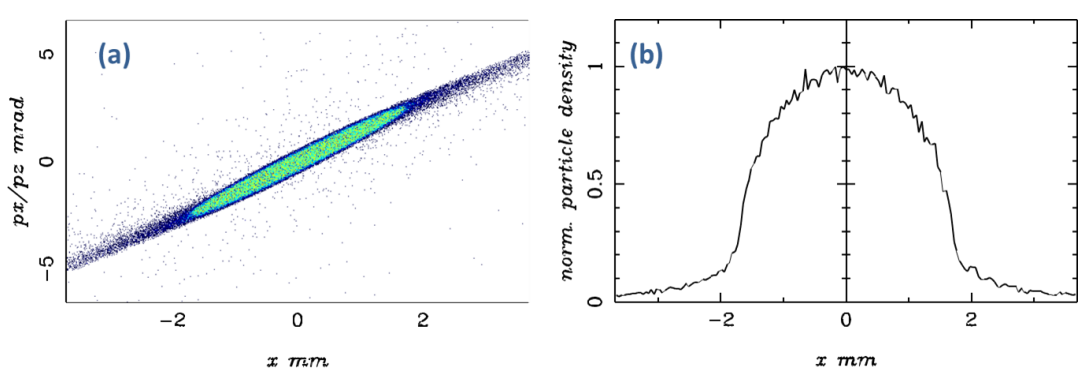

Figure 6.30: Transverse (x) phase space (a) and the corresponding projection (b) at $z = 1$ m for the CNT cathode.

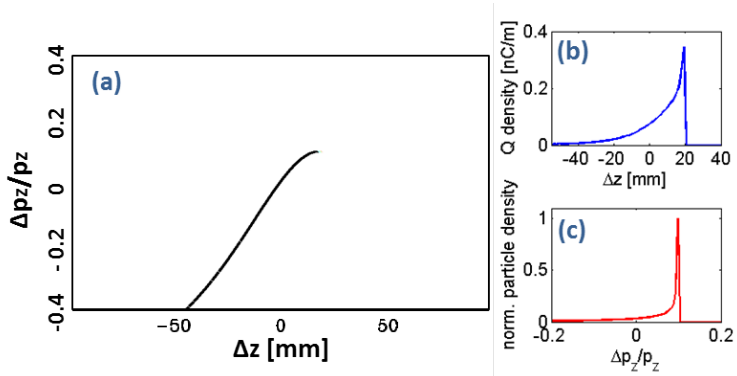

Figure 6.31: Longitudinal phase space distribution (a) of the bunch emitted from a CNT cathode, at $z = 1$ m, and the corresponding projections [(b) and (c)].

spond to the data taken just after the small cathode was installed and 2 weeks later respectively. From Eq. 6.5 we get $\log(\bar{I}E_0^{-2.5}) = \left(\frac{b}{\beta_e}\right)\frac{1}{E_0} + \log\left(\frac{\mathcal{A}a\beta_e^{2.5}}{\sqrt{2\pi}}\right)$. Hence β_e can be experimentally computed from the slope of the FN curve $\frac{b}{\beta}$, and the effective emission area $\mathcal{A}$ can be computed from the intercept $\log\left(\frac{\mathcal{A}a\beta_e^{2.5}}{\sqrt{2\pi}}\right)$ when a value for ϕ is assumed. From the linear fit equations shown in the FN plots in Figs. 6.32 and 6.33, the corresponding β_e factors and effective emission areas were computed and are shown in Table 6.3. It can be noted that the enhancement factors for the large and small cathodes are qualitatively similar and independent of the applied magnetic field. The estimated effective emission area $\mathcal{A}$ is much smaller than expected for the small cathode. Assuming the same CNT density for both cathodes, we would anticipate the effective emission area associated with the small cathode would be $(1.5/15)^2 = 10^{-2}$, but a factor of $\sim [10^{-9} - 10^{-8}]$ was observed. This discrepancy can be attributed to the damage underwent by the small cathode by an observed multipacting due to favorable secondary emission yield from the stainless steel substrate. Upon removal, some gray spots were observed on the small cathode CNT area accompanied by erosion in some substrate sites citing damage as a result of strong multipacting. The small cathode also consistently degraded with time

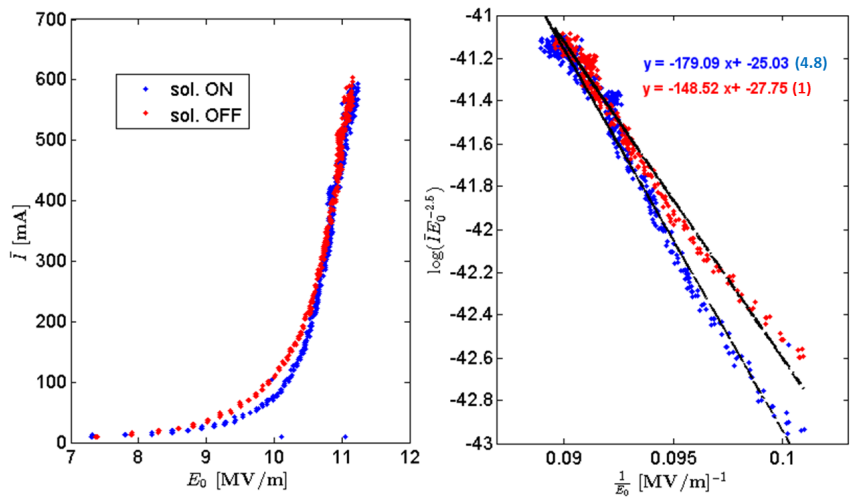

Figure 6.32: Measured average current as a function of applied macroscopic field (left) and the corresponding FN plots (right) for the large cathode. The data 'sol. ON/OFF' correspond to the cases of solenoid lenses turned on and off respectively. The black lines are the linear fits and the corresponding equations are displayed with the the norm of fit residuals shown in the brackets.

while being operated at high field values. The large cathode did not show any performance degradation despite being exposed to atmosphere for $\sim$ 4 weeks between two subsequent tests.

6.4.2.2 Beam Bunching

The temporal structure of the beam emitted from the large cathode was studied by detecting the transient voltage induced by the bunch train as detected by an electromagnetic pick-up located $\approx$ 30 cm from the cathode. The cumulative voltage signal $V(t)$ in time t corresponding to the bunch train can be approximated as

$$V(t) = \Lambda(t) \sum_{n=1}^{N} S(t + n\delta t) \tag{6.9}$$

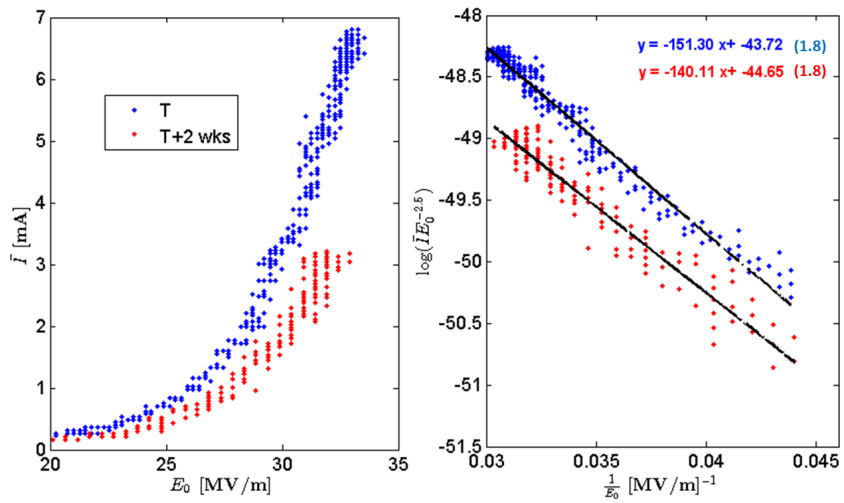

Figure 6.33: Measured average current as a function of applied macroscopic field (left) and the corresponding FN plots (right) for the small cathode. The 'T' corresponds to data taken just after the installation of the cathode while 'T+2 wks' corresponds to the data taken 2 weeks later. The black lines are the linear fits and the corresponding equations are displayed with the norm of the fit residuals shown in the brackets.

where $\Lambda(t)$ is the signal envelope and $S(t)$ is the signal corresponding to a single micro-bunch; any two successive micro-bunches in the bunch train are separated in time by $\delta t = \frac{1}{f_0}$ where $f_0 = 1.3$ GHz, the operating RF frequency. $N = \frac{T}{\delta t}$ is the total number of micro-bunches in the bunch train corresponding to the RF macro-pulse of duration T. The fast-Fourier transform (FFT) of $V(t)$ provides a bunching factor $b(f)$ corresponding to the frequency f [74]. If the duration of $V(t)$ is short, then $b(f)$ is enhanced at the frequencies nf_0 (with $n \geq 2$), the harmonic frequencies of f_0; this concept was earlier demonstrated in Fig. 4.4. Figure 6.34 shows the voltage signal induced by the beam from the large cathode (a) and the corresponding FFT (b). The five peaks in the FFT correspond to the data points $\{(nf_0[\text{GHz}], b(f))\} = \{(1.3, 1); (2.6, 0.28); (3.9, 0.49); (5.2, 0.07); (6.5, 0.20)\}$ respectively for $n = [1 - 5]$ demonstrating short bunching of the electron beam after RF acceleration [75]. From computing the relative amplitudes $\frac{b(nf_0)}{b(f_0)}$ for different $V(t, E_0)$ signals, where E_0 is

Table 6.3: Inferred enhancement factors and effective emission areas for the cases considered in Figs. 6.32 and 6.33. The values in the brackets correspond to the ϕ values of 4.5, 4.9 and 5.4 eV respectively.

large cathode		
Configuration	β_e, ϕ = [4.5, 4.9, 5.4] eV	$\mathcal{A} \times 10^7$ [m^2]
large cathode, sol. ON	[349.66, 397.31, 459.64]	[0.94, 0.91, 0.88]
large cathode, sol. OFF	[421.64, 479.08, 554.25]	[0.038, 0.037, 0.036]
small cathode		
Configuration	β_e, ϕ = [4.5, 4.9, 5.4] eV	$\mathcal{A} \times 10^{16}$ [m^2]
small cathode, T	[413.89, 470.28, 544.07]	[4.71, 4.57, 4.37]
small cathode, T+2 wks	[446.94, 507.84, 587.52]	[1.53, 1.49, 1.42]

the peak electric field in the RF gun, the bunch (rms) duration was estimated $\sigma_t \simeq 67 \pm 25$ ps in [74] assuming a Gaussian signal $S(t)$.

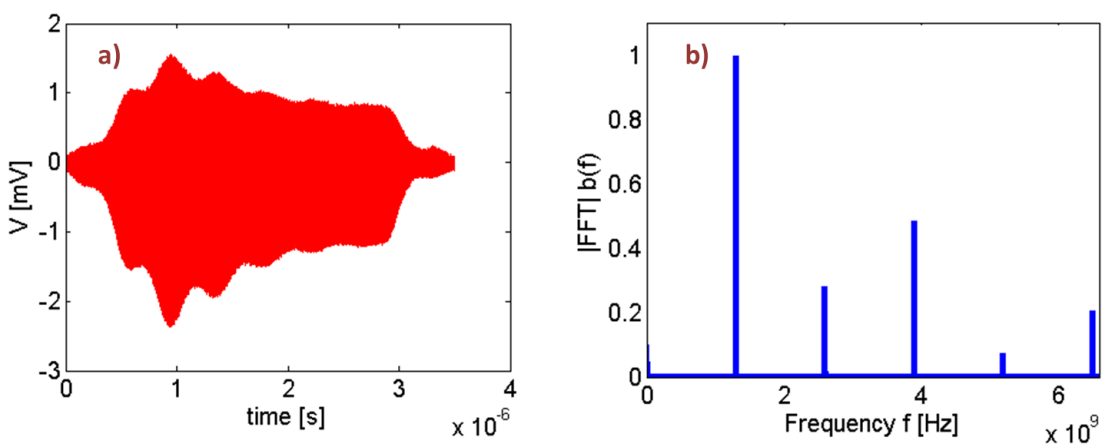

Figure 6.34: Voltage signal induced by the beam emitted from the large cathode, detected by the electromagnetic pick-up (a) and the corresponding FFT (b).

6.4.2.3 Transverse Beam Characteristics and Current Stability

An important figure of merit of a field-emitted beam is its transverse emittance. The horizontal emittance of the full bunch train was characterized for the small cathode. The multi-slit mask located at position X3 was inserted and the transmitted beamlets were observed at location X5 using the procedure described in Section 2.2.4.1. The measurement indicates a transverse horizontal emittance of $\epsilon_x = 2.64 \pm 0.8$ μm for the small cathode. Emittance measurements for the large cathode were compromised by an inconclusive measurement of the mean energy due to a large energy spread.

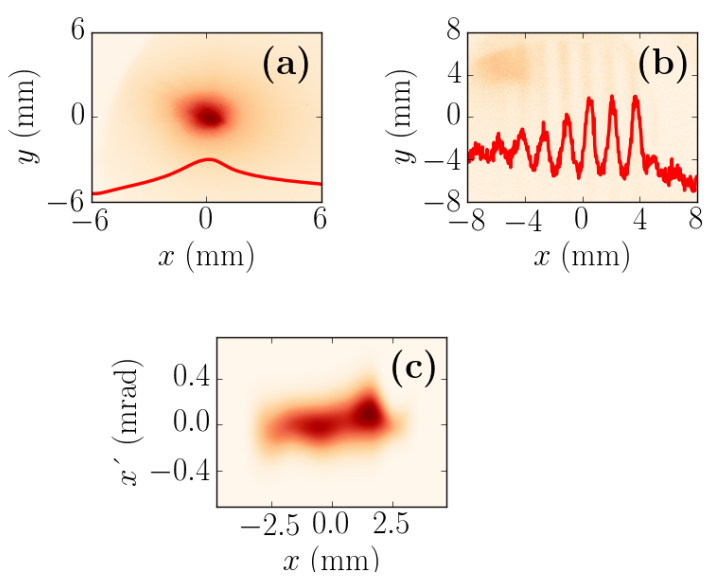

Figure 6.35: Emittance measurement snapshots showing the beam's transverse distribution at X3 for the small cathode (a), the transverse distribution of the beamlets transmitted through the multi-slit mask observed at X5 (b) with associated horizontal projections $[x, x'(\equiv p_x/p_z)]$ trace space at the location of X3 from processing of images (a) and (b) [74].

Finally, the stability of a high current electron source is crucial for some applications. The current stability over a few hours was tested and it was confirmed that

both cathodes were able to sustain the production of high average currents with very low jitter; see Fig. 6.36 (a).

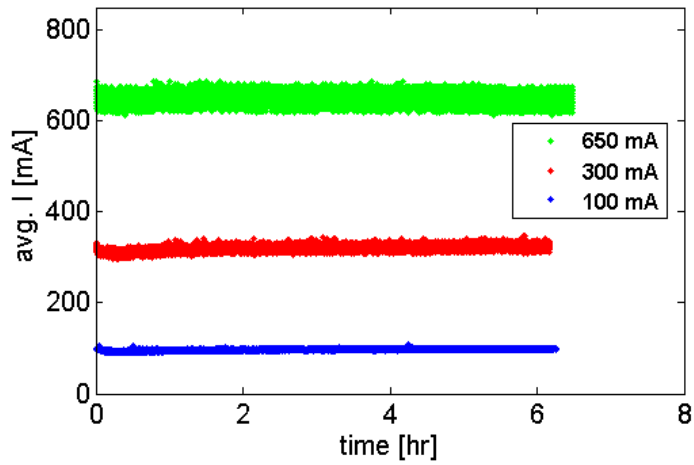

Figure 6.36: Current stability over a > 6-hour period for 100, 300 and 650 mA current.

In summary, we have demonstrated the operation of a CNT cathode in an RF source and produced bunch trains with operating average current $\bar{I}$ of up to 0.65 A and rms duration of 70 ps implying a charge per bunch of $Q \simeq \bar{I}/f_0 \simeq 0.50$ nC corresponding to the peak current of a single bunch $\hat{I} = Q/\sigma_t\sqrt{2\pi} \simeq 3$ A. The explored cold-cathode technology along with superconducting RF (SRF) technology can enable production of long trains of bunches, hence producing high average current. The main challenge for such an endeavor remains the temporal control of emission time, since FE cathodes emit over a broad phase of the RF period. Such a long emission not only gives rise to high energy spread in the beam but also can lead to multipacting, as observed in some of our experiments, leading to RF cavity damage, or quenching in the case of SRF cavities. Hence development of emission control technologies of FE bunches is crucial. One possible solution to this problem is a

dual-frequency gun [76] that can support a fundamental and a harmonic frequency, could effectively gate the emission at the proper RF phase.

CHAPTER 7

BEAM APPLICATION STUDIES

With a goal of performing comprehensive studies with regards to electron beams generated in an RF gun, three experiments were performed at HBESL that encompass beam applications. These experiments include the design of an inverse Compton scattering (ICS) experiment using a ~ 4 MeV electron beam for the generation of soft x-rays, the experimental generation of ellipsoidal beams, and the temporal beam shaping using birefringent crystals. These application studies supplement the charge generation experiments discussed in the previous chapters demonstrating a general research of electron beams.

7.1 Design of Inverse Compton Scattering Experiment

7.1.1 Introduction and Motivation

The inverse Compton scattering (ICS) is an electron–photon scattering in which energy transfer from a relativistic electron to the interacting photon occurs, thus increasing the frequency of the (back-) scattered photon. ICS experiments have been routinely demonstrated to generate high brilliance (sometimes referred to as brightness) X-rays whose applications encompass a number of areas including medical imaging, microscopy, solid state physics, material science and beyond [77]. Brilliance (B) is an important and widely used figure of merit to characterize x-rays,

defined as the number of photons per unit time, per unit area, per unit solid angle per 0.1% of frequency bandwidth of x-ray beams given as

$$B(t) = \frac{dN}{dt d\mathcal{A} d\Omega(\frac{\Delta\nu}{\nu})} \tag{7.1}$$

where N is the number of photons, t is time [s], $\mathcal{A}$ is the area of cross section [mm^2], Ω is the solid angle [mrad^2] and $\Delta\nu$ is 0.1% of the center frequency ν [Hz]. Increasing the brilliance [s^{-1}mm^{-2}mrad^{-2}] not only will increase the resolution of conventional x-ray applications but will pave ways for new opportunities such as x-ray phase-contrast imaging.

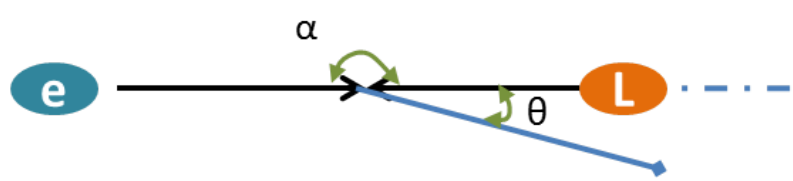

Figure 7.1: A diagram of an ICS scenario in the laboratory frame. The ellipses 'e' and 'L' represent an electron beam and a laser beam respectively. The angles α and θ represent the collision angle and the observation angle respectively.

If a relativistic electron beam ($\beta \simeq 1$, where $\beta = \sqrt{1 - \frac{1}{\gamma^2}}$) with Lorentz factor γ collides (head-on) with a laser beam of frequency ν_L at an angle α as shown in Fig. 7.1, then the frequency ν_X of the backscattered radiation as a function of the observation angle θ is given as [78]

$$\nu_X(\theta) \approx \frac{2\gamma^2\nu_L\big[1 - \cos(\alpha)\big]}{1 + \frac{K^2}{2} + \gamma^2\theta^2}, \tag{7.2}$$

where α is the collision angle, K is the wiggler strength which indicates the vector potential of the laser [79], and is given in more convenient units as $K = 25.6 \times \lambda_L[\mu\text{m}]\sqrt{I}[\text{W/cm}^2]/c[\text{cm/s}]$, where c is the speed of light, $\lambda_L(= c/\nu_L)$ and I are the laser wavelength and intensity respectively. From Eq. 7.2, the maximum photon

energy ($\equiv h\nu_X$, where h is the Planck's constant) for a given set of electron and laser beam parameters is obtained when α is 180° i.e when the collision is perfectly head-on, and for $\theta = 0$, i.e. along the direction of the electron beam. In the range $K \ll 1$ (and $\alpha = 180^o$, $\theta = 0$), Eq. 7.2 reduces to

$$\nu_X \approx 4\gamma^2\nu_L. \tag{7.3}$$

Most ICS experiments utilize high energy electron and laser beams to produce brilliant and high energy light sources like hard x-rays. The current experiment was designed to produce soft x-rays ($\lambda \sim$ 1-20 nm) at HBESL using a low energy electron beam ($\sim$ 4 MeV) as Massachusetts Institute of Technology's (MIT) initial attempt to develop a compact ultrafast bright and intense x-ray (CUBIX) source using a compact THz-wave undulator [80]. The detection of the backscattered radiation requires more sensitive detectors if low energy electron beams were to be used, due to low photon flux, which was one of the challenges of the experiment. The experiment was designed, installed and carried out at HBESL as a proof-of-principle concept to generate and detect soft x-rays utilizing a 800-nm laser.

Taking HBESL's laser specifications given in Table 7.1, we get $I = 1.11 \times 10^{13}$ [W/cm^2] and $K = 0.0023$. For an electron beam with an average energy of 4 MeV ($\gamma \simeq 7.82$), we get $\lambda_X \simeq 3.27$ nm ($\lambda_X \equiv \frac{c}{\nu_X}$ at $\theta = 0$ (on axis) using Eq. 7.3). This wavelength corresponds to soft x-ray regime. A complete information of the backscattered radiation includes its spectral intensity, spatial and temporal distributions evaluated over the entire parameter space of the interacting electron and laser beams. However, in the current experiment we attempted to make a successful spatio-temporal alignment of the laser and electron beams and later on detect any ICS radiation, rather than full characterization.

7.1.2 Experimental Setup

The ICS experiment involved implementing mainly three aspects; design and installation of the ICS interaction chamber, spatio-temporal alignment of the electron and laser beams, and the detection of ICS radiation.

HBESL's amplified laser output, as mentioned before in Chapter 4, has a maximum repetition rate of 1 KHz, which means the minimum temporal separation between two consecutive laser pulses is 1 ms. This puts a requirement of using a laser pulse for the ICS that also generates the photo-emitted beam. (An alternative would be to use an auxiliary laser system's pulse that is triggered by the same trigger as the laser used for photoemission, which imposes additional requirements on the needed resources). A schematic of the experiment is shown in Fig. 7.2, where a residual 800-nm IR pulse output during the process of frequency tripling (see Section 3.7) is used for the ICS, while the corresponding UV pulse generates the photo-emitted electron beam. A dichroic mirror which transmits IR but reflects UV was used to separate the IR and UV pulses for this purpose.

The laser and the electron beams interact head-on inside an interacting chamber and the point of interaction is called the interaction point (IP). The laser is directed towards and away (outside of the beamline) from the IP using a pair of off-axis parabolic (OAP) Aluminum mirrors OAP1 and OAP2 respectively (see Fig. 7.2). It is highly desired that the laser beam moving away from the IP is dumped properly outside the beamline to avoid any unnecessary laser scattering off of the beamline components; otherwise the scattered laser can interfere with the ICS radiation's signal as received by a photodiode (PD) detector installed $\sim$ 1 m downstream of the interaction chamber. The electron beam is let straight through OAP1 and OAP2

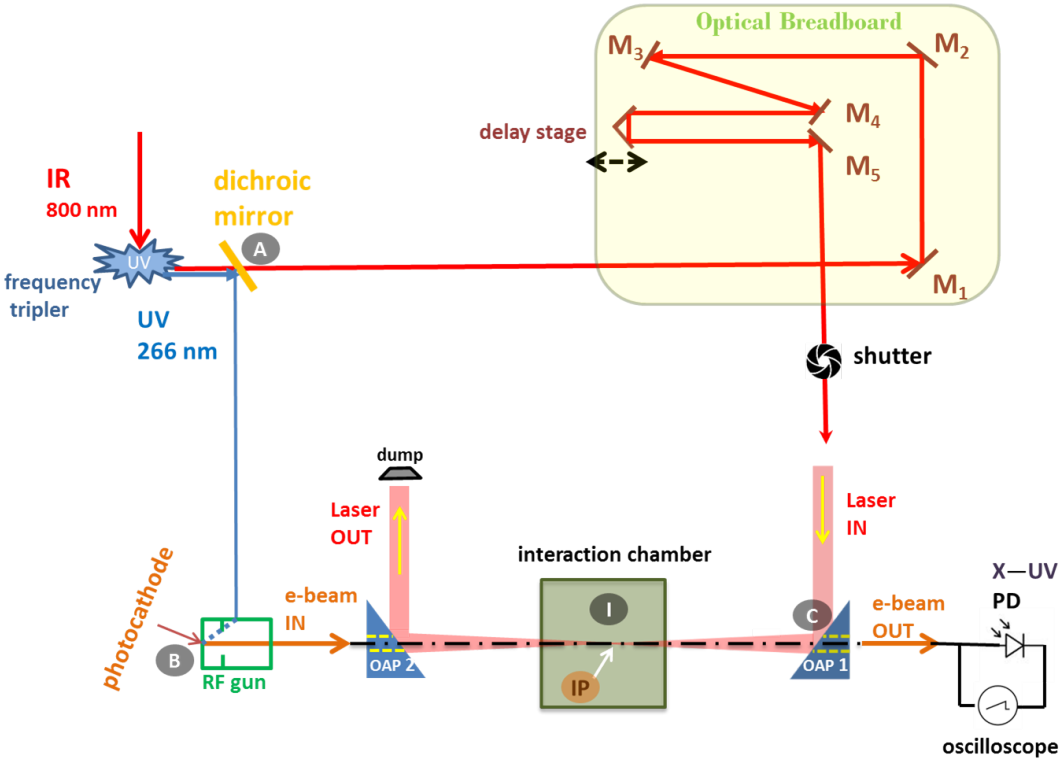

Figure 7.2: A Schematic of the ICS experiment. 'IP' stands for interaction point and 'PD' for photodiode. Note: items are not to scale.

via 3-mm diameter through-holes (yellow dashed lines in Fig. 7.2) at the centers of the mirrors. The laser energy lost due to the presence of the holes is assumed to be minimal.

The design and installation of the ICS interaction chamber: the interaction chamber consists of a 6-way cross (see Fig. 7.3) which houses a vertical actuator arm that can insert or remove a YAG screen at an angle 45° to the beam axis. The YAG screen is used for spatial as well as temporal alignment of the laser and electron beams which is described later in this section. A charge-coupled device (CCD) camera focused onto the YAG screen allows to remotely obtain an image of the laser or the electron beam. The IP lies approximately at the center of the 6-way cross which also corresponds to the center of the YAG screen when inserted into the

chamber. On each side of the interaction chamber, there is a cube-cross that houses the the respective OAP mirror. The OAP mirrors are mounted on their respective links (housed by bellow flanges that can vary their lengths) that are attached to the base flanges, and can be independently lowered or raised for vertical spatial laser alignment. This is done by lowering or raising the lab-jacks that are attached to the base flanges using c-clamps. The lab-jacks themselves can be rotated about the vertical axis as they are screwed to the respective rotating stages directly underneath them, thus allowing for rotational alignment of the OAPs before the base assembly is sealed for vacuum. The viewports have anti-reflective coatings for 800-nm laser to transmit maximum laser power.

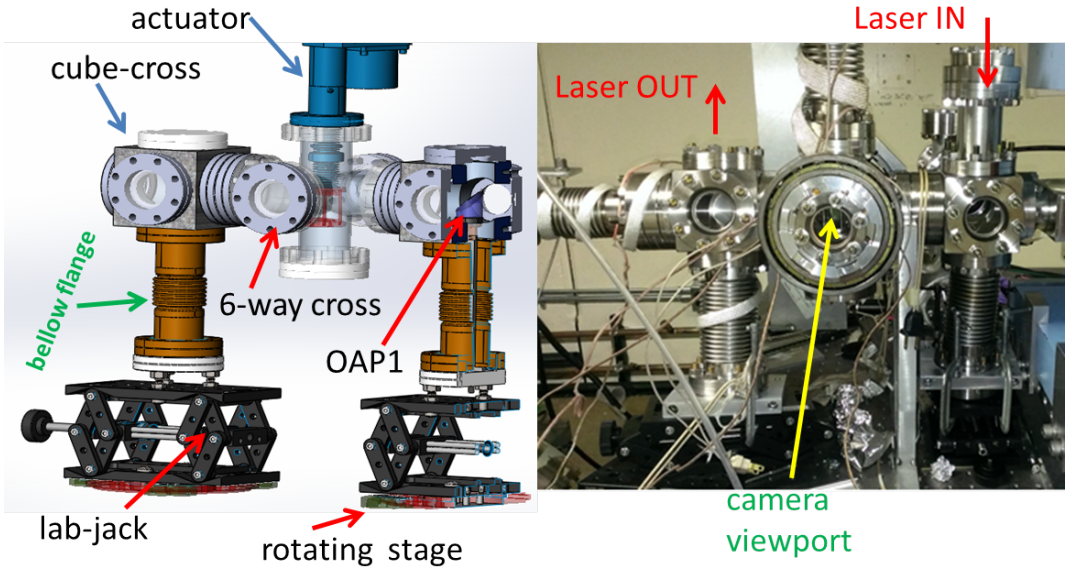

Figure 7.3: Design of the ICS interaction chamber: sectional view of a computer aided drawing (CAD) assembly (left) and a photograph of the actual installation (right).

Spatial alignment: the spatial alignment was done such that the IR laser traversed (with the help of a HeNe laser) approximately through the center of all the optics and also such that using the delay stage didn't noticeably alter the beam's

path. Use of HeNe lasers to align Class 4 lasers like in our case, is a standard procedure for obvious safety and convenience reasons. This is done by first spatially aligning a HeNe laser onto a class 4 laser using several mirrors, and later using the HeNe laser as a replacement for the Class 4 laser during alignment. For the spatial alignment within the interaction chamber, OAP1 was adjusted using the rotational stage and the lab-jack mentioned previously, to align the laser beam onto the center of the YAG screen. The electron beam was spatially aligned with the center of the YAG screen by utilizing the steering magnets. Later the electron beam was empirically focused to the smallest possible size using the quadrupole magnets. Figure. 7.4 shows the photographs of the laser and electron beams on the YAG screen at the IP as grabbed by the CCD camera. This pertains to the spatial alignment of the electron and laser beams.

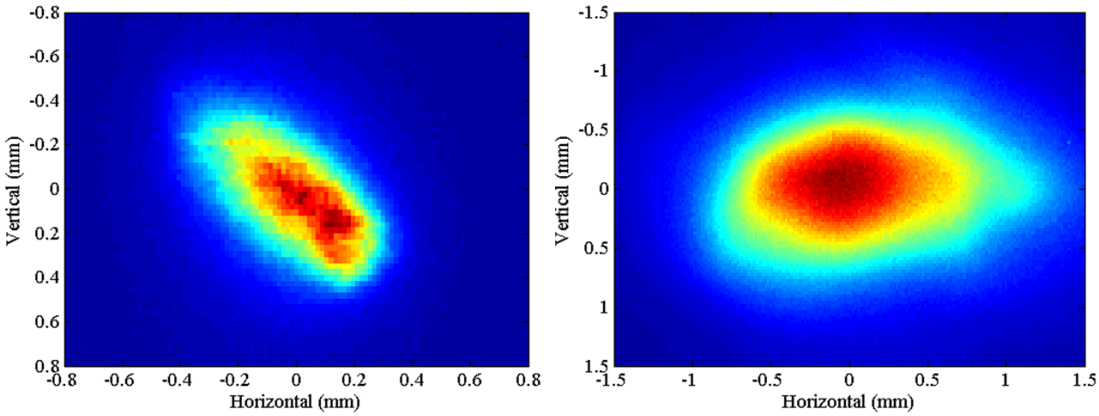

Figure 7.4: CCD images of the laser (left) and the electron beam (right) at the IP [81].

The images in Fig. 7.4 appear to be saturated, so the actual beam sizes are likely smaller than displayed. From the figure, we estimated the laser transverse size to be ~ 0.2 mm radius and the electron beam's as ~ 0.75 mm radius. For an experiment

like ICS, spatio-temporal alignment remains to be the most critical and arduous aspect.

Table 7.1: Important experimental specifications of the ICS experiment.

laser	1.4 mJ (energy/pulse)	100 fs (FWHM) $\sim$ 0.2 mm spot radius	800$\pm$25 nm (bandwidth)
e-beam	4 MeV (mean energy)	$\sim$ 100 fs (temporal) 0.75 mm spot radius	500 pC (charge/bunch)
photo-diode	2.2 ns (rise time)	100 ps (resolution)	100 electrons/photon at 480 eV (calibration)

Temporal alignment: in order for the laser and electron beams to overlap in time at the center of the YAG screen inside the interaction chamber, one needs to ensure that both beams travel roughly the same distance from a reference point, when the speed of the electron beam is approximated as c. This means that in Fig. 7.2, the path distance

$$\underbrace{\overline{\mathrm{AB}}}_{\text{UV pulse}} + \underbrace{\overline{\mathrm{BI}}}_{\text{e-beam}} = \underbrace{\overline{\mathrm{AC}} + \overline{\mathrm{CI}}}_{\text{IR pulse}}.$$

To ensure this, first the path length $\overline{\mathrm{AB}}+\overline{\mathrm{BI}}$ was measured to be $\sim$ 7 m using a tape measure. In order to make the path length $\overline{\mathrm{AC}}+\overline{\mathrm{CI}}$ of the IR laser the same, mirrors M_1, M_2 etc. were added on an optical breadboard (see Fig. 7.2) which included a motorized delay stage for fine-tune delay adjustment of the IR laser within $\pm$20 mm. In practice,

$$\left(\frac{\overline{\mathrm{AB}} + \overline{\mathrm{BI}}}{c}\right) = \left(\frac{\overline{\mathrm{AC}} + \overline{\mathrm{CI}}}{c} + \delta t\right)$$

since the electron beam starts from rest, where δt (> 0) is time lag (delay) of the electron beam with respect to the IR laser pulse on the order of a few ns, which corresponds to a path difference of tens of cm between the laser and electron beams. Hence the IR pulse's path $\overline{\mathrm{AC}} + \overline{\mathrm{CI}}$ was made longer (by tens of cm) with respect to the path $\overline{\mathrm{AB}} + \overline{\mathrm{BI}}$. When the laser pulse hits the YAG screen, a small fraction of the reflected laser makes it back to the PD and the corresponding signal can be seen on a fast-sampling (11 GHz) oscilloscope connected the PD. Also, when the electron beam hits the YAG screen, the electron-induced radiation generated by the electron beam also reaches the PD and the corresponding signal is seen on the oscilloscope alongside with the (reflected) laser's signal. It can be noted that there is no control over the electron beam's time of arrival at the center of the YAG screen, as the injection phase of the UV laser for photoemission is to be maximized for the energy of the electron beam. Therefore the path length of the IR laser was iteratively adjusted by adding or subtracting a mirror on the breadboard to bring the two signals within $\pm\frac{20\ \mathrm{mm}}{c} \sim \pm 70$ ps to be in the range of the delay stage. This corresponds to the coarse synchronization.

While monitoring the two signals on the oscilloscope, the laser delay stage was remotely adjusted to overlap the two signals. The overlapped signals mean that the laser and the electron beams hit the YAG screen at the same time, as it can be noted that both the reflected laser and the electron-induced radiation travel the same path length i.e. from the YAG screen to the PD. This pertains to the fine synchronization.

7.1.3 Measurement

After the spatio-temporal alignment of the electron and laser beams was ensured as described previously, the YAG screen was retracted to allow for the two beams to interact directly at the IP. The overall signal detected by the PD includes superfluous unwanted background signals from the scattered laser and electron beams. In order to identify any ICS x-ray signal from the PD whose specifications are given in Table. 7.1, we looked for the signal that would appear only in the region of synchronized electron and laser beams, i.e. when the laser delay stage was in the right range.

An electronic shutter (see Fig. 7.2) in the path of the laser allowed for the blocking and unblocking of the laser into the ICS chamber. The electron beam could also be blocked by using one of the gate-valves located upstream of the interaction chamber in the beamline. By blocking and unblocking the laser and electron beams independently, several attempts were made to subtract the background noise in the PD signal. Figure. 7.5 shows the PD signal after background subtraction as a function of the laser delay. A Gaussian fit (red trace in the figure) to the data resulted in the fit equation $y = 2.58\exp[\frac{-(x+0.14)^2}{2.82^2}]$ with a standard deviation $\sigma \simeq 2$, where y represents the PD signal [mV] and x represents the IR path delay [mm]. It can be noticed that the signal fades away as the point of collision moves away from the laser focus, which is a direct evidence of the detection of the ICS radiation. The cross-correlation signal of the electron and laser beams shown in Fig. 7.5 approximately represents the bunch, since the bunch duration is a couple orders of magnitude greater than the laser duration. Hence the rms bunch duration is approximately $\frac{2\text{ mm}}{c} = 6.6$ ps, which falls within the expected range.

When the spatial overlap of the electron and laser beams was slightly and intentionally misaligned by steering the laser beam away from the IP using M5 (see Fig. 7.2), no ICS signal was observed as a function of the laser delay, further assuring that the signal shown in Fig. 7.5 is associated with the ICS backscattered radiation.

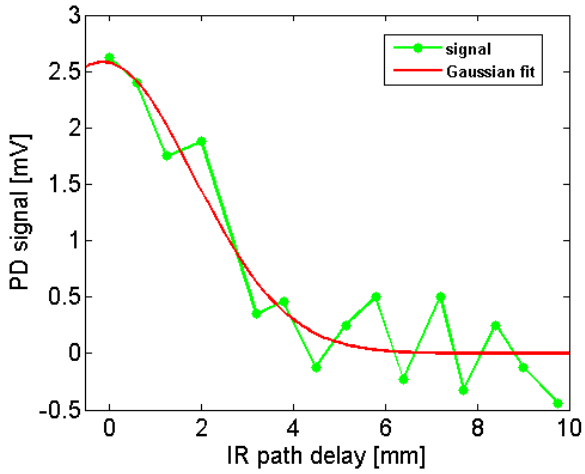

Figure 7.5: ICS signal (green trace) as a function of laser path delay and the corresponding Gaussian fit.

7.1.4 Conclusion

In conclusion, a successful design and installation of the ICS experiment was demonstrated with a low energy 4-MeV electron beam and a 800-nm laser. This experiment also expanded HBESL's diverse research capabilities towards the applications of bright electron beams. Although the ICS radiation could not be quantitatively characterized, it was a first hint that low energy electrons can be used to develop a soft x-ray source. Finally we note that the setup assembled for the ICS was also employed to support some research on channeling radiation (CR); see Ref. [82].

7.2 Generation of Ellipsoidal Electron Bunches using Cesium Telluride Photocathode

7.2.1 Introduction and Motivation

Uniformly filled 3D ellipsoidal electron bunches offer the advantage of effective suppression of space charge induced emittance growth due the linear dependence of the space charge fields with the position within the beam [83]. Such a beam with $E_u \propto u$, where E_u is the component of the electric field in the direction of the spatial coordinate $u \in \{x, y, z\}$, undergoes simple beam dynamics and is ideal for controlled high brightness charged particle acceleration [84]. Producing uniform ellipsoidal beams previously remained elusive due to the experimental complexity of the suggested methods [85, 11], e.g. by using a photoemission drive laser that is similarly shaped to the ellipsoidal beam. Serafini [86] and Luiten [84] proposed a simple way of realizing uniform ellipsoidal beams by using a laser pulse (for photoemission) whose duration is much shorter than the final bunch duration without any requirements on the laser's transverse shape. Since then, production of ellipsoidal beams has been demonstrated using ultrashort laser pulses on metallic photocathodes. Such a method employs the formation of ellipsoidal bunches via space charge dominated expansion called the 'blowout' regime [86]. The blowout regime is achieved if the condition below is satisfied [84];

$$\frac{eE_0 c\tau_l}{m_e c^2} \ll \frac{\sigma_0}{\epsilon_0 E_0} \ll 1, \tag{7.4}$$

where e, E_0, c, τ_l, m_e, σ_0 and ϵ_0 are respectively the electronic charge, the accelerating electric field, the speed of light, the duration of the photoemission process, the electronic mass, the initial surface charge density on the photocathode and the electric permittivity of the free space. From the above condition, it has been shown that in general a high E_0, a small τ_l and a low σ_0 favors the formation of an ellipsoidal bunch [87]. Formation of ellipsoidal bunches was experimentally demonstrated using a prompt (metallic) photocathode, high E_0 (80 MV/m) and $\tau = 35$ fs laser pulses [11]. Ellipsoidal bunches were also generated at the now-decommissioned A0PI at Fermilab using a Cs_2Te photocathode, $\tau < 200$ fs laser pulses and $E_0 \approx$ 35 MV/m. The combination of a booster cavity that accelerated a 4-MeV beam to 16 MeV and a spectrometer magnet was used to characterize the longitudinal phase space of ellipsoidal beams [88]. In the present experiment, we used a transverse deflecting cavity (TDC) to make a more direct characterization of the 4-MeV ellipsoidal bunches generated using a Cs_2Te photocathode, $\tau = 100$-fs UV drive laser and an electric field $E_0 \approx 35$ MV/m. The operation of the TDC is described in Section 2.2.2.2.

7.2.2 Numerical Simulations

ASTRA simulations (see Fig. 7.6) were performed to study the temporally mapped transverse distribution of the electron beam deflected by the TDC. The input parameters in ASTRA approximately correspond to the experimental parameters, which are as follows; laser pulse length $\tau = 33$ fs (rms) (a sixth of a 200-fs full width Gaussian temporal emission), laser transverse spot size $XY_{rms} = 1.3$ mm (rms) (a forth of 5.2-mm diameter of a uniform circular distribution), peak electric field in

the RF gun E_0 = 34 MV/m and the peak electric field of the TDC E_T = 0.32 MV/m. In Fig. 7.6, the view of interest is 'Front View @ 3m' as it corresponds to the temporally mapped x ($\propto t$) $- y$ distribution of the beam after the TDC. It can be noted in the figure that as the charge density increases, the asymmetry of the ellipsoidal bunch increases. The asymmetry appears around Q=800 pC (σ_0 = 37.67 pC/mm^2), and at Q=1.2 nC a tail-like structure is clearly evident. This effect is understood as when the image charge fields due to a high σ_0 become comparable to the accelerating gradient E_0, the fields exert decelerating forces on the beam near the cathode, thus giving rise to a tail-like structure to the beam. This effect is implicit in condition 7.4. Also shown in Fig. 7.6 is the bunch charge as a function of XY_{rms}. At low XY_{rms} values, the initial charge density is so high that the emission of the tail of the bunch is inhibited by the space charge forces exerted by the bunch's head as evident in the figure. No quadrupole magnets were included in the ASTRA program in order to observe the natural space charge induced transverse shape and size of the beam.

7.2.3 Experiment

The parameter σ_0, the surface charge density, is given by $\sigma_0 \equiv Q/(\pi r^2)$, where Q is the bunch charge and r is the uniformly distributed laser transverse spot radius on the photocathode. Q could be varied by varying the drive laser energy and r by varying the size of an iris the laser goes through. We obtained the longitudinal ellipsoidal structure of the beam for different σ_0 values and expected the ellipsoidal structure of the beam to be spoiled at higher σ_0 values. We considered two laser spot radii (rms) viz. 2.6 mm and 3.25 mm, and for each spot size we considered 4

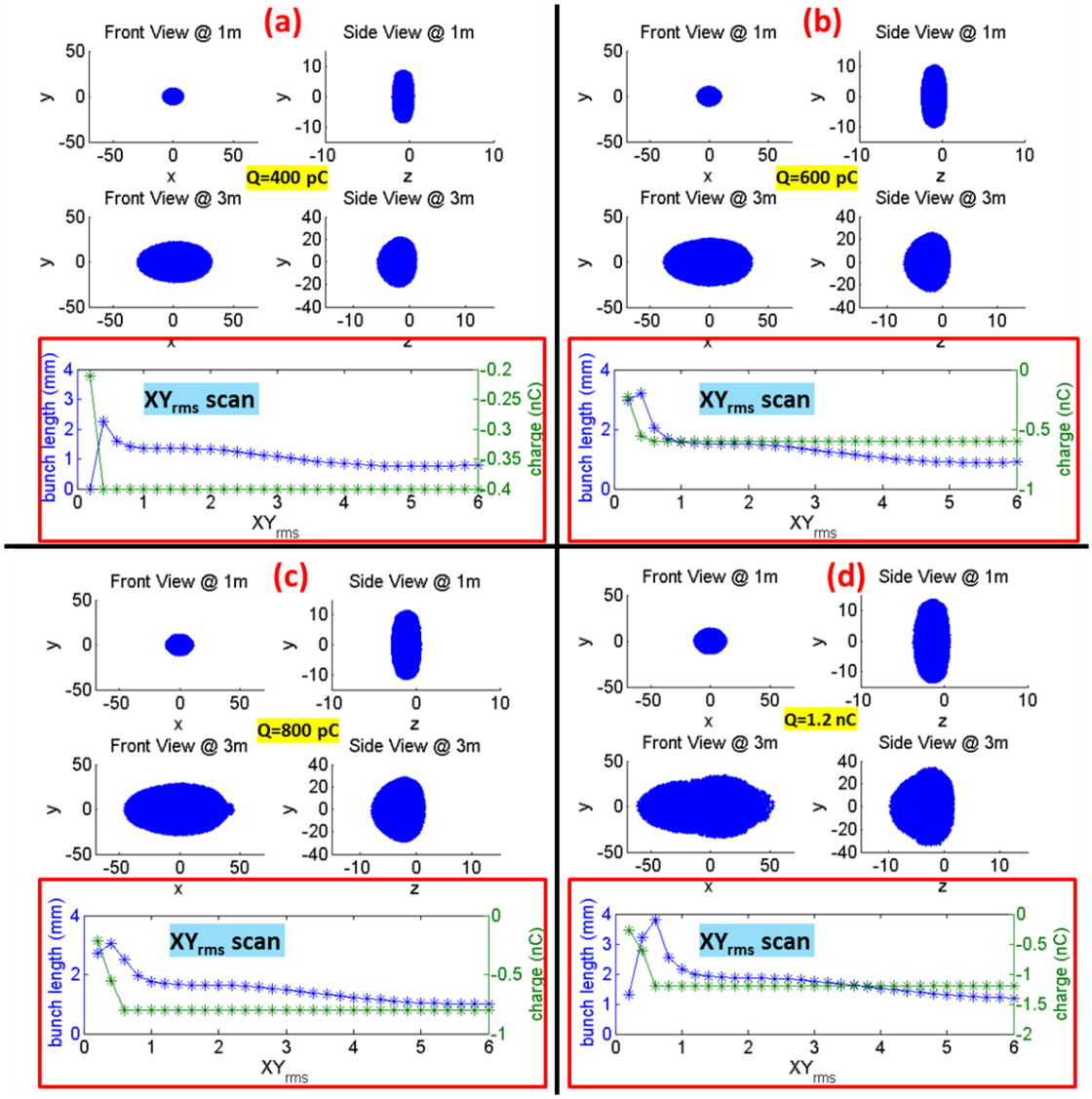

Figure 7.6: ASTRA simulations of the evolution of the electron beam profile as a function of charge density. In the scatter plots [a-d] in the order, the charge density is increased by increasing the initial charge (Q) (indicated in yellow text boxes) of the bunch while maintaining the initial rms spot size $XY_{rms} = 1.3$ mm. The beam positions 1 m and 3 m respectively correspond to the locations before and after the TDC. The bottom sub-plot in each of the plots [a-d] show the bunch charge and the bunch length as a function of XY_{rms} for the corresponding initial charge (constant) values shown in the yellow text boxes. (All dimensions of length are in mm).

charge values, viz. 600, 400, 160 and 80 pC to evaluate the ellipsoidal nature of the electron beam.

Since the central beam energy was measured to be 4.84 MeV using the spectrometer and the YAG screen at XS3, the peak electric field requirements on the TDC was minimal. For a given low E_T ($\sim$ 0.32 MV/m), the TDC was calibrated by obtaining the phase–deflection curve at X7 YAG screen (see Fig. 2.5) located $\sim$ 3.1 m downstream of the TDC.

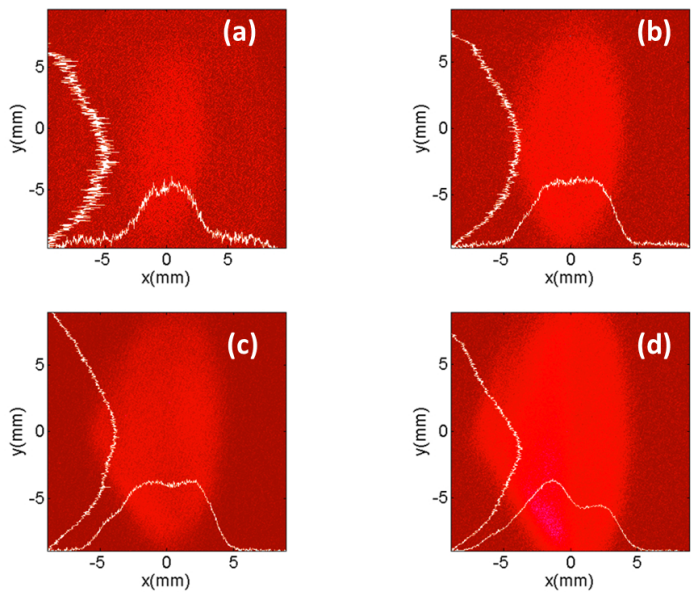

Figure 7.7: The transverse ($x \propto t$) distribution of the beam for 80 pC ($\sigma_0 = 3.76$ pC/mm^2) (a), 160 pC ($\sigma_0 = 7.5$ pC/mm^2) (b), 400 pC ($\sigma_0 = 18.83$ pC/mm^2) (c) and 600 pC ($\sigma_0 = 28.25$ pC/mm^2) (d) observed on X7 YAG screen. The white traces are the corresponding projections along the respective axes, where x corresponds to the deflection axis.

Figure 7.7 shows the transverse distribution of the beam for different charge values for the laser spot with size 2.6-mm radius. The associated intensity projections are shown as white traces. It can be observed in Fig. 7.7 that the 80-pC (a) and 160-pC (b) beams exhibit ellipsoidal shape (sharp edges of the white traces along y) to the most extent, but the beams with a higher charge—and hence a higher σ_0—do not retain their ellipsoidal shapes. The appearance of the asymmetric tail at high σ_0 values is consistent with the trend observed in the ASTRA simulations shown in

Fig. 7.6. However, based on graphical comparison between Figures 7.6 and 7.7, the σ_0 value at which the asymmetry appears in the experiment ($\sigma_0 \sim 18.83$ pC/mm^2) is different from that of the simulations ($\sigma_0 \sim 37.67$ pC/mm^2). This discrepancy can be attributed to the inhomogeneous regions in the laser transverse distribution shown in Figure. 7.8 which induce much stronger local σ_0 values than the average σ_0 over the spot. The inhomogeneities were caused due to the dispersive effects and spatial inhomogeneities in the laser optics.

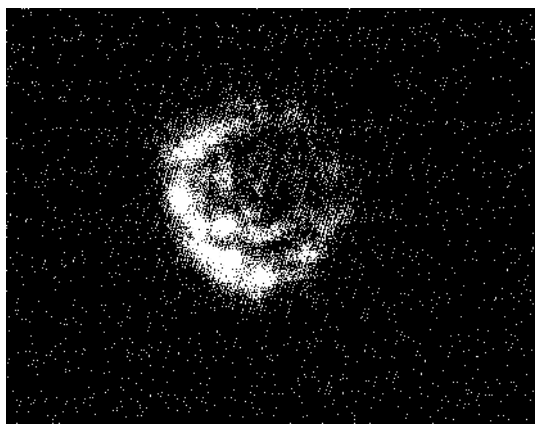

Figure 7.8: A gray-scale image of the laser transverse distribution as detected on the virtual cathode.

Emittance measurements of 4.28, 3.73 and 2.9 μm (Fig. 7.9) were obtained for the beams with charge values of 600 pC ($\sigma_0 = 28.25$ pC/mm^2), 400 pC ($\sigma_0 = 18.83$ pC/mm^2) and 150 pC ($\sigma_0 = 7.05$ pC/mm^2) respectively for the laser spot with radius 2.6 mm using the multi-slit method. The slits were located at X3 while the images of the beamlets on the X5 YAG were processed to calculate the emittance values, as described in Section 2.2.4.1. The measured transverse trace space (x) plots shown in Fig. 7.9 show the linear mapping between the $x - x'$ trace space, a characteristic of ellipsoidal bunches. For the laser spot with spot radius 3.25mm, the longitudinal profiles of the beams (not shown here) were observed to be consistently ellipsoidal due to lower σ_0 values when compared to those in Fig. 7.7. In all the

cases, the beam's transverse size was kept minimal using the quadrupole magnets before the TDC (X5) in order to minimize the contribution of transverse beam size on the beam's $x - y$ profile deflected after the TDC.

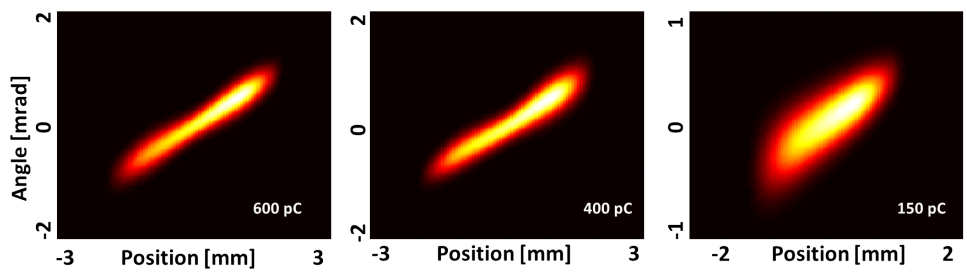

Figure 7.9: The transverse trace space of the beam measured at X3 using the multi-slit method for the different charge values shown. The emittance measurements of 4.28, 3.73 and 2.9 μm correspond to the plots from left to right respectively.

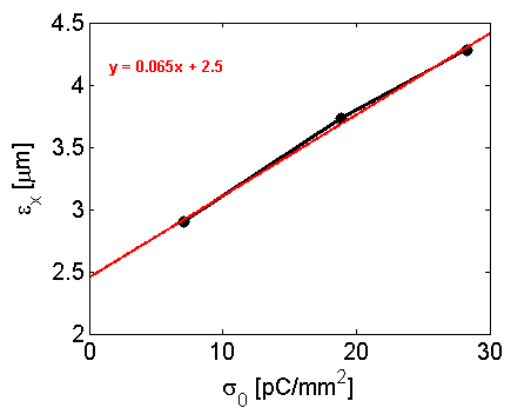

Figure 7.10: x-emittance as a function of the charge density corresponding to the beam's trace space distributions shown in Fig. 7.9. The red line is a linear fit to the data; also the fit equation is shown.

7.2.4 Conclusion

In conclusion, a direct experimental observation of the longitudinal profile of ellipsoidal beams produced from a Cs_2Te photocathode, using a transverse deflecting

cavity (TDC) was made. It was observed that the ellipsoidal characteristics of the beam are spoiled by increased charge density, consistent with the theory. The linear signature of the measured transverse (x) trace space at different charge densities is consistent with the ellipsoidal characteristics of the beam. It was shown that Cs_2Te photocathodes are capable of producing ellipsoidal bunches despite their slower response times when compared to metallic photocathodes. Finally, it is convincing that generation of ellipsoidal bunches using ultrashort drive laser pulses via blowout regime is a practicable technique.

7.3 Temporal Beam Shaping using Birefringent Crystals

7.3.1 Introduction and Motivation

Temporal shaping of electron bunches have several applications in accelerator physics, like improving the transform ratio in wake-field acceleration [89] and generation of THz radiation. Temporal shaping of electron beams is commonly done by similarly shaping the laser pulses used in photoemission. With the advent of new laser profiling techniques, e.g. with acousto-optic programmable dispersive filters (AOPDF), more complex electron beam shaping is possible. For simple temporal shaping of beams, birefringent crystals like Barium borate (BBO) serve as a direct, cheap and reliable tools to create a custom temporal bunch train for photoinjectors [90, 91] from a source laser pulse via photoemission. By using multiple crystals, a bunch train of more than two bunches with variable charge can be created [92], however such a process is quickly limited by the reduced laser energy for every crystal added.

A simple birefringent crystal has an 'ordinary' axis (OA) and an 'extraordinary' axis (EA) which are perpendicular to each other as shown in Fig. 7.11. The indices of refraction n_o and n_e respectively along the OA and the EA are unequal. When an incoming linearly polarized light wave with polarization oriented at an angle θ with respect to the OA enters the birefringent crystal, the polarization (E-field) components E_E and E_O that are parallel to the OA and the EA respectively therefore experience different levels of refraction. The component that experiences higher n has a slower phase velocity and hence lags behind the other component as they traverse through the crystal. The temporal phase delay between the two polarization components as they exit the crystal is thus $L\frac{\delta n}{c}$ where L, δn and c are the thickness of the crystal, the difference $|n_o - n_e|$, and the speed of light respectively. For the convention assumed in Fig. 7.11, we see that $E_E/E_O = \tan(\theta)$. If we define I_E and I_O as the intensities of the pulses corresponding to the electric fields E_E and E_O respectively, then we have $\frac{I_E}{I_O} = (\frac{E_E}{E_O})^2 = \tan^2(\theta)$. Hence the intensity ratio of the two pulses can be varied by varying θ by rotating the crystal. When $\theta = \{0^o, 90^o\}$, the laser electric field is along the EA and the OA respectively giving rise to a single pulse output out of the crystal.

A light pulse with $\theta \neq \{0^0, 90^0\}$ implies a split into two pulses whose polarizations are perpendicular to each other, one lagging behind the other. When an ultrashort light pulse with a finite bandwidth is sent through a birefringent crystal, the wavelength (λ) dependent refractive index, or the group index given to the first approximation as $n_g = n - \lambda\frac{dn}{d\lambda}$ [93] also should be considered. We are interested in the group delay between the two pulses after the exit of the crystal as the pulse envelope is of importance. Therefore in the case of an ultrashort light pulse, $\delta t = L\frac{\delta n_g}{c}$ where δn_g is the difference in group indices of the OA and the EA.

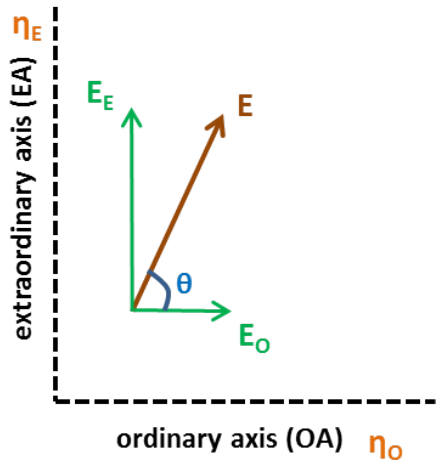

Figure 7.11: A diagram explaining principle of birefringence.

In this experiment, we used an α-BBO crystal (α refers to the crystalline structure) to create a bunch composed of two (twin) sub-bunches. Detection of the twin electron bunches generated by the corresponding twin laser pulses produced from the crystal was made. The temporal separation between the twin bunches was estimated from the charge vs. laser–RF relative phase plots for different θ values. The twin bunches were also observed using the TDC.

7.3.2 Experiment

A 18-mm thick α-BBO crystal of 5-mm$\times$5-mm transverse dimensions was introduced directly in the path of the UV drive laser beam after frequency upconversion. The crystal was mounted on a rotatable mount to allow for varying θ. The charge dependence on the laser–RF relative phase (ϕ) in the absence of the crystal is shown in Fig. 5.10. When a twin-pulse train is used for photo emission, the expected pattern of the charge (Q) dependence on the laser–RF relative phase (ϕ) is explained in Fig. 7.12. An appearance of the shoulder is an evidence of the existence of twin

bunches separated by a relative phase of arrival $\Delta\phi$. For a 1.3-GHz RF pulse, the time period of 360^0 phase corresponds to $\simeq$ 769 ps in time, hence a $\Delta\phi$ of 1^0 corresponds to $\simeq$ 2.13 ps.

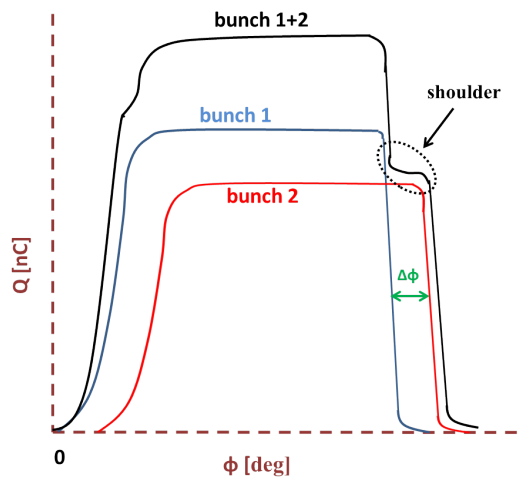

Figure 7.12: A diagram explaining the expected pattern of the charge dependence on the laser–RF relative phase for the twin bunches. The blue curve corresponds to the first bunch while the red for the delayed bunch. The black curve is the cumulative of both bunches. Note: items not to scale.

Fig. 7.13 shows the $Q - \phi$ plots for different θ values and the data without the crystal. It can be noted that in the presence of the crystal, part of the laser energy is lost in material absorption; hence the maximum charge obtained is less when compared to the case without the crystal. The estimation of $\Delta\phi$ for each case of θ in Fig. 7.13 was done using fitting equations [94]. A function $f(\Phi)$ was assigned from the fit to the $Q - \phi$ plot (see Fig. 7.13) for the case of $\theta = 0$. This was empirically achieved by graphically ensuring that the fit line approximately passes through the center of the corresponding data points. For a few of the other cases, a fit $I_1 f(\Phi + \phi_1) + I_2 f(\Phi + \phi_2)$ was obtained to extract $\frac{I_1}{I_2}$ and $\Delta\phi = \phi_1 - \phi_2$ where I_1, I_2, ϕ_1, ϕ_2 are the fit parameters. The results of this analysis are summarized in Table 7.2.

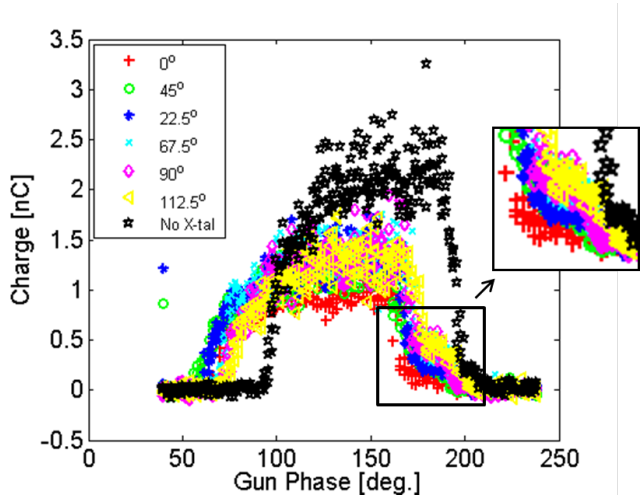

Figure 7.13: $Q - \phi$ plots for different θ values. The inset shows the region where the shoulders appear.

Table 7.2: Estimated fit parameters for the plots in Fig. 7.13 for four θ values [94].

θ	45^0	67.5^0	90^0	112.5^0
ratio $\frac{I_1}{I_2}$	2.4	3.8	4.1	2.6
$\Delta\phi$	8.6^0	7.4^0	8.2^0	7.8^0

It can be noted that $\Delta\phi$ is independent of θ and depends only on L. The average $\Delta\phi$ for the four θ values considered in Table. 7.2 is 8^0 which corresponds to a time separation between the twin bunches (or laser pulses) $\delta t \simeq 17$ ps. For an α-BBO crystal and $\lambda = 263$ nm, the delay is numerically estimated to be 0.864 ps/mm using Sellenmeir equation [94, 95]; this translates to $\delta t = 15.5$ ps for $L = 18$ mm in our case, which is in good agreement with the experimental value obtained (17 ps).

The twin bunches were sent through the TDC to make a direct observation of their temporal separation. If the phase of the TDC is set such that the centroid of the bunches passes through the zero-crossing (see Fig. 2.4) then the two pulses are transversely deflected in the opposite directions. The temporal separation is

therefore seen as spatial separation (δs) on the X7 screen. Figure. 7.14 shows the images of the electron beam at X7 with the TDC turned on and off.

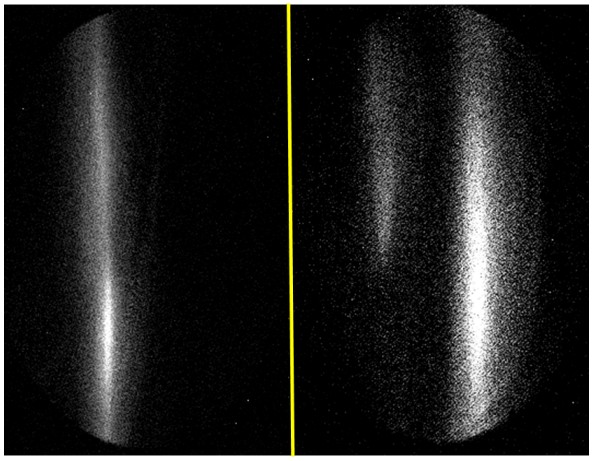

Figure 7.14: The electron beam on X7 screen with the TDC turned off (left), and turned on (right) revealing the twin bunches. The two bunches are slightly misaligned due to beam alignment errors on axis.

The spatial separation of the twin bunches is a function of the deflecting electric field E_T. By taking $\delta t \simeq 17$ ps, we propose to calibrate the TDC by obtaining the relation between δs and E_T as shown in Fig. 7.15.

7.3.3 Conclusion

In conclusion we demonstrated the temporal shaping of an electron beam using an α-BBO birefringent crystal. From the charge–phase plots, we made an empirical estimation of the temporal separation of the twin bunches which was in good agreement with previously known numerical estimation. A more direct observation of the temporally separated bunches was made using a TDC and a method of calibrating the TDC was proposed based on the known birefringence of the crystal.

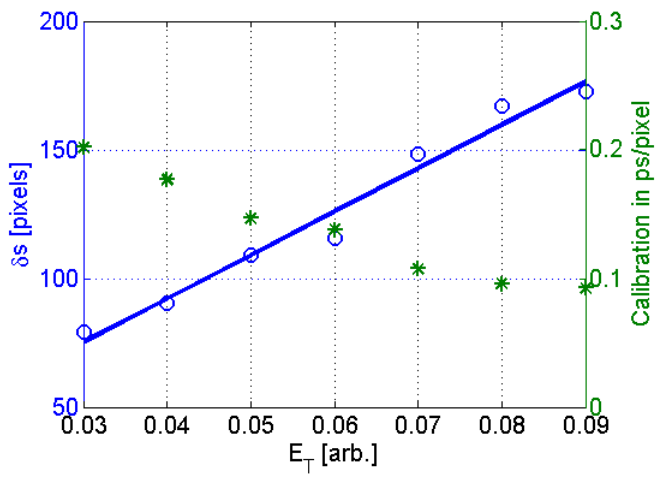

Figure 7.15: The spatial separation of the twin bunches on X7 screen downstream of the TDC as a function of E_T. Also shown is the $\delta t/\delta s$ calibration.

CHAPTER 8

CONCLUSION

A compact accelerator test facility was developed to conduct research dedicated towards the production of high brightness and high current electron beams. This involved the reconfiguration of a photoinjector beamline including the design, assembling and commissioning of the beamline. The facility's laser system was also upgraded to support the formation of broadband ($\sim$ 50 nm) amplified IR pulses necessary for the production of ultrashort laser pulses. This latter required the installation of a femtosecond seed laser synchronized with the photoinjector's RF system at the sub-picosecond level.

The reconfigured accelerator supported some studies on single and multiphoton photoemission from a Cesium Telluride (Cs_2Te) semiconductor photocathode that especially led to the observation of two-photon photoemission from Cs_2Te. A comparison of this nonlinear photoemission process with the linear emission indicates that the linear photoemission is several orders of magnitude more efficient. This result is in contrast to the case of a copper cathode studied in Ref. [52]; and the difference is attributed to the high linear photoemission quantum efficiency of Cs_2Te (compared to copper) and the fact that only a two-photon process was sustained compared to a three-photon process in Ref. [52].

The first operation of carbon-based field-emitter cathodes inside an RF cavity was demonstrated. The field-emitter cathodes studied included a patterned array of diamond emitters (that could be used to generate multi-bunch beams) and a carbon nanotube cathode with randomly oriented emitters. The latter produced Ampere-

class beams. The successful demonstration of this type of cathodes has potential in the development of compact and portable high current electron accelerators in high resolution x-ray imaging and free electron lasers. Patterned diamond field emitter cathodes are also attractive when combined with advanced phase space manipulations to form attosecond electron bunch trains such as the ones needed to drive compact coherent x-ray sources [96].

The facility was also employed to perform beam dynamics experiments on inverse Compton scattering to generate soft x-rays, explore the generation of ellipsoidal bunches from Cs_2Te photocathode, and investigate a simple temporal-shaping technique. Particularly, we demonstrated inverse Compton scattering of low energy $\sim$ 4-MeV electrons with a 800-nm laser beam.

REFERENCES

[1] W. Henning et al. Accelerators for America's Future. Technical Report, U.S. Dept. of Energy, 2010.

[2] V. Shvedunov et al. Low energy electron accelerators and applications. Plenary talk, *2011 Dual Year Russia–Spain*, Nov. 10, 2011.

[3] J. A. Antolak et al. Electron Radiotherapy: Past, Present, and Future. *AAPM Annual Meeting*, TH-A-500-1, Indianapolis, Aug. 8, 2013.

[4] D. J. Griffiths. Introduction to Electrodynamics. *Prentice Hall*, NJ, 3rd Ed., 1999.

[5] S. G. Biedron et al. Compact, e-beam based mm-and THz-wave light sources. *Workshop on Terahertz Sources for Time Resolved Studies of Matter*, ANL, Jul. 30-21, 2012.

[6] S. I. Molokovsky. Intense Electron and Ion Beams. *Springer*, August 18, 2005.

[7] D. Holcolbe et al. Vacuum microelectronic emitters and their applications using compound semiconductor technology. Report, UCSB, 1994.

[8] Archive of Cern Courier. http://cerncourier.com/cws/article/cern/58918

[9] A. R. Fry. Novel Pulse Train Glass Laser for RF Photoinjectors. *Doctoral dissertation*, Dept. of Physics and Astronomy, University of Rochester, 1996.

[10] T. W. Koeth. An Observation of a Transverse to Longitudinal Emittance Exchange at the Fermilab A0 Photoinjector. *Doctoral dissertation*, Dept. of Physics and Astronomy, The State University of New Jersey, 2009.

[11] P. Musumeci et al. Experimental Generation and Characterization of Uniformly Filled Ellipsoidal Electron-Beam Distributions. *Physical Review Letters*, 100, 244801, 2008.

[12] C. R. Prokop. Advanced Beamline Design for Fermilab's Advanced Superconducting Test Accelerator. *Doctoral dissertation*, Dept. of Physics, Northern Illinois University, 2014.

[13] Y. E. Sun. Angular-Momentum-Dominated Electron Beams and Flat-Beam Generation. *Doctoral dissertation*, Dept. of Physics, University of Chicago, 2005.

[14] P. Piot et al. Operation of an ungated diamond field-emission array cathode in a L-band radiofrequency electron source. *Applied Physics Letters*, 104, 263504, 2014.

[15] C. Lejeune et al. Emittance and Brightness: Definitions and Measurements. *Applied Charged Particle Optics*, p. 159, Part A, Academic Press, NY, 1980.

[16] Y. E. Sun et al. Improved emittance measurement system for the flat-beam experiment at FNPL. FNAL Publication, Beams-doc-1870-v1, 2005.

[17] C. M. Bhat et al. Envelope and multi-slit emittance measurements at Fermilab A0 photoinjector and comparison with simulations. Report, Fermilab-Conf-07-321-AD, 2007.

[18] M. Pherson et al. A magnetic spectrometer for electron energy calibration. NRC Publications Archive, PIRS-0617, May 1998.

[19] E. Hemsing et al. Beam by design: Laser manipulation of electrons in modern accelerators. *Reviews of Modern Physics*, 86, 897, Jul. 2014.

[20] J-C. Deils, W. Rudolph. Ultrashort Laser Pulse Phenomena. *Elsevier Inc.*, 2006.

[21] K. T. MacDonald. Gaussian laser beams with radial polarization, 2000.

[22] W. Koechner. Solid-State Laser Engineering. *Springer*, NY, 4th Ed., 1999.

[23] A. Webster. Useful Mathematical Formulas for Transform Limited Pulses. Dec. 3, 2012.

[24] P. F. Moulton. Ti-doped Sapphire Tunable Solid State Laser. *Optics News*, Vol. 8, No. 6, 1982.

[25] http://www.idestaqe.com/products/ultrafast-laser/octavius-85m/

[26] http://www.idestaqe.com/IDESTAQE/assets/File/Idesta-Octavius_85M.pdf

[27] D. Strickland et al. Compression of amplified chirped optical pulses. *Optics Communications*, Vol. 56, 3, p. 219-221, 1985.

[28] Spitfire Pro, Ti:Sapphire Regenerative Amplifier System. Part Number 90015207, Rev A, Feb. 2008.

[29] Y. Li et al. Generating a Quasiellipsoidal Electron Beam by 3D Laser-Pulse Shaping. *Physical Review Letters*, 100, 074801, Feb. 2008.

[30] T. Maxwell. Measurement of Sub-picosecond Electron Bunches via Electro-optic Sampling of Coherent Transition Radiation. *Doctoral dissertation*, Dept. of Physics, Northern Illinois University, May 2012.

[31] F. Verluise et al. Amplitude and phase control of ultrashort pulses by use of an acousto-optic programmable dispersive filter: pulse compression and shaping. *Optics Letters*, Vol. 25, No. 8, Apr. 15, 2000.

[32] https://en.wikipedia.org/wiki/Acousto-optic_programmable_dispersive_filter

[33] A. M. Weiner. Ultrafast Optics. *John Wiley & Sons, Inc.*, New Jersey, 2009.

[34] F. Guillot, Z. Javalon. Dazzler user manual, physics.

[35] P. A. Franken et al. Generation of Optical Harmonics. *Physical Review Letters*, 7, 118, 1961.

[36] I. McKinnie et al. High-harmonic generation: Ultrafast lasers yield X-rays. *Nature Photonics*, 4, p. 149-151, 2010.

[37] R. Trebino. Frequency-Resolved Optical Gating: The Measurement of Ultrashort Laser Pulses. *Springer*, NY, Aug. 2000.

[38] K. W. DeLong et al. Pulse retrieval in frequency-resolved optical gating based on the method of generalized projections. *Optics Letters*, Vol. 19, No. 24, 1994.

[39] L. Xu. Measurement of Complex Ultrashort Laser Pulses Using Frequency-Resolved Optical Gating, *Doctoral dissertation*, Georgia Institute of Technology, Aug. 2009.

[40] T. Maxwell. Synchronization and characterization of an ultrashort pulse laser for photoemission and electron-beam diagnostics studies at a radio frequency photoinjector. *JINST*, 7 T110014, 2012.

[41] Operation manual, LB1005 High-Speed Servo Controller, P2102297 Rev. A.

[42] A. Visioli. Practical PID Control. *Springer Science & Business Media*, Nov. 2003.

[43] http://www.microwavefilter.com/MNiriscoupled.htm

[44] N. A. Moody. Fabrication and Measurement of Cesiated Metal Photocathodes. *Masters thesis*, Dept. of Electrical and Computer Engineering, University of Maryland, 2004.

[45] I. V. Bazarov et al. Thermal Emittance and Response Time Measurements of a GaN Photocathode. *Journal of Applied Physics*, 105, 083715, 2009.

[46] I. Will et al. Photocathode Lasers for Cesium Telluride Photocathodes. *1st Topical Workshop on Laser Based Particle Sources*, 22, CERN, Feb. 21, 2013.

[47] K. L. Jensen. Advances in Imaging and Electron Physics. *Elsevier Academic Press*, Vol. 149, 2007.

[48] R. A. Loch. Cesium-Telluride and Magnesium for High Quality Photocathodes: Preparation and Diagnostics. *Masters thesis*, University of Twente, Netherlands, 2005.

[49] Z. Yusof et al. Kelvin Probe Studies of Cesium Telluride Photocathode for AWA Photoinjector. *Nuclear Instruments and Methods in Physics Research Section A: Accelerators, Spectrometers, Detectors and Associated Equipment*, 711, p. 60-64, 2013.

[50] S. H. Kong et al. Fabrication and characterization of cesium telluride photocathodes: A promising electron source for the Los Alamos Advanced FEL. *Nuclear Instruments and Methods in Physics Research A*, 358, p. 276-279, 1995.

[51] W. E. Spicer, A. Herrera-Gomez. Modern Theory and Applications of Photocathodes. SLAC-PUB-6306, Aug. 1993.

[52] P. Musumeci et al. Multiphoton Photoemission from a Copper Cathode Illiminated by Ultrashort Laser Pulses in an rf Photoinjector. *Physical Review Letters*, 104, 084801, 2010.

[53] P. Muggli et al. Two-color photoemission produced by femtosecond laser pulses on copper. *Journal of the Optical Society of America B* 12, 4, p. 553-558, 1995.

[54] J. H. Bechtel et al. Two-photon photoemission from metals induced by picosecond laser pulses. *Physical Review Letters B*, 15, 4557, 1977.

[55] B. B. Laud. Lasers and Non-linear Optics. *John Wiley Sons, Inc.*, 1991.

[56] G. Ferrini et al. Non-liner electron photoemission from metals with ultrashort pulses. *Nuclear Instruments and Methods in Physics Research A*, 601, p. 123-131, 2009.

[57] C. Hong. Intelligent Field Emission Arrays. *Doctoral dissertation*, Dept. of Materials Science and Engineering, Massachusetts Institute of Technology, 2003.

[58] G. Fursey. Field Emission in Vacuum microelectronics. *Kluwer Academic/Plenum Publishers*, NY, 2005.

[59] R. H. Fowler, L. Nordheim. *Proceedings of Royal Society of London*, A 119, p. 173-181, 1928.

[60] E. Minoux et al. Achieving High-Current Carbon Nanotube Emitters. *Nano Letters*, 5, 11, p. 2135-2138, 2005.

[61] J. W. Wang et al. Field Emission and RF Breakdown in High-Gradient Room-Temperature Linac Structures. SLAC-PUB, 7684, 1997.

[62] L. F. Velasquez-Garcia et al. Uniform High-Current Cathodes Using Massive Arrays of Si Field Emitters Individually Controlled by Vertical Si Ungated FETs Part 1: Device Design and Simulation. *IEEE Transactions on Electron Devices*, 58, 6, Jun. 2011.

[63] J. D. Jarvis et al. Resonant tunneling and extreme brightness from diamond field emitters and carbon nanotubes. *Journal of Applied Physics*, 108, 094322, 2010.

[64] A. Mustonen et al. Five picocoulomb electron bunch generation by ultrafast laser-induced field emission from metallic nano-tip arrays. *Applied Physics Letters*, 99, 103504, 2011.

[65] X. Caldern-Coln et al. A carbon nanotube field emission cathode with high current density and long-term stability. *Nanotechnology*, 20, 32570, 2009.

[66] K. B. K. Teo et al. Microwave devices: Carbon nanotubes as cold cathodes. *Nature*, 437, 968, 2005.

[67] C. A. Brau. High-brightness electron beams – small free-electron lasers. *Nuclear Instruments and Methods in Physics Research Section A: Accelerators, Spectrometers, Detectors and Associated Equipment*, 407, p. 1-3, 1998.

[68] J. D. Jarvis et al. Fabrication of Diamond Field-Emitter-Array Cathodes for Free-Electron Lasers. *Proceedings of FEL08*, Gyeongju, Korea, 2008.

[69] W. Zhu et al. Large current density from carbon nanotube field emitters. *Applied Physics Letters*, 75, 873, 1999.

[70] Finite Element Analysis (FEA) Software, http://www.comsol.com/multiphysics/fea-software

[71] D. Mihalcea et al. Simulations of Field-Emission Cathodes for High Current Electron Injectors. *Proceedings of LINAC08*, Victoria, Canada, 2008.

[72] J. P. Carneiro et al. Transverse and longitudinal beam dynamics studies at the Fermilab photoinjector. *Physical Review Special Topics Accelerators and Beams*, 8, 040101, 2005.

[73] J. J. Hartzell et al. Continued Development and Testing of Carbon Nanotube Cathodes at Radiabeam. *Proceedings of NAPAC*, Pasadena, CA, 2013.

[74] D. Mihalcea et al. Ampere-Class Pulsed Field Emission from Carbon-Nanotube Cathodes in a Radiofrequency Resonator. arXiv:1502.03040v1, 2015.

[75] F. M. Charbonner et al. Basic and applied studies of field emission at microwave frequencies. *Proceedings of IEEE*, 51, 7, 991, 1963.

[76] J. W. Lewellen et al. Field-emission cathode gating for rf electron guns. *Physical Review Special Topics Accelerators and Beams*, 8, 033502, Mar. 2005.

[77] P. Sprangle et al. Tunable, Short-Pulse Hard X-Ray Source from a Compact Laser Synchrotron Source. Naval Research Lab, MR/4790–92-6973, 1992.

[78] W. Leemans et al. Femptosecond X-rays from 90^0 Thomson Scattering. *Proceedings of PAC*, 1, p. 174-176, 1995.

[79] O. Williams. Basic Theory of Inverse Compton (Thomson) Scattering and Conceptual Design of X-ray Source using the PEGASUS Linac at UCLA and a Tabletop Terawatt Laser. pbpl.physics.ucla.edu/Education/Courses/Physics_199/Inverse_Compton/

[80] W. S. Graves. Compact XFEL Light Source. *Proceedings of 2013 FEL*, NY, Aug. 2013.

[81] E. Nanni et al. Demonstration of inverse Compton scattered x-rays. Internal report, MIT CUBIX team, Sept. 29, 2013.

[82] B. Blomberg. Development of a novel X-ray source from planar electron channeling. *Masters thesis*, Dept. of Physics, Northern Illinois University, May 2014.

[83] I. M. Kapchinskii et al. Limitations of proton beam current in a strong focusing linear accelerator associated with beam space charge. *Proceedings of International Conference on High Energy Aceelerators*, p. 274, 1959.

[84] O. J. Luiten et al. *Physical Review Letters*, 93, 094802, 2004.

[85] J. B. Rosenzweig. The High Brightness Electron Beam Physics and Photoinjector Technology Program at UCLA. *Beam Dynamics Newsletter*, 46, 2008.

[86] L. Serafini. Advanced Accelerator Concepts. *AIP Conference Proceedings*, 413, 321, 1997.

[87] T. van Oudheusden. Electron source for sub-relativistic single-shot femtosecond diffraction. *Doctoral dissertation*, Dept. of Applied Physics, Eindhoven University of Technology, Netherlands, 2010.

[88] P. Piot et al. Formation and acceleration of uniformly-filled ellipsoidal electron bunches obtained via space–charge-driven expansion from a cesium-telluride photocathode. *Physical Review Special Topics Accelerators and Beams*, 16, 010102, 2013.

[89] F. Lemery et al. Temporal Electron-bunch Shaping from a Photoinjector for Advanced Accelerator Applications. *Proceedings of IPAC 2014*, Germany, Jun. 2014.

[90] J. G. Power et al. Temporal Laser Pulse Shaping for RF Photocathode Guns: The Cheap and Easy way using UV Birefringent Crystals. *AIP Conference Proceedings*, 1086, 689, 2009.

[91] I. Bazarov et al. Efficient temporal shaping of electron distributions for high-brightness photoemission electron guns. *Physical Review Special Topics Accelerators and Beams*, 11, 040702, 2008.

[92] S. Zhou et al. Efficient temporal shaping of ultrashort pulses with birefringent crystals. *Applied Optics*, Vol. 46, p. 8488-8492, 2007.

[93] T. Vo-Dinh. Biomedical Photonics Handbook. *CRC Press*, p. 2-36, 2003.

[94] J. C. Thangaraj et al. Bunch Shaping Experiments at the High Brightness Electron Source Laboratory (HBESL) (in press). *Proceedings of AAC 2014*, San Jose, 2014.

[95] J. C. Thangaraj et al. Z-shaper: A Picosecond UV Laser Pulse Shaping Channel at the Advanced Superconducting Test Accelerator. *Proceedings of LINAC*, Geneva, 2014.

[96] W. S. Graves et al. Intense Superradiant X Rays from a Compact Source Using a Nanocathode Array and Emittance Exchange. *Physical Review Letters*, 108, 263904, 2012.